Engineering Journal

First Quarter 2024 | Volume 61, No. 1

Smarter. Stronger. Steel.

Engineering Journal

American Institute of Steel Construction

Dedicated to the development and improvement of steel construction, through the interchange of ideas, experiences, and data.

Engineering Journal (ISSN 0013-8029) is published quarterly. Published by the American Institute of Steel Construction at 130 E Randolph Street, Suite 2000, Chicago, IL 60601.

Archives: Search at **aisc.org/ej**. Article downloads are free for current members and are available for a nominal fee for non-members.

Seismic Design and Performance of Composite Coupling Beam-to-SpeedCore Wall Connections

Amit H. Varma, Mubashshir Ahmad, Soheil Shafaei, and Ron Klemencic

ABSTRACT

Coupled composite plate shear walls—concrete filled (CC-PSW/CFs) are an effective seismic lateral-force-resisting system for the design and construction of mid- to high-rise buildings around the world. The coupled system consists of two or more composite plate shear walls—concrete filled (C-PSW/CFs) connected to each other using composite coupling beams located at the story heights. The CC-PSW/CF system can provide higher overturning moment capacity, lateral stiffness, and ductility than uncoupled walls. Concrete-filled steel box sections are typically used for the composite coupling beams, which are designed to be flexure critical members. When the CC-PSW/CF system is subjected to lateral seismic forces, plastic hinge formation and inelastic deformations (energy dissipation) occur near the ends of most of coupling beams along the structure's height, followed by flexural hinging of the C-PSW/CFs, typically at the base. This paper presents the details and design of four composite coupling beam-to-C-PSW/CF connection configurations. Six connection specimens representing the four connection configurations, with beam clear span-to-section depth, L_b/d, ratios of 3.5 and 5.1, were designed and tested. The lateral force-displacement and moment-rotation responses of the specimens are summarized. All six composite coupling beam-to-C-PSW/CF wall connection specimens (1) developed and exceeded the plastic flexural capacities, M_p, of the coupling beams calculated using the plastic stress distribution method and (2) developed chord rotation capacities greater than 0.03 radian before their flexural strength degraded to 80% of the plastic moment capacity, M_p.

Keywords: SpeedCore, composite, connections, coupling beam, coupled system, shear walls, seismic design, experimental research, performance assessment.

INTRODUCTION

Coupled composite plate shear walls—concrete filled (CC-PSW/CF) consist of two or more composite plate shear walls (concrete filled) connected using composite coupling beams (links), as shown in Figures 1(a) and 1(b). The uncoupled C-PSW/CF system was included as a seismic force-resisting system (SFRS) in ASCE/SEI 7-16 (ASCE, 2016), and its seismic design and detailing requirements were presented in the 2016 AISC *Seismic Provisions for Structural Steel Buildings*, ANSI/AISC 341-16 (AISC, 2016). However, the coupled (CC-PSW/CF) system was not addressed in either standard.

Recent research has focused on developing seismic design and detailing requirements for the CC-PSW/CF system. The results from a rigorous FEMA P695 study conducted recently (Bruneau et al., 2019; Kizilarslan et al. 2021b; Broberg et al., 2022) have confirmed that CC-PSW/CF can be used as a distinct SFRS with seismic response modification factors of 8 ($R = 8$), overstrength factor of 2.5 ($\Omega_0 = 2.5$), and displacement amplification factor of 5.5 ($C_d = 5.5$). This led to the inclusion of the CC-PSW/CF system and its seismic design and detailing procedure in FEMA P-2082-1 (FEMA, 2020) and, subsequently, its seismic response modification factors in ASCE/SEI 7-22 (ASCE, 2022); seismic design and section detailing requirements in the 2022 AISC *Seismic Provisions for Structural Steel Buildings*, ANSI/AISC 341-22 (AISC, 2022a); and detailed design examples and guidance in AISC Design Guide 38, *SpeedCore Systems for Steel Structures* (Varma et al., 2023) and Chapter 5 of FEMA P-2192-V1 (FEMA, 2021).

Figure 1 shows a typical CC-PSW/CF system along with its components. Figure 1(c) shows a typical cross section of a planar C-PSW/CF. Planar C-PSW/CF comprises two steel web plates and two flange (closure) plates welded together to form a box section. The web plates are connected using tie bars, which improve the stability of empty steel modules during transportation, erection, and concrete casting (Varma et al., 2019). The steel tie bars and headed stud anchors are used to develop the composite interaction between steel plates and infill concrete. In the seismic design of CC-PSW/CF, composite coupling beams are used due to their high flexural stiffness and capacities. Figure 1(d) shows a typical cross section of a composite coupling beam made of built-up steel box-section and plain concrete.

Amit H. Varma, Karl H. Kettelhut Professor, Purdue University, West Lafayette, Ind. Email: ahvarma@purdue.edu (corresponding)

Mubashshir Ahmad, PhD Candidate, Purdue University, West Lafayette, Ind. Email: ahmad54@purdue.edu

Soheil Shafaei, Lead Research Scientist, Purdue University, West Lafayette, Ind. Email: sshafaei@purdue.edu

Ron Klemencic, President and CEO, Magnusson Klemencic Associates, Seattle, Wash. Email: rklemencic@mka.com

Paper No. 2022-11

The empty steel modules of C-PSW/CFs are prefabricated in a shop and transported to the site for erection. The empty steel modules of C-PSW/CFs serve as formwork and falsework during the construction and concrete casting; hence, using this system improves the construction schedule considerably (Varma et al., 2019). The steel plates act as primary reinforcement of the walls in the composite phase (Varma et al., 2014). This system is commercially referred to as the SpeedCore system by the American Institute of Steel Construction (AISC) because of the remarkable reduction in overall construction time. This decrease in construction time was demonstrated by the Rainier Square Tower (Traut-Todaro, 2019), constructed approximately 43% faster than the typical reinforced concrete (RC) corewall building with steel framing. The Rainier Square Tower is the first commercial high-rise building employing the CC-PSW/CF system in the United States. It utilized a CC-PSW/CF core system surrounded by traditional steel gravity frames (composite steel floor). The wall modules were preinstalled with shear tabs for steel beam framing connections and ledger angles for deck support. Holes were predrilled at the floor level to connect the concrete deck to the composite core through dowel rebars. The prefabricated steel modules were erected and spliced on site by a combination of partial-joint-penetration (PJP) groove welds and reinforcing fillet welds.

The coupling beam-to-composite wall connections are an integral part of the CC-PSW/CF system. Seismic performance requirements for these coupling beam-to-wall connections have been specified in ANSI/AISC 341-22. Performance confirmation for coupling beam-to-wall connections is essential to achieve the seismic performance of the system (Kizilarslan et al., 2021b; Broberg et al., 2022). This paper presents the design of four different beam-to-wall connection configurations in accordance with the corresponding provisions in ANSI/AISC 341-22, as exemplified

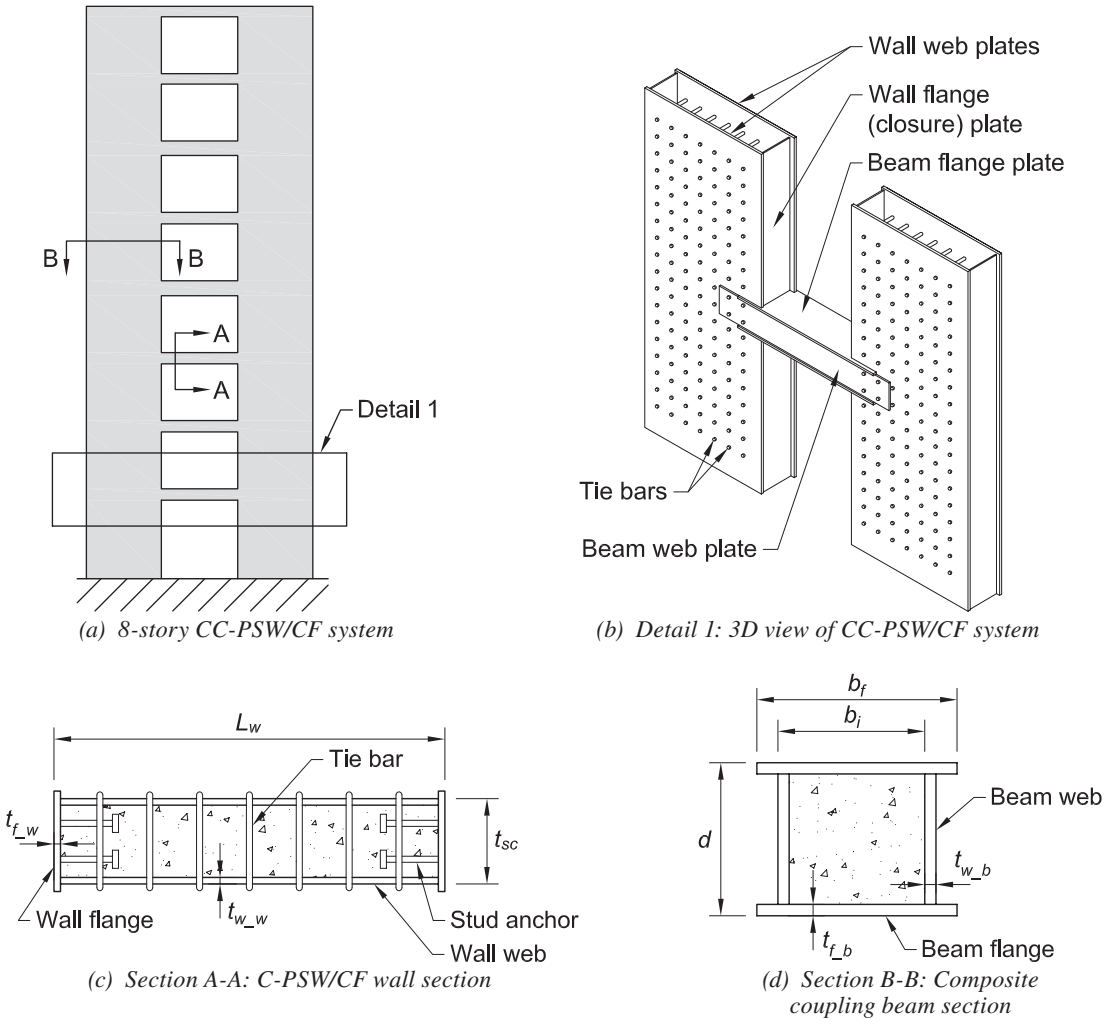

(a) 8-story CC-PSW/CF system

(b) Detail 1: 3D view of CC-PSW/CF system

(c) Section A-A: C-PSW/CF wall section

(d) Section B-B: Composite coupling beam section

Fig. 1. Typical CC-PSW/CF system and components.

in AISC Design Guide 38, and their experimental performance in terms of the rotational capacities developed.

BACKGROUND

Individual uncoupled shear walls provide good seismic behavior and resistance. However, connecting individual shear walls using coupling beams at each story provides greater stiffness and redundancy to the seismic force-resisting system. The coupled system has lateral stiffness greater than the sum of the two connected walls (El-Tawil et al., 2010). The overturning moment is resisted partially by coupling action resulting from the axial force (tension-compression) couple across the wall system, which reduces the moment demand on the individual walls. If designed appropriately, plastic hinging and inelastic deformations (energy dissipation) occur at the ends of the coupling beams and spread along the height of the structure, rather than just being concentrated at the base of the individual shear walls.

For the CC-PSW/CF system, Broberg et al. (2022) developed a capacity design method based on a weak beam–strong wall design principle that prioritizes the occurrence of plastic hinging at the ends of the coupling beams and spreading of plasticity along the height of the structure before forming plastic hinges at the bases of the individual shear walls. Several archetype (3- to 22-story) structures were designed using this capacity design principle. Nonlinear inelastic finite element models for the composite walls and coupling beams were developed and benchmarked using experimental results (Kizilarslan et al., 2021a; Shafaei et al., 2021a, 2021b; Bruneau et al., 2019). These models were used to conduct incremental dynamic (nonlinear time-history) analyses for 22 sets of appropriately scaled ground motions according to the FEMA P695 procedure. The seismic response of CC-PSW/CF systems reasonably follows the sequence of plastification assumed by the capacity design principle (Broberg et al., 2022). Statistical analysis of the results confirms the proposed seismic factors ($R = 8$, $\Omega_0 = 2.5$, and $C_d = 5.5$) for the CC-PSW/CF system (Kizilarslan et al., 2021b).

The coupled system has better ductility and seismic behavior due to the spread of plasticity along the height of the structure through the formation of plastic hinges at the ends of the coupling beams. For uncoupled walls, inelastic deformations concentrate in the plastic hinge regions at the base of the individual walls, while the remaining wall lengths remain mostly elastic. Comprehensive FEMA P695 studies conducted for uncoupled C-PSW/CF wall systems have confirmed seismic factor values of $R = 6.5$, $\Omega_0 = 2.5$, and $C_d = 5.5$ for the uncoupled system (Broberg et al., 2023; Kizilarslan and Bruneau, 2023).

The higher R factor of 8 for the coupled system acknowledges its better ductility and ability to spread plasticity along the height of the structure. The coupling beam-to-wall connections play an important role in achieving this system level ductility. They are required to have adequate strength to develop the flexural plastic hinges at the ends of the coupling beams and sustain them for at least 0.03 rad of chord rotation before flexural strength degrades below 80% of the nominal plastic moment capacity. The incremental dynamic (nonlinear time-history) analyses conducted as part of the FEMA P695 studies modeled the inelastic behavior of the coupling beam plastic hinges in accordance with this performance requirement, present in ANSI/AISC 341-22, Section H8.8.

Consequently, the coupling beam-to-wall connections used in the CC-PSW/CF system should accommodate this performance requirement and exhibit a minimum chord-rotation capacity of 0.03 rad before flexural strength degrades to 80% of the nominal plastic moment capacity, M_p. This type of connection performance requirement, shown in Figure 2, is prevalent in seismic design provisions (ANSI/AISC 341-22). For example, beam-to-column connections in intermediate moment frames and special moment frames are required to have chord rotation capacities of at least 0.02. and 0.04 rad, respectively.

It is also important to note that the FEMA P695 study and, consequently, the current seismic design provisions (ANSI/AISC 341-22) are limited to CC-PSW/CF systems designed with flexure-critical coupling beams, with a clear span-depth (L_b/d) ratio greater than or equal to 3 and less than or equal to 5. Shear-critical composite coupling beams with an L_b/d ratio less than 3.0 were not included for several reasons, including the inadequate cyclic performance seen in tests conducted by Nie et al. (2014). Currently, there is a lack of coupling beam-to-composite wall connections that have been designed, detailed, and then tested to confirm their performance under cyclic loading. This paper directly addresses this gap in knowledge.

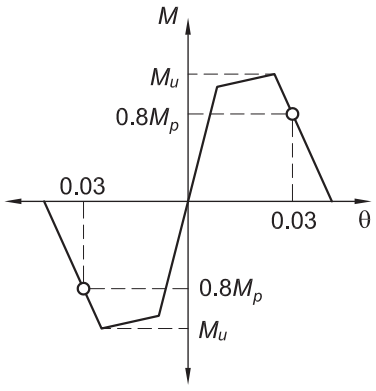

Fig. 2. Envelope of moment–rotation (M-θ) response of coupling beam.

Table 1. Planar CC-PSW/CF Archetypes from Bruneau et al. (2019)							
Case	Number of Stories	Coupled Wall Length, L_w, in.	Wall Thickness, t_{sc}, in.	Plate Thickness, t_{f_w}, and t_{w_w}, in.	Coupling Beam Length, L_b, in.	Coupling Beam Section, in.	L_b/d
PG-1A	8	144	20	9/16	72	$20(b_f)\times24(d)\times$ $3/8(t_{f\_b})$, $3/8(t_{w\_b})$	3
PG-1B		132	24	9/16	96	$24(b_f)\times24(d)\times$ $1/2(t_{f\_b})$, $3/8(t_{w\_b})$	4
PG-1C		120	24	5/8	120	$24(b_f)\times24(d)\times$ $1/2(t_{f\_b})$, $3/8(t_{w\_b})$	5
PG-2B	8	144	10	3/16	72	$10(b_f)\times18(d)\times$ $3/16(t_{f\_b})$, $1/4(t_{w\_b})$	4
PG-1D	12	204	18	9/16	72	$18(b_f)\times24(d)\times$ $5/16(t_{f\_b})$, $3/8(t_{w\_b})$	3
PG-1E		192	22	9/16	96	$22(b_f)\times24(d)\times$ $7/16(t_{f\_b})$, $3/8(t_{w\_b})$	4
PG-1F		180	24	9/16	120	$24(b_f)\times24(d)\times$ $1/2(t_{f\_b})$, $3/8(t_{w\_b})$	5
PG-2E	12	204	8	3/16	72	$8(b_f)\times18(d)\times$ $3/16(t_{f\_b})$, $1/4(t_{w\_b})$	4

DESIGN AND DETAILS OF CONNECTIONS IN ARCHETYPE STRUCTURES

Several CC-PSW/CF archetype structures (3-, 8-, 12-, 18-, and 22-story buildings) using planar or C-shaped C-PSW/CFs and composite coupling beams were designed following the capacity design method described in Broberg et al. (2022). Table 1 provides the dimensions and details of 8- and 12-story CC-PSW/CF archetype structures with planar C-PSW/CFs and composite coupling beams as shown in Figure 1 and reported in Bruneau et al. (2019) and Kizilarslan et al. (2021b).

Composite Coupling Beam-to-C-PSW/CF Connections

Four composite coupling beam-to-C-PSW/CF connections—identified as connection types 1, 2, 3, and 4—were developed based on construction considerations and expected structural performance. Connection types 1 and 2 have slots cut in the wall web plates to receive the coupling beam flange plates, which are wider than the wall thickness, t_{sc}. The beam flange plates are connected to the wall web plates using complete-joint-penetration (CJP) groove welding from the outside. The web plates of the wall and coupling beam are separate. The web plates of the coupling beam overlap the web plates of the wall and are fillet welded from the outside. The common details of connection types 1 and 2 are shown in Figure 3.

Continuity of the wall flange (closure) plate is the only difference between these two connections. In connection type 1, the wall flange (closure) plate is interrupted where the beam flanges enter the wall webs, leading to monolithic concrete in the wall and coupling beam [Figure 4(a)]. In connection type 2, the flange (closure) plate is continuous, as shown in Figure 4(b), leading to the concrete being interrupted between the walls and the coupling beam. Connection type 2 was conceptualized to study the importance, or lack thereof, of the continuity of the vertical flange (closure) plate of the wall through the depth of the coupling beam. The beam flange plate is first inserted into the slots; the wall flange closure plate is then inserted and welded on to the wall web and beam flange plates all four sides. The beam web plates are lapped to the wall web plates and welded at the end. Connection types 1 and 2 are recommended when the design thicknesses of the wall and the

coupling beam web plates are not close to each other—that is, there is more than a quarter-inch difference between them.

Connection types 3 and 4 have a continuous wall and beam web (same plate). As shown in Figure 5, connection type 3 has slots cut in the wall web plates to receive the coupling beam flange plates, which are wider than the wall thickness, t_{sc}. The beam flange plates are connected to the wall web plates using complete joint penetration (CJP) welding from the outside. In connection type 4, the flange plates of the coupling beam have the same width as the inside-to-inside thickness of the wall ($t_{sc} - 2t_p$), as shown in Figure 6. The coupling beam flange plates are placed inside the wall web plates at the connection and are connected to the wall web plates using CJP groove welding.

For both connection types, the wall flange (closure) plate is interrupted where the coupling beam connects to the wall, resulting in monolithic concrete in the wall and coupling beam. The beam flanges were connected to wall flange (closure) plates using fillet welding as shown in Figures 5 and 6. Connection types 3 and 4 are recommended when the design thicknesses for the wall and the coupling beam web plates have less than a quarter-inch difference between them. Instead of using separate web plates for the wall and beam, the wall web plate can be continued in the beam.

Design of Coupling Beam-to-C-PSW/CF Connections

Coupling beam-to-C-PSW/CF connections for the 8- and 12-story archetype structures (with planar walls) were designed according to ANSI/AISC 341-22, Section H8.8, and AISC Design Guide 38. The coupling beam-to-C-PSW/CF connection was designed to develop and transfer 1.2 times the expected flexural capacity $M_{p,exp}$ (and corresponding capacity-limited shear force) of the coupling beam. Forces in the beam elements were calculated, and a mechanism to transfer the forces to the wall elements was identified. The connections were then detailed to have a higher capacity than the required forces.

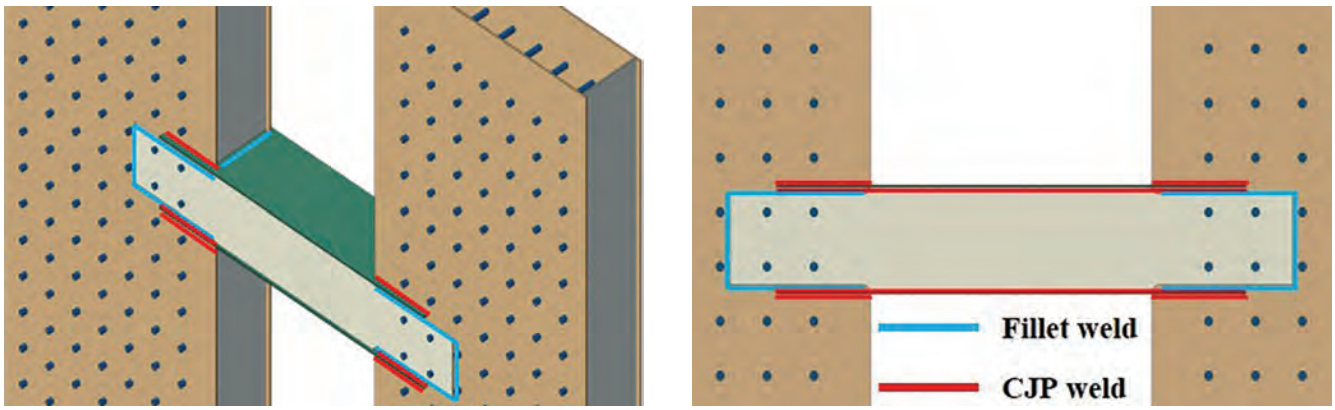

(a) Connection details *(b) Flange and web welding details*

Fig. 3. Common details of connection type 1 and 2.

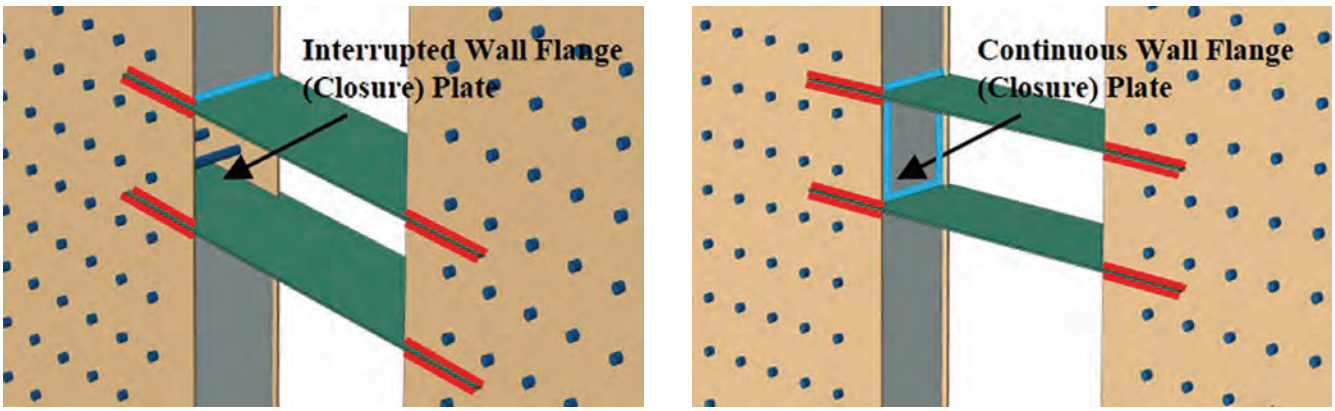

(a) Connection type 1 *(b) Connection type 2*

Fig. 4. Details of connection type 1 and type 2 (beam web plates are hidden).

The expected flexural capacity, $M_{p,exp}$, of the composite coupling beam was calculated using the plastic stress distribution method in the AISC *Specification for Structural Steel Buildings*, ANSI/AISC 360-22, Section I1.2 (AISC, 2022b), while using the expected yield strength, R_yF_y, for steel and the expected compressive strength, $R_cf'_c$, for concrete. Forces resisted by the flange plates, web plates, and concrete infill of the beam are transferred to the walls through the following connection elements:

1. Beam flange-to-wall web connection
2. Beam flange-to-wall flange connection
3. Beam web-to-wall web connection
4. Direct bearing of beam infill concrete to wall concrete

Preliminary finite element analyses of the coupling beam-to-C-PSW/CF connections showed the stresses in the beam flange were transferred to the wall primarily through the beam flange-to-wall web connection, which was also confirmed later by experimental results. The stress transfer through the beam flange-to-wall flange connection was negligible; therefore, the beam flange-to-wall web connection was designed to transfer the entire force in the beam flange, and the beam flange-to-wall flange connection was made using nominal fillet welds. The compression in the beam infill concrete was assumed to be transferred to the wall infill concrete through direct bearing. The required strength and available capacity calculation for the remaining two connection elements, beam flange-to-wall web and beam web-to-wall web, are discussed in the following sub-sections.

Coupling Beam Flange-to-Wall Web Connection

The coupling beam flange-to-wall web weld was designed to transfer the minimum of 120% of the expected tensile yield capacity and 100% of the expected tensile rupture

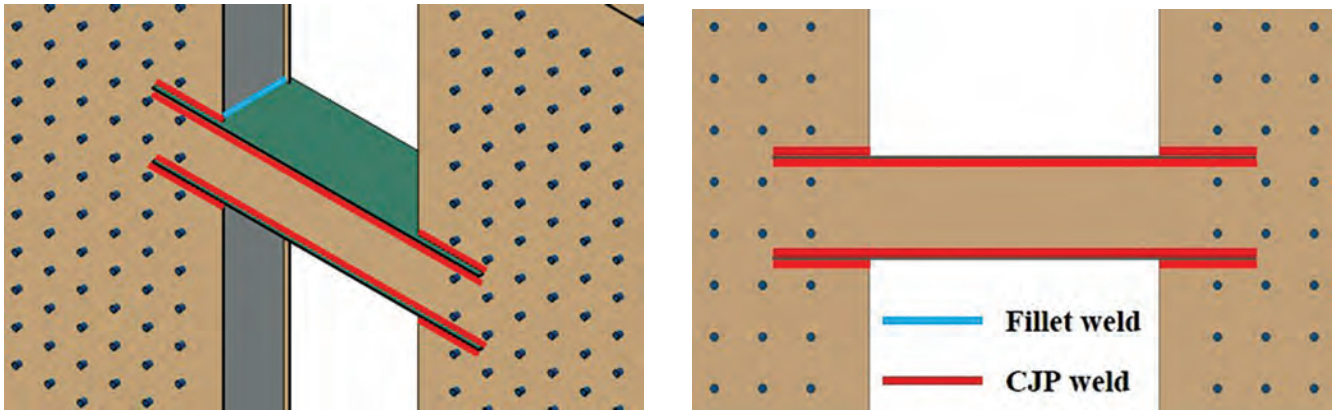

(a) Connection details *(b) Flange welding details*

Fig. 5. Details of connection type 3.

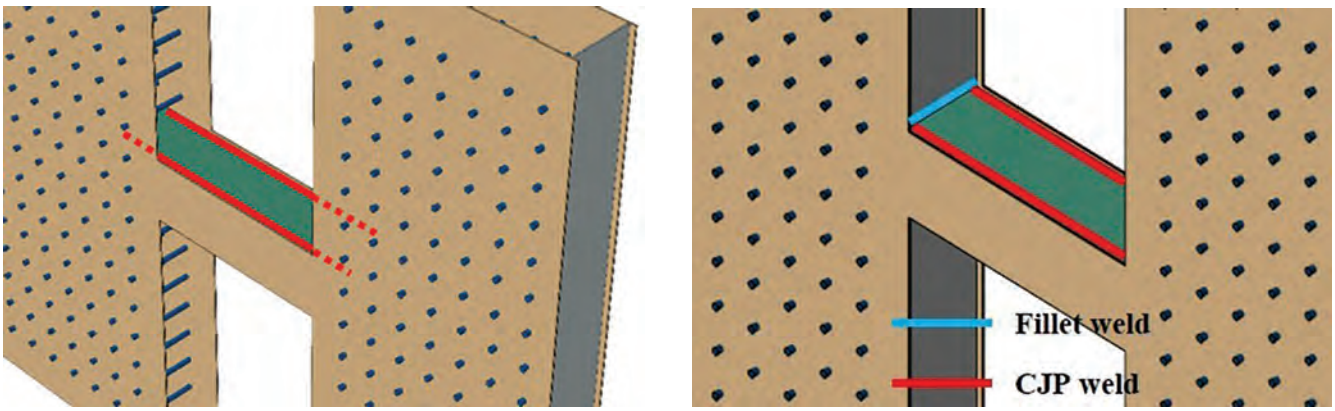

(a) Flange welding details *(b) Connection details*

Fig. 6. Details of connection type 4.

Table 2. Coupling Beam Flange-to-Wall Web Connection Calculations for Archetype Structures								
Case	**PG-1A**	**PG-1B**	**PG-1C**	**PG-2B**	**PG-1D**	**PG-1E**	**PG-1F**	**PG-2E**
Flange plate connection demand								
$1.2R_yF_yA_{f\_CB}$, kips	545	858	858	149	413	693	858	124
$R_tF_uA_{f\_CB}$, kips	590	930	930	161	447	751	930	134
T_{flange}, kips	545	858	858	149	413	693	858	124
Length of weld/flange embedment length								
L_{req}, in.	12.1	14.3	14.3	6.6	11	13.2	14.3	5.5
$L_{provided}$, in.	24	26	26	18	24	24	26	18
Shear strength of beam flange plates								
$\phi_d 0.6R_yF_yA_{f\_SY}$, kips	297	429	429	111	248	347	429	111
$\phi_n 0.6R_tF_uA_{f\_SR}$, kips	347	502	502	130	521	405	502	130
$\frac{T_{flange}}{2}$, kips	272	429	429	74	206	347	429	62
Shear strength of wall web plates								
$\phi_d 0.6R_yF_yA_{w\_SY}$, kips	891	965	1073	223	891	891	965	223
$\phi_n 0.6R_tF_uA_{w\_SR}$, kips	1042	1129	1255	261	1042	1042	1129	261
$\frac{T_{flange}}{2}$, kips	272	429	429	74	206	347	429	62

capacity of the flange plate, as shown in Equation 1. The length of the weld and the corresponding flange embedment length were estimated using Equation 2 to transfer this required tensile force from the beam flange to the wall web. Limit states of shear yielding and shear rupture of the beam flange and wall web plates at the connection were checked against the tension demand using Equations 3 to 6.

$$T_{flange} = \min\left(1.2R_yF_yA_{f\_CB}, R_tF_uA_{f\_CB}\right) \quad (1)$$

$$L_{req} \geq \frac{T_{flange}}{n\left(\phi_d 0.6F_y t_{p,f\_CB}\right)} \geq d \quad (2)$$

$$\frac{T_{flange}}{2} \leq \phi_d 0.6R_yF_yA_{f\_SY} \quad (3)$$

$$\frac{T_{flange}}{2} \leq \phi_n 0.6R_tF_uA_{f\_SR} \quad (4)$$

$$\frac{T_{flange}}{2} \leq \phi_d 0.6R_yF_yA_{w\_SY} \quad (5)$$

$$\frac{T_{flange}}{2} \leq \phi_n 0.6R_tF_uA_{w\_SR} \quad (6)$$

where

A_{f_CB} = cross-sectional area of the coupling beam flange, in.^{2}

A_{f_SR} = net shear area of coupling beam flange plate in shear rupture, in.^{2}

A_{f_SY} = gross shear area of coupling beam flange plate in shear yielding, in.^{2}

A_{w_SR} = net shear area of wall web plate in shear rupture, in.^{2}

A_{w_SY} = gross shear area of wall web plate in shear yielding, in.^{2}

n = number of weld lines connecting each end of beam flange to wall web; equal to 4 for connection types 1, 2, and 3, and equal to 2 for connection type 4

t_{p,f_CB} = thickness of coupling beam flange plate, in.

ϕ_d = 1.00

ϕ_n = 0.90

Sample beam flange-to-wall web connection calculations (with n equal to 4 for connection types 1, 2, and 3) for the archetype structures are presented in Table 2. The calculations are performed using F_y and F_u values of 50 and 65 ksi, respectively, considering an additional inch of overhang on each side of the beam flange to provide welding clearance, as shown in Figures 3, 4, and 5. Potential shear yielding and rupture planes for the coupling beam flange and wall web plates are shown in Figure 7 using yellow lines. Multiple yielding and rupture planes can be checked as applicable. Table 2 summarizes the limits for the cases presented here.

Coupling Beam Web-to-Wall Web Connection

For connection types 1 and 2, with separate beam and wall web plates, the beam web-to-wall web connection was designed to transfer the combination of capacity-limited shear, flexure, and axial force resisted by the beam web plates. Because the plastic neutral axis of the composite section does not coincide with the centroid of the section, the webs are subjected to a net tensile force (T_{web}), moment (M_{web}), and shear (V_{web}), estimated using the stress block shown in Figure 8. Each C-shaped fillet weld group (shown in Figure 9) was designed to transfer one-half of the total force carried by the beam webs—that is, $T_{c,weld}$, $M_{c,weld}$, and $V_{c,weld}$.

The C-shaped weld group connecting the beam web-to-wall web was designed for simultaneous flexure, shear, and tension as follows. AISC *Steel Construction Manual* (AISC, 2023) Table 8-8 was used to design the C-shaped weld group for the combination of flexure and shear, which were converted to an eccentric shear force producing an equivalent effect using Equation 7. This equivalent shear was applied to the C-shaped weld, as shown in Figure 9. The horizontal and vertical weld lengths of the C-shaped welds are also identified in Figure 9. Equations 8 to 12 were used to calculate the strength, $P_{weld,V}$, of the C-shaped weld group subjected to eccentric shear using AISC *Manual* Table 8-8. The strength of the weld group for resisting tension, $P_{weld,H}$, was estimated using Equation 13 in accordance with ANSI/AISC 360-22, Section J2.4, while considering only the horizontal welds of the C-shaped weld group. Finally, the utilization ratio for simultaneous tension and eccentric shear was estimated using the sum of the squared terms (SRSS) method and the individual demand-to-capacity ratios $\left(\frac{V_{c,weld}}{P_{weld,V}} \text{ and } \frac{T_{c,weld}}{P_{weld,H}}\right)$ as shown in Equation 14.

$$Eccentricity(Ecc) = \frac{M_{c,weld}}{V_{c,weld}} \tag{7}$$

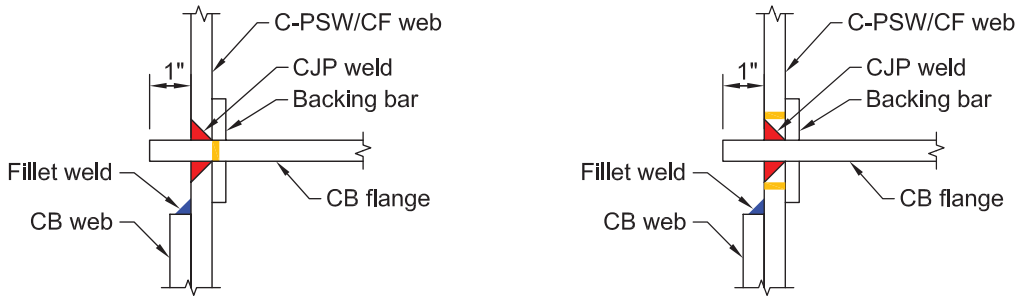

(a) CB flange shear yielding and rupture plane

(b) C-PSW/CF web shear yielding and rupture plane

Fig. 7. Possible shear yielding and rupture planes (shown using yellow lines).

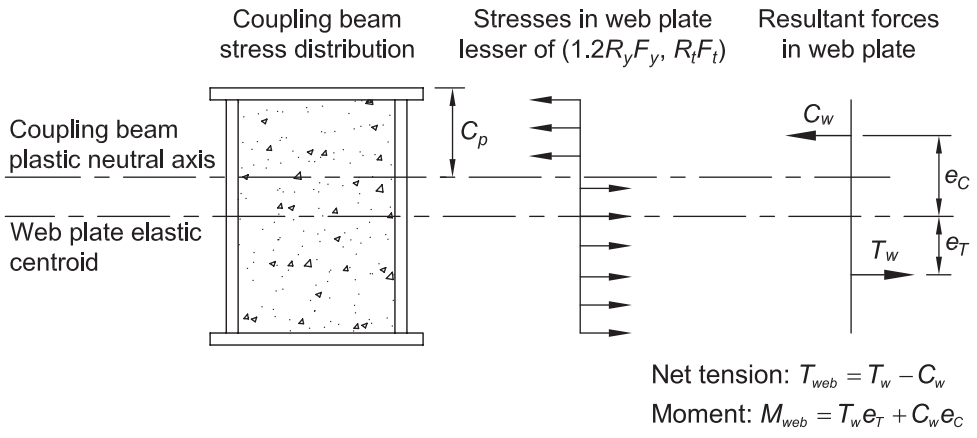

Fig. 8. Tension and moment in coupling beam web plates.

$$cg = \frac{2L_{web,H,weld}\,0.5L_{web,H,weld}}{2L_{web,H,weld}L_{web,V,weld}} \quad (8)$$

$$e_x = Ecc + L_{web,H,weld} - cg \quad (9)$$

$$k = \frac{L_{web,H,weld}}{L_{web,V,weld}} \quad (10)$$

$$a = \frac{e_x}{L_{web,V,weld}} \quad (11)$$

$$P_{weld,V} = \phi_n C_{8.8} C_1 (16w) L_{web,V,weld} \quad (12)$$

$$P_{weld,H} = \phi_n 0.6F_{EXX}\,2L_{web,H,weld}\,(0.707w) \quad (13)$$

$$\sqrt{\left(\frac{V_{c,weld}}{P_{weld,V}}\right)^2 + \left(\frac{T_{c,weld}}{P_{weld,H}}\right)^2} \le 1.0 \quad (14)$$

where

C_1 = electrode strength coefficient
$C_{8\cdot8}$ = coefficient tabulated in AISC *Manual* Table 8-8
F_{EXX} = filler metal classification strength, ksi
w = fillet weld size, in.

Sample beam web-to-wall web connection calculations for the archetype structures are presented in Table 3. It includes the forces resisted by the coupling beam web plates, the demands on the C-shaped welds, the weld geometry including fillet weld size w, the calculated eccentric shear strength, the tension strength, and the utilization ratio. The utilization ratio for all archetype structure connections was approximately 0.8, less than the maximum permissible limit of 1.0.

Detailed section and connection design calculations for an archetype structure (PG-1A) are included in Varma et al. (2021).

TEST SPECIMEN DETAILS

The test specimens designed and fabricated for this study were approximately one-half scale representations of the archetype structure connections. The scaling of the specimens was limited by the testing capacity available in the laboratory. A portion of the coupled system, including one-half of the coupling beam length and one composite wall, was selected to study the connection's response under cyclic lateral loading. The shear force and bending moment distribution in a coupling beam, with the inflection point located at the beam mid-span, was replicated using the half-beam cantilever subassembly. Gong and Shahrooz (2001) and Farsi et al. (2016) have used similar subassembly test setups in the past.

Test Matrix

The test specimens were not precisely scaled representations of any specific archetype structure; instead, they were designed to estimate the fundamental behavior under the constraints of the available laboratory capabilities. Two specimens of connection types 1 and 2 and one specimen of connection types 3 and 4, with beam clear span-to-section depth ratios, L_b/d, of 3.5 and 5.1, were selected as shown in the final test matrix in Table 4. It includes the specimen designation, connection type, and the L_b/d ratio. Geometric details of the wall and coupling beam are given in Table 4 and shown in Figure 10, including:

Wall:

H_w = height, in.
L_w = length, in.
t_{f_w} = flange thickness, in.
t_{sc} = thickness, in.
t_{w_w} = web thickness, in.

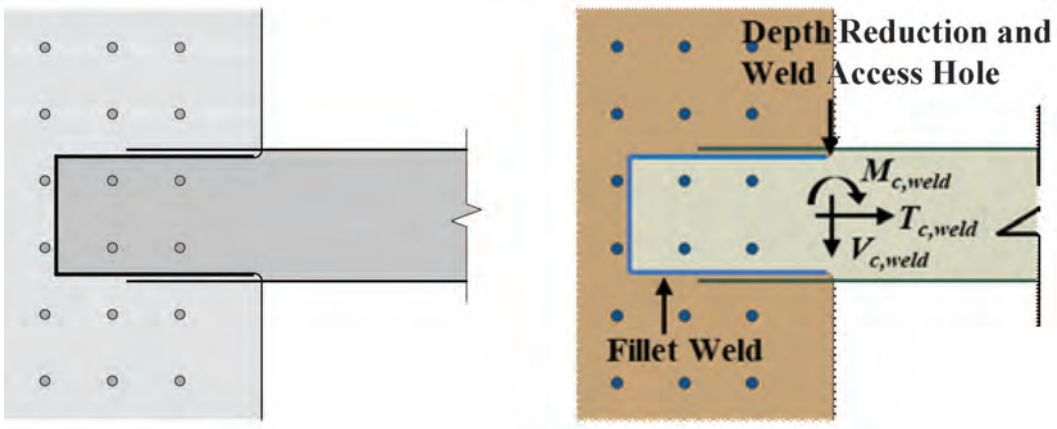

Fig. 9. C-shaped fillet weld connecting beam web-to-wall web.

Table 3. Coupling Beam Web-to-Wall Web Connection Calculations for Archetype Structures								
Case	**PG-1A**	**PG-1B**	**PG-1C**	**PG-2B**	**PG-1D**	**PG-1E**	**PG-1F**	**PG-2E**
Forces in beam web plates								
T_{web}, kips	738	778	778	331	712	759	778	297
M_{web}, kip-in.	3941	3491	3491	1732	4202	3706	3491	1895
V_{web}, kips	662	650	520	185	575	570	520	169
Force demand on C-shaped weld								
$T_{c,weld}$, kips	369	389	389	166	356	380	389	149
$M_{c,weld}$, kip-in.	1971	1746	1746	866	2101	1853	1746	948
$V_{c,\ weld}$, kips	331	325	260	93	288	285	260	85
Weld geometry								
$L_{web,V,weld}$, in.	22	22	22	16	22	22	22	16
$L_{web,H,weld}$, in.	44	44	44	20	44	44	44	20
w, in.	5⁄16	5⁄16	5⁄16	¼	5⁄16	5⁄16	5⁄16	¼
C-shaped weld eccentric shear capacity								
Ecc, in.	5.95	5.38	6.72	9.36	7.31	6.51	6.72	11.2
cg, in.	17.6	17.6	17.6	7.14	17.6	17.6	17.6	7.14
e_x, in.	32.4	31.8	33.1	22.2	33.7	32.9	33.1	24.1
k	2.00	2.00	2.00	1.25	2.00	2.00	2.00	1.25
a	1.47	1.44	1.51	1.39	1.53	1.50	1.51	1.51
$C_{8.8}$	4.97	5.04	4.90	2.93	4.81	4.91	4.88	2.74
$P_{weld,V}$, kips	492	499	485	169	477	486	483	158
C-shaped weld tension capacity								
$P_{weld,H}$, kips	735	735	735	267	735	735	735	267
Utilization of weld capacity								
$\frac{V_{c,weld}}{P_{weld,V}}$	0.67	0.65	0.54	0.55	0.60	0.59	0.54	0.53
$\frac{T_{c,weld}}{P_{weld,H}}$	0.50	0.53	0.53	0.62	0.48	0.52	0.53	0.56
Utilization ratio	0.84	0.84	0.75	0.83	0.77	0.78	0.75	0.77

Table 4. Details of Composite Coupling Beam-to-C-PSW/CF Connection Specimens												
Specimen	**Connection Type**	**L_b/d Ratio**	**Coupling Beam Dimensions, in.**					**Wall Dimensions, in.**				
			b_f	**b_i**	**d**	**t_{f_b}**	**t_{w_b}**	**t_{sc}**	**t_{f_w}**	**t_{w_w}**	**H_w**	**L_w**
SP-1	1	5.1	12.875	11.5	12.5	¼	3⁄16	11.5	¼	¼	120	38.5
SP-2	2	5.1	12.875	11.5	12.5	¼	3⁄16	11.5	¼	¼	120	38.5
SP-3	1	3.5	13.25	11.5	12.5	¼	⅜	11.5	¼	¼	120	29.25
SP-4	2	3.5	13.25	11.5	12.5	¼	⅜	11.5	¼	¼	120	29.25
SP-5	3	3.5	12.5	10.75	12.5	¼	⅜	11.5	¼	⅜	120	29.25
SP-6	4	3.5	10.75	10.75	12.5	¼	⅜	11.5	¼	⅜	120	29.25

Coupling beam:

b_f = flange width, in.
b_i = inside-to-inside distance between webs, in.
d =total depth of cross section, in.
t_{f_b} = flange thickness, in.
t_{w_b} = web thickness, in

Specimens SP-1 (connection type 1) and SP-2 (connection type 2), with an approximately square cross section and L_b/d ratio of 5.1, represent the thicker wall web and thinner beam web plate design of archetypes PG-1C and PG-1F. Specimens SP-3 (connection type 1) and SP-4 (connection type 2) represent the thinner wall web and thicker beam web plate design of archetypes PG-2B and PG-2E, but with an approximately square cross section of the beam and an L_b/d ratio of 3.5. Specimens SP-5 (connection type 3) and SP-6 (connection type 4), with L_b/d ratio of 3.5 are representative of archetypes PG-1A and PG-1D, but with an approximately square cross section of the beam and web plate that is of equal thickness and continuous for both the coupling beam and the composite wall. Fabrication drawings of all six specimens are presented in Figures 11 and 12.

Design of Test Specimens

The C-PSW/CF, coupling beam, and the connection between the two members were designed following the requirements in ANSI/AISC 360-22 and ANSI/AISC 341-22, which are also described in detail in AISC Design Guide 38.

Design of C-PSW/CF

The steel plates were designed to comprise between 1% and 10% of the total composite cross section, as specified in ANSI/AISC 360-22, Section I1.6. The opposite web plates were connected using tie bars, and the tie bars and stud anchors also anchored the plates to the concrete infill. In accordance with ANSI/AISC 341-22, Section H7.5a, the steel plates must be nonslender—that is, yielding in compression occurs before local buckling, which can be achieved using Equation 15.

$$\frac{b}{t_p} \le 1.05\sqrt{\frac{E_s}{R_y F_y}} \tag{15}$$

where

b = largest unsupported length of the plate between rows of steel anchors or ties, in.
t_p = steel plate thickness of C-PSW/CF wall webs, identified as t_{w_w} in Figure 10, in.

The maximum allowable tie bar spacing is limited to 1.0 times the wall thickness, t_{sc}, per ANSI/AISC 360-22, Section I1.6b. Additionally, the detailing of the empty steel modules (before concrete casting) in terms of the maximum slenderness ratio for the steel plates (S/t_p) and the tie bar diameter and spacing are limited to provide adequate shear stiffness and stability using Equation 16, developed by Varma et al. (2019), and required by ANSI/AISC 360-22, Section I1.6b.

$$\frac{S}{t_p} \le 1.0\sqrt{\frac{E_s}{2\alpha + 1}} \tag{16}$$

$$\alpha = 1.7\left(\frac{t_{sc}}{t_p} - 2\right)\left(\frac{t_p}{d_{tie}}\right)^4 \tag{17}$$

where

S = largest clear spacing of the ties, in.
d_{tie} = effective diameter of the tie, in.

Tie bars of low carbon ASTM A1018/A1018M steel, with ½ in. diameter, were uniformly spaced at 6 in. in both directions. They were welded to the wall web plates using 5⁄16 in. fillet welds around the circumference of the bar on the outside of wall web plates to develop the full yield strength of the tie bar. Table 5 shows the section details of the wall to be within limits prescribed by the design code.

Design of Composite Coupling Beam

The cross-section areas of the steel elements were designed to be greater than 1% of the total composite cross section, per ANSI/AISC 360-22, Section I2.2a. The section was

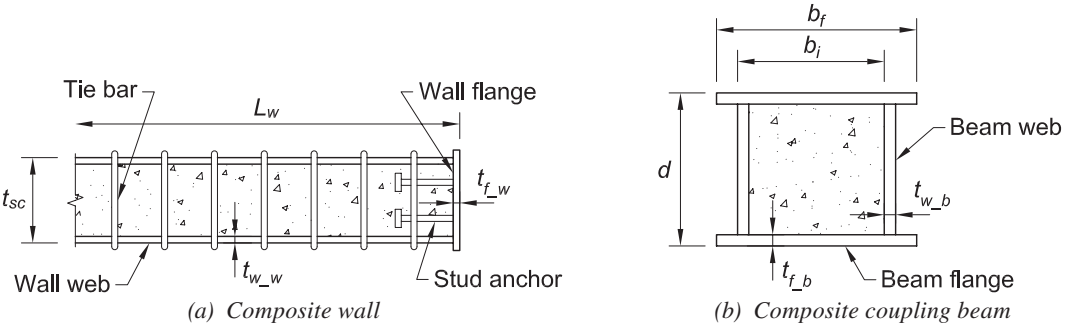

(a) Composite wall *(b) Composite coupling beam*

Fig. 10. Cross-section details of specimens.

Table 5. Section Details of C-PSW/CF						
Specimen	Percentage of Steel	$\frac{b}{t_p}$	$1.05\sqrt{\frac{E_s}{R_yF_y}}$	$\frac{S}{t_p}$	α	$1.0\sqrt{\frac{E_s}{2\alpha+1}}$
SP-1	4.7%	24.0	24.3	24.0	4.70	52.9
SP-2	4.7%	24.0	24.3	24.0	4.70	52.9
SP-3	4.7%	24.0	24.3	24.0	4.70	52.9
SP-4	4.7%	24.0	24.3	24.0	4.70	52.9
SP-5	6.9%	16.0	24.3	16.0	15.4	30.2
SP-6	6.9%	16.0	24.3	16.0	15.4	30.2

Table 6. Section Details of Composite Coupling Beams									
Specimen	Percentage of Steel	$\frac{b_c}{t_{f\_b}}$	$2.37\sqrt{\frac{E_s}{R_yF_y}}$	$\frac{h_c}{t_{w\_b}}$	$2.66\sqrt{\frac{E_s}{R_yF_y}}$	L_b, in.	$M_{p,exp}$, kip-in.	$\frac{1.2(2M_{p,exp})}{L_b}$, kips	$V_{n,exp}$, kips
SP-1	7.4%	46.0	54.9	64*	61.6	31.25	3290	126	156
SP-2	7.4%	46.0	54.9	64*	61.6	31.25	3290	126	156
SP-3	10.2%	46.0	54.9	32	61.6	21.0	4262	244	313
SP-4	10.2%	46.0	54.9	32	61.6	21.0	4262	244	313
SP-5	10.6%	43.0	54.9	32	61.6	21.0	4034	231	307
SP-6	10.7%	43.0	54.9	32	61.6	21.0	3687	211	322

* The ratio of $\frac{h_c}{t_{w\_b}}$ is slightly higher than the slenderness limit, but it was deemed to be adequate for these tests.

designed to be compact with slenderness ratios of flanges and webs limited per Equations 18 and 19 in accordance with ANSI/AISC 341-22, Section H8. The web slenderness requirement is established to develop the shear yield strength before shear buckling. The flange slenderness requirement is established to develop the compression yield strength before elastic buckling.

$$\frac{b_c}{t_{f\_b}} \le 2.37\sqrt{\frac{E_s}{R_yF_y}} \tag{18}$$

$$\frac{h_c}{t_{w\_b}} \le 2.66\sqrt{\frac{E_s}{R_yF_y}} \tag{19}$$

where

b_c = clear unsupported width of the coupling beam flange plate, in.

h_c = clear unsupported width of the coupling beam web plate, in.

The section was proportioned to be flexure-critical by designing the shear strength to be greater than the capacity-limited shear due to the expected flexural capacity, as shown in Equation 20, which is in accordance with ANSI/AISC 341-22, Section H8.8. The capacity-limited shear force is increased by 1.2 to account for steel inelastic hardening, concrete confinement, and the biaxial (tensile) stress state in the steel tension flange.

Table 6 shows the structural characteristics of the composite coupling beams to be within the limits prescribed by ANSI/AISC 341-22, Section H8.

$$V_{n,exp} \ge \frac{1.2(2M_{p,exp})}{L_b} \tag{20}$$

where

L_b = clear span length of the coupling beam, in.

$M_{p,exp}$ = expected flexural capacity of composite coupling beam calculated using the plastic stress distribution method specified in ANSI/AISC 360-22, Section I1.2, while using the expected yield strength for steel, R_yF_y, and the expected compressive strength, R_cf_c', for concrete, kip-in.

$V_{n,exp}$ = expected shear strength of composite coupling beam calculated per ANSI/AISC 360-22, Section I4.2, while using expected yield strength, R_yF_y, for steel, and expected compressive strength, R_cf_c', for concrete, kips

Table 7. Coupling Beam Flange-to-Wall Web Connection Calculations for CC-PSW/CF Specimens				
Case	**SP-1, SP-2**	**SP-3, SP-4**	**SP-5**	**SP-6**
Flange plate connection demand				
$1.2R_yF_yA_{f\_CB}$, kips	209	215	203	174
$R_tF_uA_{f\_CB}$, kips	232	239	225	194
T_{flange}, kips	209	215	203	174
Length of weld/flange embedment length				
L_{req}, in.	10.75	10.0	9.4	16.1**
$L_{provided}$, in.	12.5	12.5	12.5	12.5
Shear strength of beam flange plates				
$\phi_d 0.6R_yF_yA_{f\_SY}$, kips	101***	101***	101	101
$\phi_n 0.6R_tF_uA_{f\_SR}$, kips	122	122	122	122
$\frac{T_{flange}}{2}$, kips	104	107	101	87
Shear strength of wall web plates				
$\phi_d 0.6R_yF_yA_{w\_SY}$, kips	203	203	304	304
$\phi_n 0.6R_tF_uA_{w\_SR}$, kips	243	243	365	182
$\frac{T_{flange}}{2}$, kips	104	107	101	87

** Designed for F_y = 50 ksi, but the calculations are presented for 36 ksi. The length of weld provided (equal to 1.0*d*) satisfies the requirement for minimum length when calculated using the measured F_y of 48 ksi. The calculation should be performed for a range of yield strengths for an actual structure. The plates procured should be required to have measured yield strength within the checked limits to ensure that the beam and wall elements yield in sequence, as intended during the design process.

*** The shear yield strength of the coupling beam flange plates is lower but close to the value required to transfer half the tension in the flange, thus the length of weld provided (equal to 1.0*d*) was deemed to be adequate.

Design of Connections

Connections at the section level and at the member level were designed for the specimens. At the section level, tie bar-to-steel plate connections, coupling beam flange-to-web connections, and wall flange-to-web connections were sized. The tie bars-to-steel plate connection was designed to develop the yield strength of the bar in tension, using 5⁄16 in. welds going around the bar's circumference on the outside of wall web plates. The flange-to-web connections in the beam and wall were designed to develop the expected yield strength of the weaker base metal plate. Flange-to-web connections in the wall utilized ¼ in. fillet welds. For flange-to-web welds in the beam, complete joint penetration groove welds were used for the specimens with an L_b/d ratio of 3.5 and ¼ in. fillet welds for specimens with an L_b/d ratio of 5.1. Although the connection was required to develop the full yield strength of the base metal, the specimens were smaller-scaled versions of the archetypes, and the thin 3⁄16 in. plate would distort excessively due to the heat from groove welding. Consequently, fillet welds were adopted as they fused through the thickness of 3⁄16 in. plates and effectively provided complete joint penetration. The coupling beam-to-C-PSW/CF connections were designed at the member level using methods presented earlier in the design of connections for archetype structures.

Coupling Beam Flange-to-Wall Web Connection

For specimens with L_b/d ratio of 3.5 (SP-3, SP-4, SP-5, SP-6), prequalified CJP weld configuration TC-U4a-GF was used to connect the beam flange to the wall web. The wider flange plate going inside the slots in wall web (SP-3, SP-4, and SP-5) was welded on two sides, as shown in Figures 3 and 5. The narrow flange plate fitted inside the wall thickness (SP-6) was welded on one side, as shown in Figure 6. The backing bars were left in place. Fillet welds were used for specimens with an L_b/d ratio of 5.1 (SP-1, SP-2). Sample calculations for the specimen beam flange-to-wall web connections are presented in Table 7. The calculations were performed using F_y and F_u values of 36 and 60 ksi, respectively. For specimens with a wider flange plate, half-an-in. of overhang was considered on each side of the beam flange to provide clearance for welding. Potential shear yielding and rupture planes for the coupling beam flange and wall web plates for connection types 1 and 2

Table 8. Coupling Beam Web-to-Wall Web Connection Calculations for CC-PSW/CF Specimens		
Case	**SP-1, SP-2**	**SP-3, SP-4**
Forces in beam web plates		
T_{web}, kips	200	304
M_{web}, kip-in.	465	1275
V_{web}, kips	129	252
Force demand on C-shaped weld		
$T_{c,\ weld}$, kips	100	152
$M_{c,\ weld}$, kip-in.	233	637.5
$V_{c,\ weld}$, kips	65	126
Weld geometry		
$L_{web,V,weld}$, in.	18.0	20.0
$L_{web,H,weld}$, in.	10.0	10.0
w, in.	3/16	5/16
C-shaped weld shear and moment capacity		
Ecc, in.	3.60	5.06
cg, in.	7.04	8.00
e_x, in.	14.56	17.06
k	1.80	2.00
a	1.46	1.71
$C_{8.8}$	4.21	4.41
$P_{weld,V}$, kips	114	198
C-shaped weld tension capacity		
$P_{weld,H}$, kips	180	334
Utilization of weld capacity		
$\frac{V_{c,weld}}{P_{weld,V}}$	0.57	0.64
$\frac{T_{c,weld}}{P_{weld,H}}$	0.55	0.46
Utilization ratio	0.79	0.78

are shown in Figure 7. Multiple yielding and rupture planes can be checked; Table 7 summarizes the limits for the cases presented.

Coupling Beam Web-to-Wall Web Connection

The coupling beam web-to-wall web connections were designed for Specimens SP-1, SP-2, SP-3, and SP-4 in accordance with Figures 8 and 9 and Equations 7 to 14, which were described earlier for the archetype structure connection design. All the corresponding calculations for Specimens SP-1 and SP-2 with length-to-depth ratio of 5.1 and Specimens SP-3 and SP-4 with length-to-depth ratio of 3.5 are provided in Table 8 along with the designed weld geometry. For Specimens SP-5 and SP-6, the coupling beam webs and wall webs were one continuous plate.

Fabrication Drawings

Figure 11 shows the elevation, section views, and weld details of specimens SP-1 and SP-3 (connection type 1) and specimens SP-2 and SP-4 (connection type 2). Figure 12 presents the same for specimens SP-5 (connection type 3) and SP-6 (connection type 4). The embedment length for the coupling beam flange and the lap length for the coupling beam web is also identified. The flange embedment

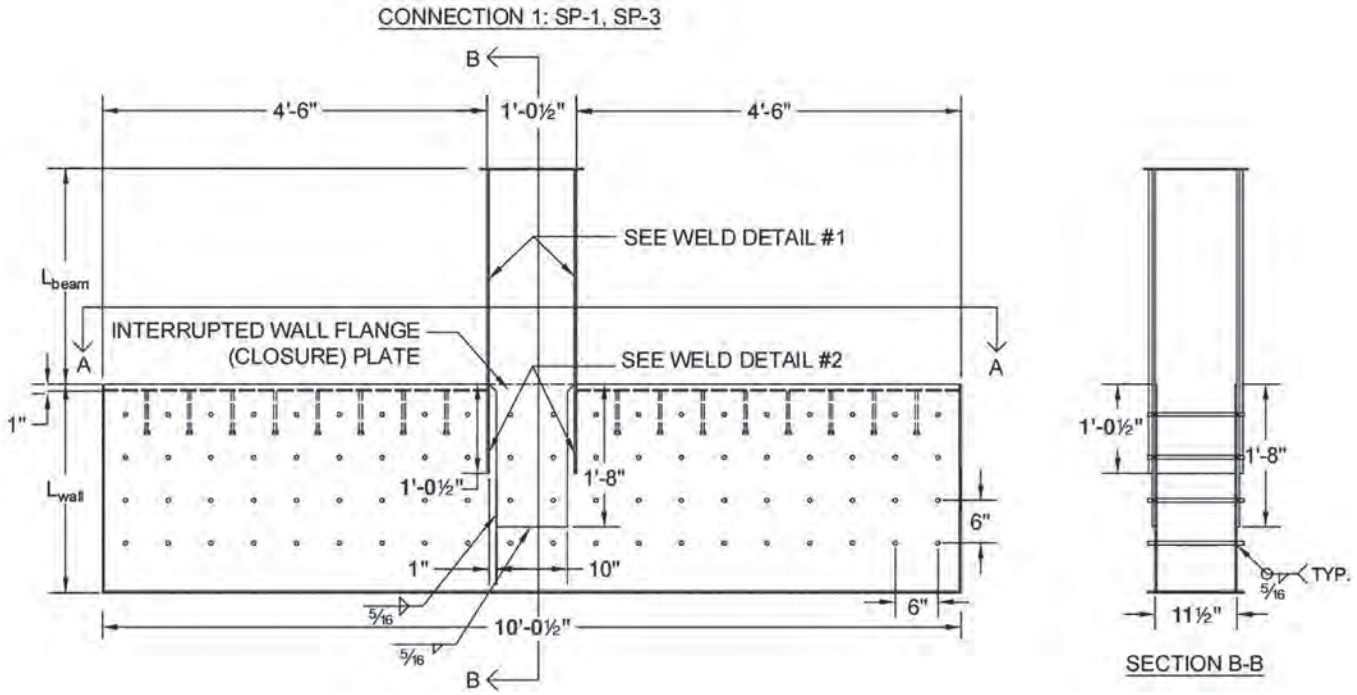

(a) Specimens SP-1 and SP-3

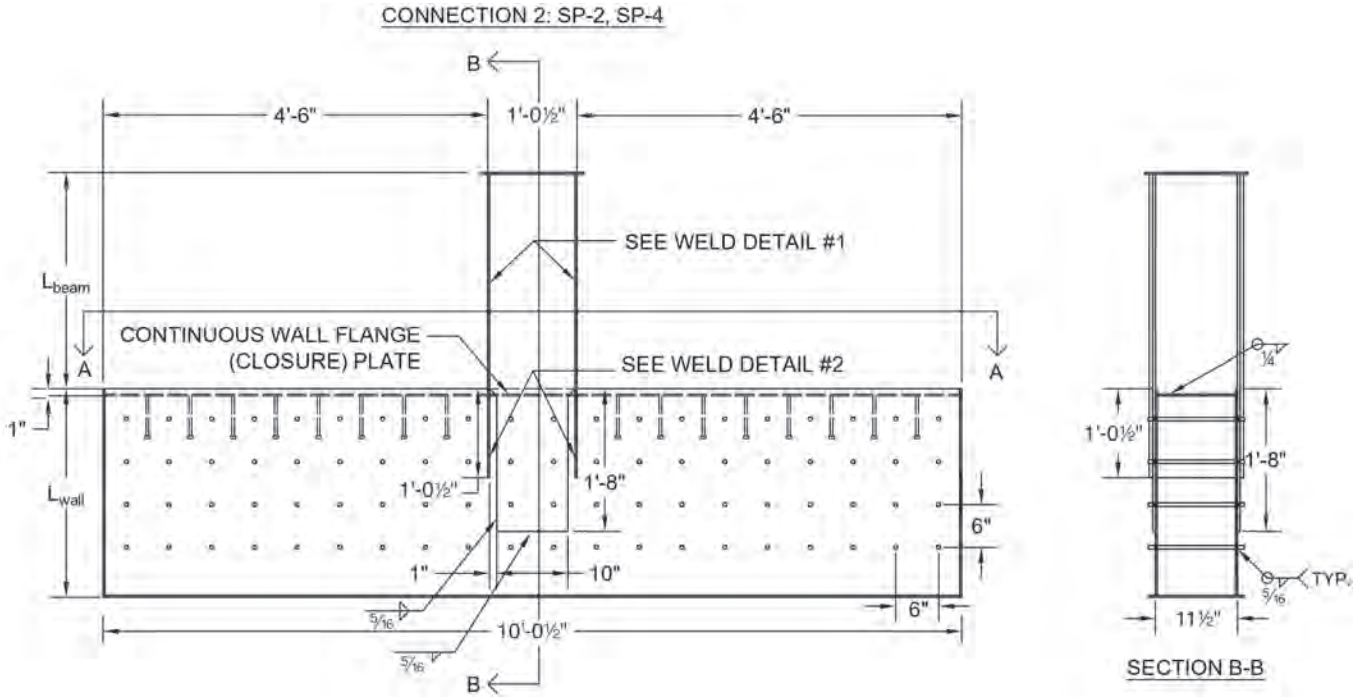

(b) Specimens SP-2 and SP-4

Fig. 11. Fabrication drawings—elevation and side view of specimens.

length was equal to the beam depth (d = 12.5 in.) for all connection types. A beam web-to-wall web lap length of 20 in. was provided for specimens with separate web plates for the beam and wall. The weld details and top section view for the connection are also shown in Figures 11 and 12.

For all connection types, specimens with an L_b/d ratio of 3.5 (SP-3, SP-4, SP-5, and SP-6) utilized prequalified CJP weld configuration TC-U4a-GF for the beam flange-to-beam web and beam flange-to-wall web connection. After welding, the backing bars were left in place. For specimens with L_b/d ratio of 5.1 (SP-1, SP-2), fillet welds were used for the beam flange-to-beam web and beam flange-to-wall web connections. The wall web was cut to receive the coupling beam flange plates at four locations. The plates making up the wall panel were connected using nominal ¼ in. fillet welds as the stresses away from the connection region were expected to be minimal.

TEST SETUP

Figure 13 shows a schematic of the test setup used for conducting the coupling beam-to-wall connection experiments. The composite wall was post-tensioned to the laboratory strong floor using high-strength post-tensioning bars. The

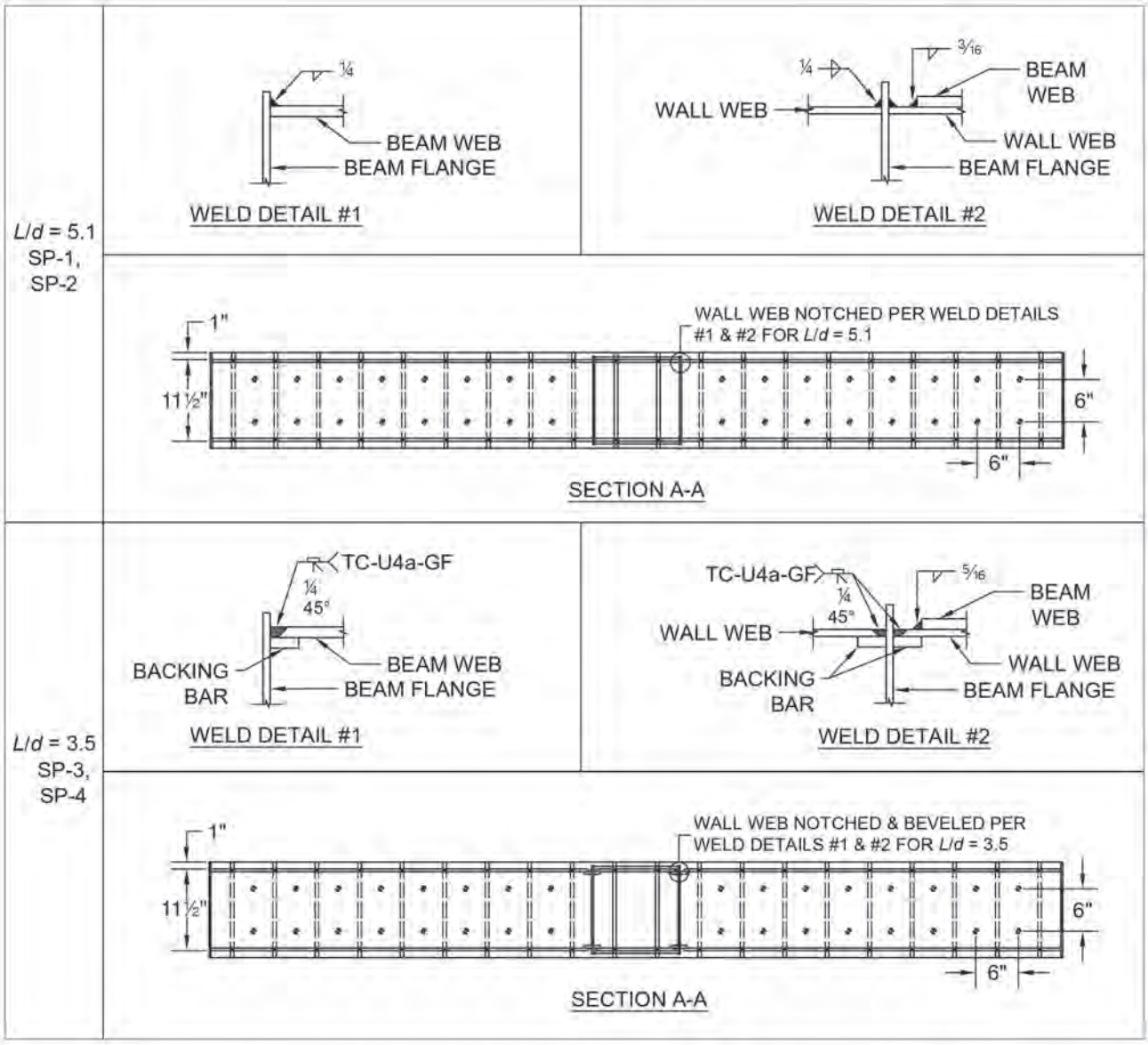

(c) Top view and connection details

Fig. 11. Fabrication drawings—elevation and side view of specimens (continued).

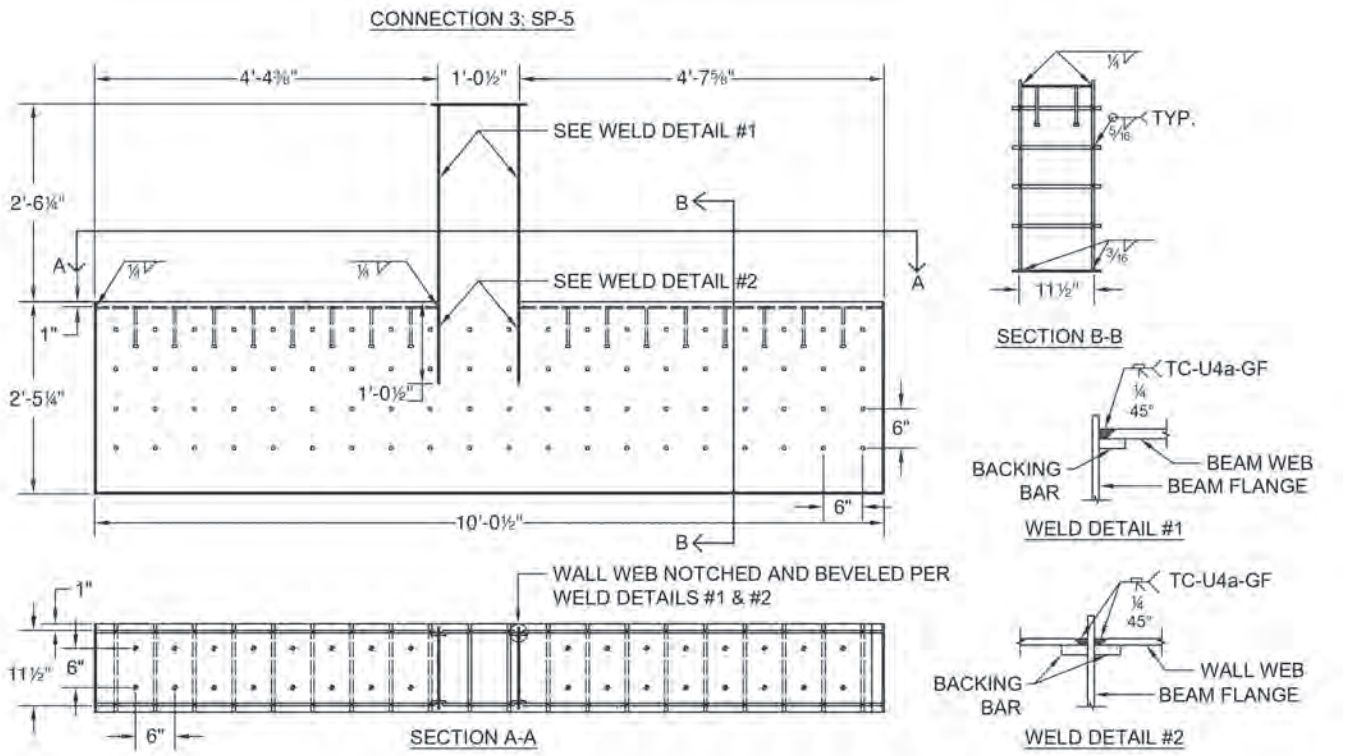

(a) Specimen SP-5

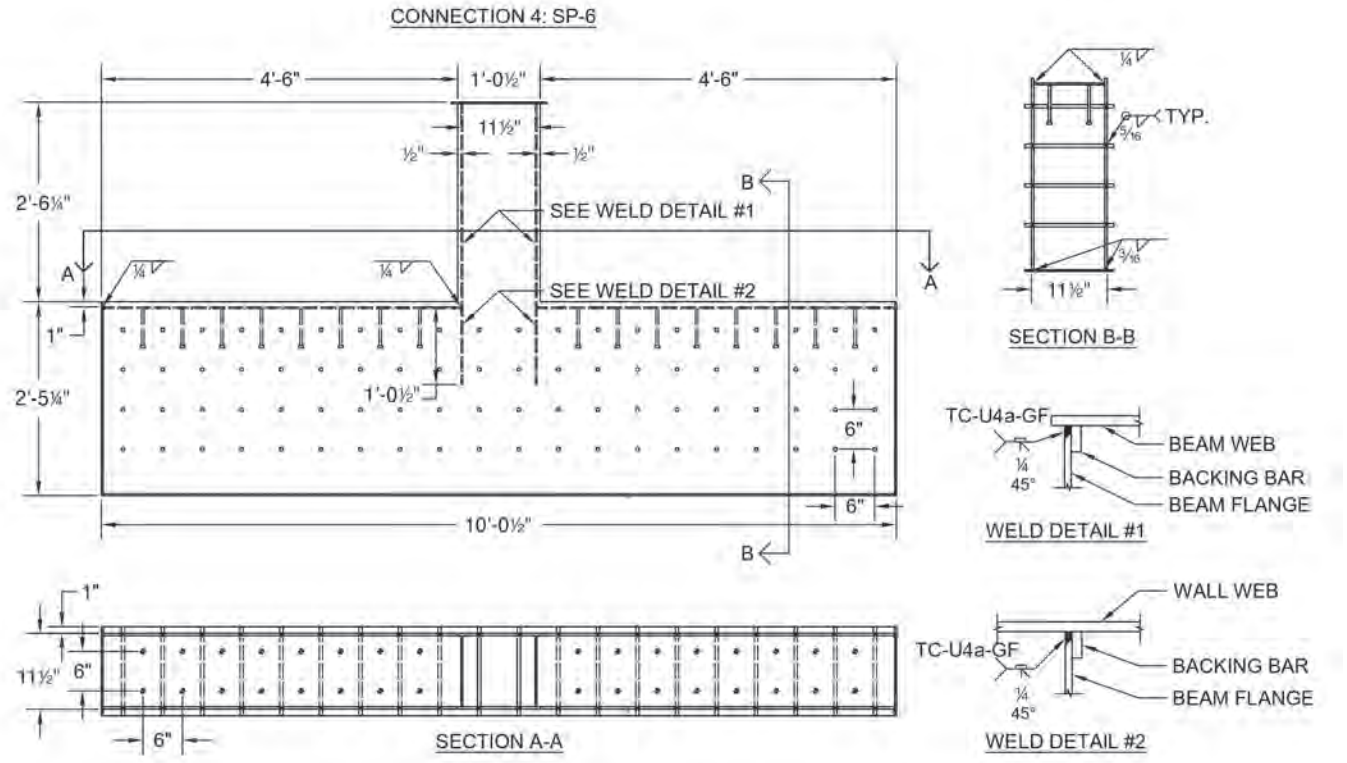

(b) Specimen SP-6

Fig. 12. Elevation, side, top views, and connection details of specimens.

coupling beam end was subjected to quasi-static lateral cyclic loading in accordance with the ATC-24 single specimen loading protocol (ATC, 1992). The lateral load was applied at the height of 31.875 in. or 21.75 in. from the top of the wall flange (closure) plate, thus achieving an L_b/d ratio of 5.1 or 3.5, respectively. Details of the experimental test setup are not presented here for brevity. They are presented in detail in Varma et al. (2021).

EXPERIMENTAL RESULTS AND OBSERVATIONS

Cyclic Response of Composite Coupling Beam-to-C-PSW/CF Connection

This section briefly presents the experimental behavior of one coupling beam-to-C-PSW/CF connection specimen (Specimen SP-1, connection type 1). The cyclic normalized moment-chord rotation response of specimen SP1 is shown in Figure 14. The moment, M, was calculated at the base of the coupling beam and normalized with respect to the nominal plastic moment capacity, M_p, of the coupling beam calculated using measured material properties and dimensions. Chord rotation, θ, was estimated by dividing the lateral displacement, Δ, at the point of load application by h, which is the coupling beam length between its base and the center point of load application. The figure includes (1) horizontal dashed lines corresponding to 80% of the nominal plastic moment capacity, M_p, and (2) vertical dashed lines corresponding to 0.03 rad chord rotation. Strain gauge data showed that all inelasticity occurred in the coupling beam flange and web, in the plastic hinge region that formed next to the connection region, and in the wall remained essentially elastic until the end of the test.

The behavior of specimen SP-1 was as follows according to the experimental observations and measurements. The cyclic lateral load-displacement response was approximately linear during the elastic cycles. The coupling beam infill concrete cracked in tension during the first elastic cycle, at a lateral force corresponding to 14% of the flexural capacity, M_p. Strain gauge data showed yielding of the beam flange and web plates in tension during the $1.0\Delta_y$ and $1.5\Delta_y$ cycles, respectively. Δ_y is defined as the peak displacement of the first inelastic cycle, projected from the displacement corresponding to the maximum elastic force level. Yielding was also confirmed by the flaking of whitewash applied to

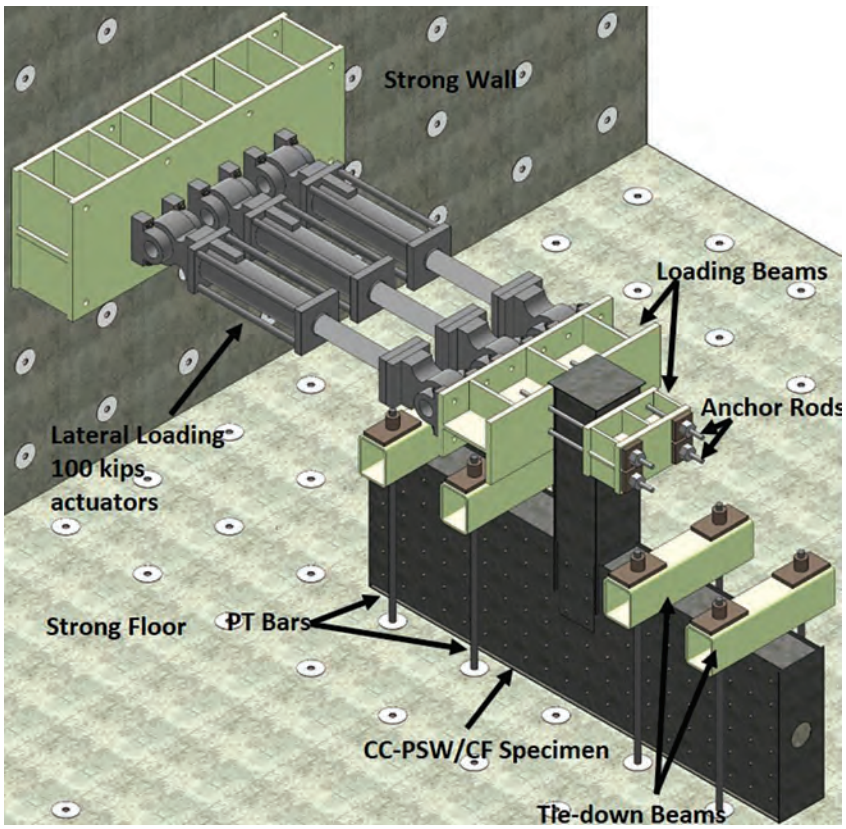

Fig. 13. Schematic view of the test setup.

the surface of steel plates in the connection region. Local buckling of compression flange was visually observed during the $2\Delta_y$ cycles, which was also confirmed by strain gauge results. The maximum flexural capacity was reached during the $2\Delta_y$ cycles. Steel fracture initiated in the base metal of the beam flange-to-wall web and the beam web-to-wall web welded connections during the 1 to $2\Delta_y$ cycles. The fracture propagated further in the beam flange and web plates during the $3\Delta_y$ cycles, which resulted in reduction of lateral load resistance in subsequent cycles. Extensive local bucking of flanges occurred during the 3, 4, and $5\Delta_y$ cycles. The beam flanges completely fractured under tension during the $5\Delta_y$ cycles.

Figure 15 shows the condition of connection at the end of the test. The whitewash was removed to get clear photographs of fracture at the end of the test. As shown in Figure 14, the average flexural capacity of the connection at chord rotation of 0.03 rad was higher than $0.8M_p$. The connection was thus deemed to satisfy the requirement of at least 0.03 chord rotation at 80% of the nominal plastic moment capacity M_p, specified by ANSI/AISC 341-22.

Comparison of Moment-Rotation Response for All Specimens

Figures 16(a)–16(e) present the cyclic, normalized moment-chord rotation responses of the remaining five specimens. These figures include horizontal lines corresponding to 80% of the nominal plastic moment capacity, M_p, calculated using plastic stress distribution method and vertical lines corresponding to the chord rotation of 0.03 rad. For each specimen, the envelopes of cyclic moment-rotation (M-θ) responses in each direction (push and pull) were developed and averaged. The backbone curve was developed by selecting the peaks of the first cycle at each force/displacement level. The push and pull curves comprised of the discrete peak points were then averaged. Figure 16(f) shows (and compares) these averaged normalized backbone moment-rotation (M-θ) curves for all specimens. As shown, the experimental capacities of all specimens exceeded the flexural capacities calculated using the plastic stress distribution method and measured material properties. All the coupling beam-to-C-PSW/CF connections developed chord-rotation capacities greater than 0.03 rad before the flexural strength degraded below 80% of M_p. The flexural capacities of the specimens were between 1.05 and 1.40 times the plastic flexural capacities of the composite coupling beams calculated using measured material properties.

CONCLUSIONS

Four different types of composite coupling beam-to-C-PSW/CF connections were developed and proposed

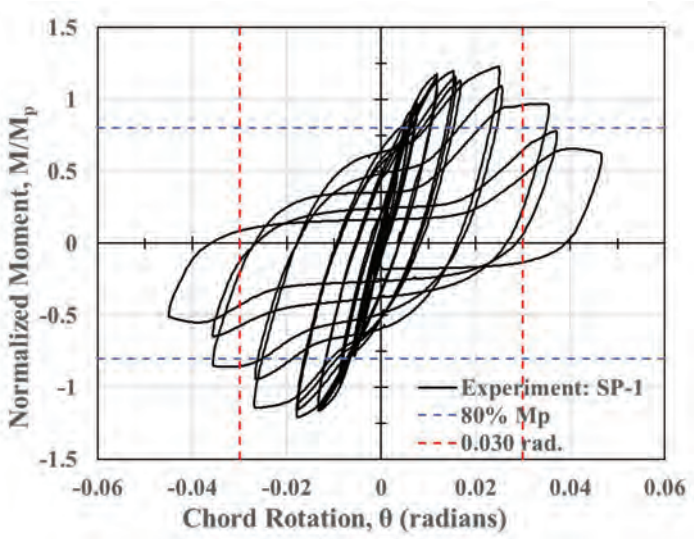

Fig. 14. Normalized moment—chord rotation curve of specimen SP-1 (connection type 1).

(a) North flange

(b) South flange

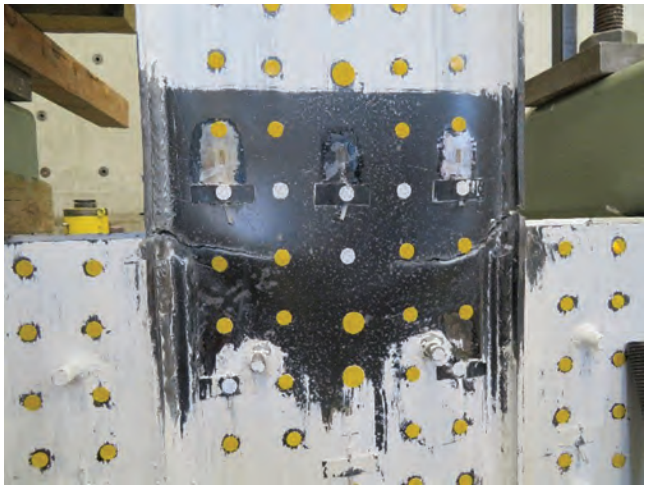

(c) East web

(d) West web

Fig. 15. End of test of SP-1 showing local buckling and fracture.

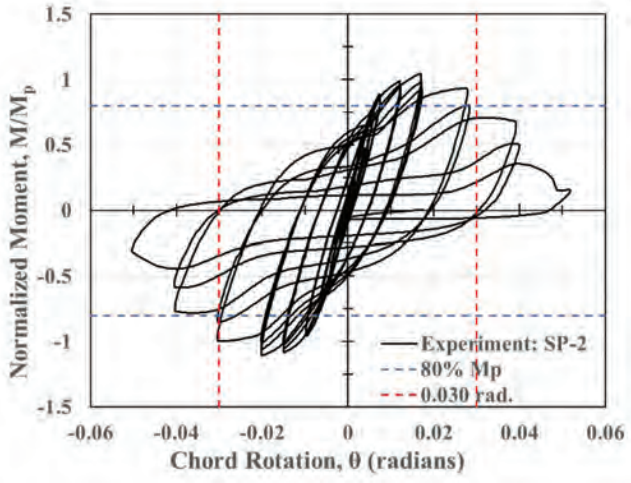

(a) Specimen SP-2

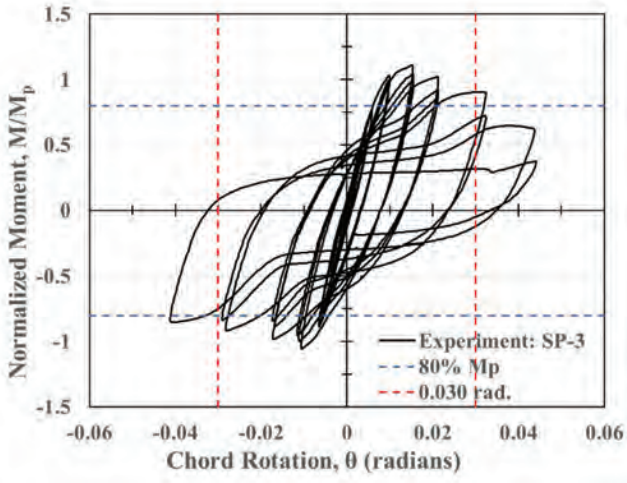

(b) Specimen SP-3

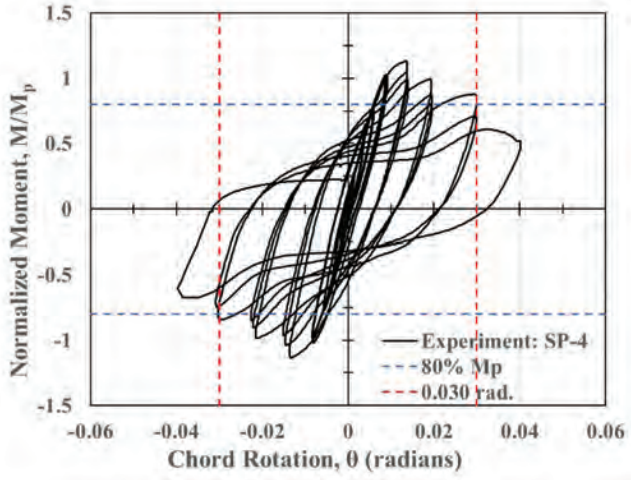

(c) Specimen SP-4

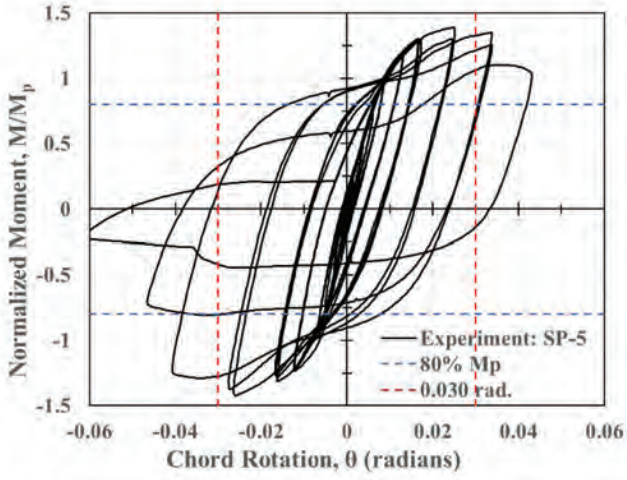

(d) Specimen SP-5

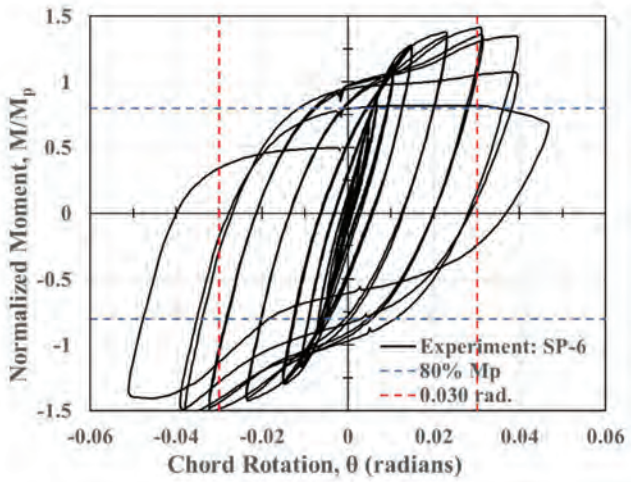

(e) Specimen SP-6

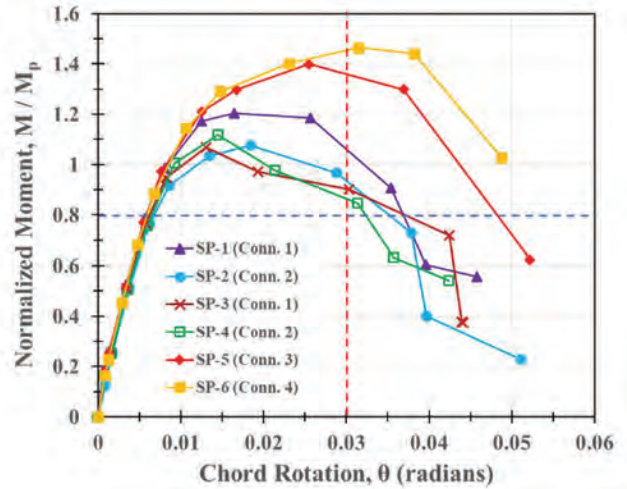

(f) Average backbones of all six specimens

Fig. 16. Normalized moment-chord rotation curves.

based on structural performance requirements and constructability considerations. The structural performance requirements for the connections were to (1) develop the flexural capacity (and associated shear force) of the coupling beams; (2) develop flexural plastic hinges at the connected ends of the coupling beams; and (3) develop chord rotation of at least 0.03 rad before the flexural resistance reduces to less than 80% of the nominal plastic moment capacity, M_p, of the coupling beam. The paper presented the design, details, and experimental evaluation of the cyclic performance of the proposed connections:

1. Connection types 1, 2, and 3 consist of wider beam flange plates going through slots in the wall web plates. Connection type 4 had a narrow beam flange fitted inside the wall thickness.
2. Connection types 1 and 2 had separate web plates for the wall and beam. The beam web plates were lapped and welded to the wall web plates from the outside. Connection types 3 and 4 had continuous web plates for the beam and wall.
3. The difference between the two connection types (1 and 2) was the continuity of the wall flange (closure) plate. The wall flange (closure) plate was interrupted at the connection leading to monolithic concrete in the wall and beam for connection type 1. The wall flange (closure) plate was continuous at the connection leading to interrupted concrete in the wall and beam for connection type 2.
4. Six composite coupling beam-to-composite wall connection specimens representing the four connection types were tested under cyclic loading. These specimens had composite coupling beam clear span-to-depth (L_b/d) ratios of 3.5 or 5.1.
5. Experimental results indicate that all six connections developed and exceeded the plastic flexural capacities (and associated shear force) of the composite coupling beams, calculated using measured material properties. The flexural capacities of the specimens were between 1.05–1.40 times the plastic flexural capacities of the composite coupling beams calculated using measured material properties.
6. All six connection specimens developed rotation capacity (as measured by chord rotation) greater than 0.03 rad before the flexural resistance degraded to 80% of the nominal plastic moment capacity, M_p, of the coupling beams.

In summary, all four connection types satisfied all the structural seismic performance requirements and can be utilized for connecting composite coupling beams to composite plate shear walls in CC-PSW/CF systems.

ACKNOWLEDGMENTS

The research presented in this paper was supported by the Charles Pankow Foundation and the American Institute of Steel Construction. The opinions expressed in the paper belong to the authors alone. The specimens were fabricated and donated by Geiger & Peters. These research results were also summarized and included in part of Professor Amit Varma's 2021 T. R. Higgins lecture titled, "Steel-Concrete Composite Construction: The Best of Both Worlds." The authors acknowledge the significant contributions of the members of the research advisory panel and Bowen Laboratory researchers and technicians.

REFERENCES

AISC (2016), *Seismic Provisions for Structural Steel Buildings*, ANSI/AISC 341-16, American Institute of Steel Construction, Chicago, Ill.

AISC (2022a), *Seismic Provisions for Structural Steel Buildings*, ANSI/AISC 341-22, American Institute of Steel Construction, Chicago, Ill.

AISC (2022b), *Specification for Structural Steel Buildings*, ANSI/AISC 360-22, American Institute of Steel Construction, Chicago, Ill.

AISC (2023), *Steel Construction Manual*, 16th Ed., American Institute of Steel Construction, Chicago, Ill.

ASCE (2016), *Minimum Design Loads and Associated Criteria for Buildings and Other Structures*, ASCE/SEI 7-16, American Society of Civil Engineers, Reston, Va.

ASCE (2022), *Minimum Design Loads and Associated Criteria for Buildings and Other Structures*, ASCE/SEI 7-22, American Society of Civil Engineers, Reston, Va.

ATC (1992), *Guidelines for Cyclic Seismic Testing of Components of Steel Structures*, Applied Technology Council, Redwood City, Calif.

Broberg, M., Agrawal, S., Varma, A., and Klemencic, R. (2023), "Seismic Design Parameters (R, C_d, and Ω_0) for Uncoupled Composite Plate Shear Walls—Concrete Filled (C-PSW/CF)," *Earthquake Engineering and Structural Dynamics*, Vol. 52, No. 10, pp. 3,149–3,170.

Broberg, M., Shafaei, S., Kizilarslan, E., Seo, J., Varma, A.H., Bruneau, M., and Klemencic, R. (2022), "Capacity Design of Coupled Composite Plate Shear Walls/Concrete Filled (CC-PSW/CF)," *Journal of Structural Engineering*, ASCE, Vol. 148, No. 4.

Bruneau, M., Varma, A.H., Kizilarslan, E., Broberg, M.R., Shafaei, S., and Seo, J. (2019), "R-Factors for Coupled Composite Plate Shear Walls/Concrete Filled (CC-PSW/CF)," Final Report, Project #05-17, Charles Pankow Foundation and American Institute of Steel Construction, accessed January 1, 2020.

El-Tawil, S., Fortney, P., Harries, K., Shahrooz, B., Kurama, Y., Hassan, M., and Tong, X. (2010), "Recommendations for Seismic Design of Hybrid Coupled Wall Systems," ASCE, Reston, Va.

Farsi, A., Keshavarzi, F., Pouladi, P., and Mirghaderi, R. (2016), "Experimental Study of a Replaceable Steel Coupling Beam with an End-Plate Connection," *Journal of Constructional Steel Research*, Vol. 122, pp. 138–150.

FEMA (2020), *NEHRP Recommended Seismic Provisions for New Buildings and Other Structures, Volume I: Part 1 Provisions, Part 2, Commentary*, FEMA P-2082-1, Federal Emergency Management Agency, Washington, D.C.

FEMA (2021), *2020 NEHRP Recommended Seismic Provisions: Design Examples, Training Materials, and Design Flow Charts: Volume I: Design Examples*, FEMA P-2192-V1, Federal Emergency Management Agency, Washington, D.C.

Gong, B. and Shahrooz, B.M. (2001), "Concrete-Steel Composite Coupling Beams. I: Component Testing," *Journal of Structural Engineering*, ASCE, Vol. 127, No. 6, pp. 625–631.

Kizilarslan, E., Broberg, M., Shafaei, S., Varma, A.H., and Bruneau, M. (2021a), "Non-Linear Analysis Models for Composite Plate Shear Walls—Concrete Filled (C-PSW/CF)," *Journal of Constructional Steel Research*, Vol. 184.

Kizilarslan, E., Broberg, M., Shafaei, S., Varma, A.H., and Bruneau, M. (2021b), "Seismic Design Coefficients and Factors for Coupled Composite Plate Shear Walls/Concrete Filled (CC-PSW/CF)," *Engineering Structures*, Vol. 244.

Kizilarslan, E. and Bruneau, M. (2023), "Verification of Seismic Response Modification Factors of Uncoupled Composite Plate Shear Walls/Concrete-Filled (C-PSW/CF)," *Journal of Structural Engineering*, ASCE, Vol. 149, No. 6.

Nie, J.G., Hu, H.S., and Eatherton, M.R. (2014), "Concrete Filled Steel Plate Composite Coupling Beams: Experimental Study," *Journal of Constructional Steel Research*, Vol. 94, pp. 49–63.

Shafaei, S., Varma, A.H., Broberg, M., and Klemencic, R. (2021a), "Modeling the Cyclic Behavior of Composite Plate Shear Walls/Concrete Filled (C-PSW/CF)," *Journal of Constructional Steel Research*, Vol. 184.

Shafaei, S., Varma, A.H., and Klemencic, R. (2021b), "Cyclic Lateral Loading Behavior of Composite Plate Shear Walls/Concrete Filled," *Journal of Structural Engineering*, ASCE, Vol. 147, No. 10.

Traut-Todaro, J. (2019), "SpeedCore, Lateral System Innovation for Today's Construction Challenges," *Modern Steel Construction*, AISC, November.

Varma, A.H., Ahmad, M., Shafaei, S., and Bradt, T. (2021), "Seismic Design and Behavior of Composite Coupling Beam-to-C-PSW/CF Connections," Final Report, Project #06-16, Charles Pankow Foundation and American Institute of Steel Construction.

Varma, A.H., Broberg, M., Shafaei, S., and Taghipour, A.A. (2023), *SpeedCore Systems for Steel Structures*, Design Guide 38, AISC, Chicago, Ill.

Varma, A H., Malushte, S.R., Sener, K.C., and Lai, Z. (2014), "Steel-Plate Composite (SC) Walls for Safety Related Nuclear Facilities: Design for In-Plane Forces and Out-of-Plane Moments," *Nuclear Engineering and Design*, Vol. 269, pp. 240–249.

Varma, A.H., Shafaei, S., and Klemencic, R. (2019), "Steel Modules of Composite Plate Shear Walls: Behavior, Stability, and Design," *Thin-Walled Structures*, Vol. 145.

Inelastic Deformation and Local Slenderness Requirements for Rectangular HSS Braces

Dawn Lehman, Charles Roeder, William Bergendahl, Joseph Kaldestad, Andrew Sen, and Jeffrey W. Berman

ABSTRACT

Rectangular hollow structural sections (HSS) are commonly used as bracing in concentrically braced frames (CBFs) designed and detailed for seismic design requirements. As the primary yielding component in CBFs, braces are expected to sustain large inelastic axial deformation during earthquake loading. It is well known that their deformation capacity depends on the width-to-thickness ratio (local slenderness). Until 2013, HSS sections were produced to meet ASTM standard A500/A500M; after 2013, the ASTM 1085 specification was implemented, and since that time, HSS sections have also been produced to meet ASTM A1085/A1085M standards. Where the ASTM A500/A500M specification requires minimum yield and tensile stress values as well as a minimum elongation and tolerances on the wall thickness, the ASTM A1085/A1085M specification also requires a minimum Charpy V-notch (CVN) toughness, a maximum yield stress of the steel, and tighter tolerances on the wall thickness and radius of curvature of the corner. These requirements offer a more reliable brace for CBFs in seismic regions. Yet there has been limited research investigating the cyclic axial response of these members. A research study was undertaken to investigate the response of ASTM A1085/A1085M tubes using the response of ASTM A500C tubes as their reference. Forty-one brace specimens were tested under cyclic inelastic axial deformation. Comparison of the data shows that most of the ASTM A500/A500 M Grade C and ASTM A1085/1085M braces meet the respective requirements of their respective ASTM standard and that the differences between the performance of ASTM A500/A500M and ASTM A1085/1085M braces are not dramatic. In addition, the study investigated the impact of width-to-thickness ratio, global slenderness, and displacement history on the response of the braces. The data show that the current AISC 341-22 high-ductility slenderness limit for special concentrically braced frame (SCBF) braces is slightly conservative. However, the data suggest that the moderate ductility slenderness limit used for ordinary concentrically braced frame (OCBF) braces is significantly more conservative than required for consistent seismic safety. Further research is required to determine appropriate limits; this paper provides some initial recommendations based on this dataset.

Keywords: highly ductile, moderately ductile, concentrically braced frame, HSS brace, inelastic deformation.

INTRODUCTION

Rectangular hollow structural sections (HSS) are commonly used for braces in braced frames for seismic design. They have a relatively large radius of gyration, and their shape facilitates connection to gusset plates. Their inelastic performance depends on local slenderness, and AISC *Seismic Provisions for Structural Steel Buildings* (AISC, 2022), hereafter referred to as AISC 341, Table D1.1 provides local slenderness limits for highly ductile and moderately ductile braces.

For highly ductile members:

$$\frac{b}{t} < 0.65\sqrt{\frac{E}{R_y F_y}} \tag{1}$$

For moderately ductile members:

$$\frac{b}{t} < 0.76\sqrt{\frac{E}{R_y F_y}} \tag{2}$$

Design of special concentrically braced frames (SCBFs) requires sections that meet the highly ductile requirements, whereas design of ordinary concentrically braced frames (OCBFs) requires moderately ductile braces.

Rectangular HSS tubes have been manufactured under the ASTM A500/A500M (ASTM, 2021) standard. ASTM A500/A500M HSS sections are manufactured as Grades A, B, and C, which have minimum specified tensile yield stresses of 39, 46, and 50 ksi, respectively. However, most tubes are produced to meet the ASTM A500/A500M Grade C specification, and herein, reference to the ASTM A500/A500M standard is specifically to ASTM A500/A500M Grade C.

Dawn Lehman, Professor of Civil & Environmental Engineering, University of Washington, Seattle, Wash. Email: delehman@uw.edu (corresponding)

Joseph Khaldestad, Structural Engineer, Coughlin Porter Lundeen, Seattle, Wash. Email: jkaldestad@gmail.com

Will Bergendahl, Associate Project Consultant at Simpson Gumpertz & Heger, Wakefield, Mass. Email: wiberg@uw.edu

Andrew Sen, Assistant Professor of Civil Engineering, Marquette University, Milwaukee, Wis. Email: andrew.sen@marquette.edu

Jeffery Berman, Professor of Civil & Environmental Engineering, University of Washington, Seattle, Wash. Email: jwberman@uw.edu

Charles Roeder, Emeritus Professor of Civil & Environmental Engineering, University of Washington, Seattle, Wash. Email: croeder@uw.edu

Paper No. 2023-02

In 2013, a new standard for tubes was introduced, the ASTM A1085/A1085M (ASTM, 2022) specification. In comparison to the ASTM A500 specification, the ASTM A1085 specification requires a minimum Charpy V-notch (CVN) toughness, a limit on the maximum yield stress, and tighter tolerances of the thickness of tube wall, corner radii, and mass per unit brace length. For simplicity, ASTM A500/A500M Grade C sections will be referred to as A500C and ASTM A1085/A1085M sections will be referred to as A1085.

A1085 HSS are manufactured as a single grade comparable to A500C with a specified minimum tensile yield stress of 50 ksi. Both A500C and A1085 HSS sections are formed by a cold-forming process. As a result, the HSS sections experience significant strain hardening during manufacturing, and the measured yield stresses vary and are typically significantly larger than the specified minimum yield stress. Similar variation in the measured tensile yield stress is also noted.

This variation in stress is quite critical in capacity-based provisions for seismic design. It is accounted for in the ratio of expected yield stress to the specified minimum yield stress, R_y. AISC 341 defines R_y as 1.25, 1.4, and 1.3 for A1085, A500 Grade B, and A500 Grade C, respectively. The ratios of the expected tensile stress to the specified strength for these steel grades, R_t, are 1.15, 1.3, and 1.2, respectively. Note that the lower values of R_y and R_t for the A1085 tubes typically will result in smaller design demands on the connections, which has the potential to result in a more cost-effective lateral force-resisting system (LFRS). It is noted that A_g for A500C braces is based on reduced wall thickness, whereas for A1085 sections, it is based on the full thickness; this difference might result in similar tensile force capacities for both braces.

Relative to A500 braces, far fewer research studies have focused on the cyclic response of A1085 tubes used as braces. This research study was undertaken to investigate the cyclic response of A1085 braces using A500C braces as the reference member. The test matrix for the study was developed in collaboration with structural engineers, academics, and institutes [the Steel Tube Institute (STI) and the American Institute of Steel Construction (AISC)]. A total of 41 braces were tested to investigate the following parameters: (1) HSS producer, (2) width-to-thickness ratio, b/t, (3) global slenderness ratio, KL/r, and (4) deformation history. The measured behavior of braces was then compared and used to evaluate current design provisions with an eye toward advancing the governing provisions for both OCBF and SCBF with A1085 tubes used as braces.

BACKGROUND AND LITERATURE REVIEW

A substantial body of test data is available for the inelastic behavior A500 rectangular HSS braces under cyclic loading. Sen (2018) developed a database including 70 cyclic load tests completed between 1988 and 2018. These data were used to develop improved models for the envelope, full cyclic response, and a simple yet effective deformation-based limit to predict brace fracture. The data include tests documented in 23 different papers and reports (Johnson, 2005; Herman, 2007; Kotulka, 2007; Powell, 2010; Clark, 2009; Lumpkin, 2009; Fell et al., 2009; Yang and Mahin, 2005; Uriz and Mahin, 2008; Shaback and Brown, 2003; Han et al., 2007; Lee, 1988; Liu and Goel, 1987; Sloat, 2014; Johnson, 2014; Ballard, 2015; Sen, 2014; Swatosh, 2016; Ibarra, 2018; Richard, 2009). See Sen (2018) for additional details about these prior test series.

The local slenderness limit, b/t, varied between 10.5 and 31.4 in these tests. This is a very wide slenderness range covering rectangular HSS that are both within the limits of highly ductile and moderately ductile braces as well as sections that are well above these local slenderness limits.

SCBF design is based on the hypothesis that, on average, the brace will not fracture before story drifts of approximately 2.5% in both directions (a story-drift range of 5%). The highly ductile slenderness limit is based on the need to use this inelastic deformation capacity during the maximum considered seismic event. This brace deformation capacity and the well-known moderate lateral resistance and stiffness of braced frames after brace fracture ensure that SCBFs satisfy the collapse probability limits for the maximum considered earthquake in the United States (which has an approximate return period of 2500 years depending on the location).

The cyclic axial deformation of the brace is quite different from the cyclic story drift of a braced frame. Figure 1 is a geometric illustration of this effect. The figure shows that the brace tensile elongation or compressive shortening, δ, neglecting deformation of the connections is:

$$\delta = L_f - L_i \tag{3}$$

where L_i and L_f are the original undeformed brace length and the final deformed brace length, respectively. The horizontal story deflection, Δ, is small compared to the dimensions of the frame and the brace angle does not change significantly with increased story deflection, and so δ and Δ are related by:

$$\delta = \Delta \cos\theta \tag{4}$$

where θ is the brace angle measured from the horizontal axis.

Normally, story drift is quantified as a ratio or percentage of the story height, H_s, which can be expressed as $H = L_i \sin\theta$. The story-drift ratio, $\frac{\Delta}{H_s}$, and brace elongation are related using Equation 5.

$$\frac{\delta}{L_i} = \frac{\Delta\cos\theta}{L_i} = \frac{\Delta\cos\theta}{H_s/\sin\theta} = \frac{\Delta}{H_s}\cos\theta\sin\theta \qquad (5)$$

The brace angle is typically about 45°, and $\frac{\delta}{L_s}$ will be $\frac{\Delta}{2H_s}$ for that geometry. The brace angle may vary between 30° and 60°, and $\frac{\delta}{L_i}$ will be $\frac{\sqrt{3}\Delta}{4H_s}$ at these extremes. In all cases, the axial shortening, or elongation, ratio is less than half the story-drift ratio. This geometric relationship does not depend on the system configuration.

Prior testing by Lehman et al. (2008) found that axial elongation occurs when the brace is in tension for most braced frame configurations; the exception is that most chevron-configured SCBFs do not fully yield the brace in tension even when designed with large beams intended to remain elastic under reversed cyclic loading. In contrast, most of the axial shortening resulting from compressive demands on the brace is accommodated by the geometric shortening resulting from brace bucking, as illustrated in Figure 2. The images in the figure show the progression of buckling and fracture. Initial buckling is shown in Figure 2(a); the out-of-plane deformation resulting from compression displacement demands on the brace increases with increasing story-drift demands [Figure 2(b)]. At large story-drift demands, local cupping initiates at the midpoint of the brace, as shown in Figure 2(c), due to the large compressive deformation demands on brace. Cupping occurs regardless of the b/t ratio; however, the brace deformation corresponding to cupping depends on the b/t ratio—that is, the compressive deformation initiating cupping is larger for smaller b/t ratios. As story drift increases, the global buckling deformations become very large as shown in Figure 2(b), and the cupping deformation also becomes large as shown in Figures 2(c) and 2(d). As the brace is cycled, it buckles, straightens, and buckles again, resulting in large inelastic strains that accumulate in the cupped region. Eventually local striations occur at the corners of the brace as shown in Figure 2(d). With increased cycles and deformation demands, ductile tearing initiates at the corner striations [see Figure 2(e)], and tearing progresses across the wall of the tube. Full fracture of the cross section [see Figure 2(f)] occurs after increased deformation and after the tearing has developed to a sufficient length.

After cupping, yielding in both tension and compression primarily occurs in the central cupped region; this is expected because the stresses are much larger in the cupped region due to the combination of axial load and large P-δ moments. This concentration of strain is demonstrated by measurements in this region. It is important to note that cupping deformations result from demands in the plastic hinge region, which occurs in the center of the brace under compressive loading. Note that although this appears to be wall buckling, it does not cause stability issues of the brace or the CBF system.

Sections with small local slenderness ratios, b/t, spread the cupping deformation over a significant length, and the development of local striation, tearing, and fracture are delayed until large axial deformations of the brace occur. Sections with large b/t ratios have very concentrated cupping and striations; tearing and fracture develop more quickly.

As such, the b/t ratio is one of the most important design parameters, as recognized by AISC. However, these limits were established prior to the prevalent use of A500C or the introduction of A1085 HSS sections. As such, a

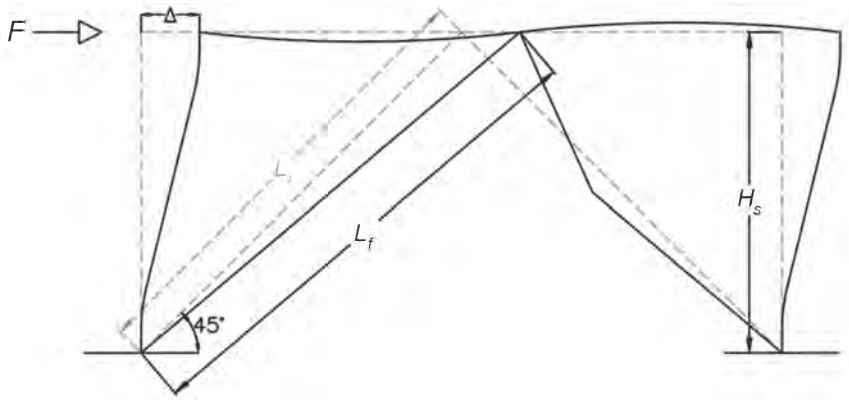

Fig. 1. Relationship between story drift and brace deformation, neglecting beam displacement.

(a) Initial brace buckling

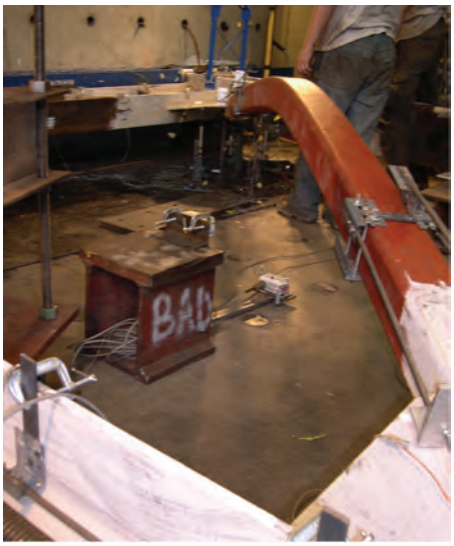

(b) Large out-of-plane deformation

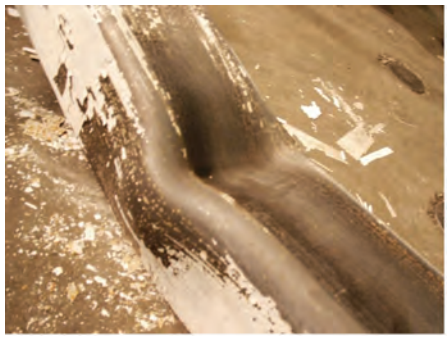

(c) Local cupping

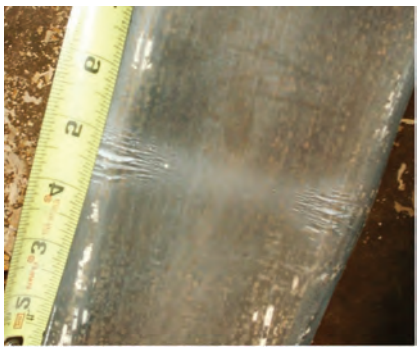

(d) Local striations at corners

(e) Ductile tearing initiates at corners and progresses across the tube wall

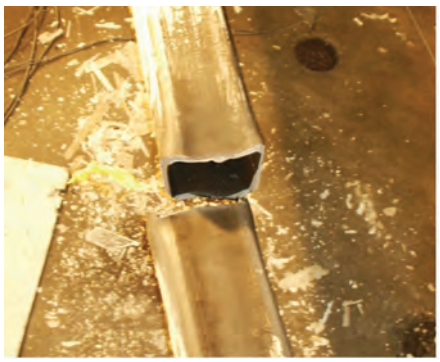

(f) Fracture after ductile tearing of most of cross section

Fig. 2. Buckling, tearing, and fracture of rectangular HSS braces.

comprehensive testing program was undertaken to evaluate current design limits for both steel grades. The following presents the experimental program and results. The final section evaluates the current limits and proposes modifications to meet the intended drift limits and extend, if possible, the number of sections available to meet the highly ductile and moderately ductile limits. In addition, the testing program evaluated the influence of the HSS producer, the global slenderness ratio (KL/r) and the displacement history.

EXPERIMENTAL PROGRAM

Forty-one square HSS specimens of various sizes and steel grades were provided by four different HSS producers (Table 1). The HSS sections were tested as braces in four series at the University of Washington's Structural Research Laboratory. The tube producers are identified as "Yellow," "Red," "Blue," and "White" to maintain producer anonymity. A naming convention is used to uniquely identify each specimen, in the order listed: (1) HSS shape, (2) steel specification (A1085 or A500C), and (3) producer (Y for Yellow, R for Red, B for Blue, and W for White).

Test Series

Table 1 shows four test series that were conducted to study the range of parameters that include ASTM specification, producer, length (and therefore KL/r), loading protocol, and HSS section (and therefore b/t). Test series I and II included a total of 32 tests that focused on the impact of producer, ASTM specification, and HSS section; all tests in these series had a brace length of 237.5 in. (6033 mm) and were tested under a standard increasing amplitude cyclic loading protocol as described later. Series I consisted of A500 and A1085 braces in the full range of section sizes, where the Yellow producer provided all A1085 braces and a mix of the four producers provided the A500 braces.

Test series III investigated solely A1085 HSS with a length of 237.5 in. (6033 mm) to study the impact of displacement histories; prior research suggests that the performance of HSS braces depends on the deformation history (Fell et al., 2009). Specifically, HSS8×8×⅜, HSS7×7×⅜, and HSS5×5×⅜ braces all from the producer marked Yellow were tested using three different loading protocols. These sections were selected because they provide a substantial range of local slenderness. As Table 1 shows, the loading protocol used for most tests was a symmetric protocol based on ATC-24 recommendations (ATC, 1992). Two alternative loading protocols identified as "chevron" or "near fault" were used in Test series III. The chevron protocol was compression dominant and intended to represent the behavior of a brace within an SCBF with a chevron configuration (Roeder et al., 2019). The near-fault loading protocol was tension dominant and intended to represent the pulse demands of a near-fault ground motion (Fell et al., 2009). Additional details on the loading protocols are provided in a subsequent section.

Prior research has shown that deformation capacity of HSS braces is also a function of the global-slenderness ratio, KL/r. To investigate this, Series IV tested A1085 HSS8×8×⅜, HSS7×7×⅜, and HSS5×5×⅜ braces that were all from the Yellow producer and were 184 in. (4660 mm) long such that their response could be compared with that of the braces that were 238 in. (6033 mm) long. Series IV specimens were subjected to the symmetric cyclic loading protocol with increasing displacements, but the magnitude of displacements was scaled to be proportional to the brace length and have the same normalized deformation history. These shorter specimens had "Short" appended to their designations.

Test Setup

The test setup was designed and built to impose cyclic compressive and tensile axial deformations on the brace specimens (HSS or other sections used as braces including BRBs). A drawing of the setup is shown in Figure 3(a); a photograph of the setup with a brace specimen in place is shown in Figure 3(b). The premise of the setup is to subject an HSS section attached to tapered plates at each end to the specified cyclic axial displacement history.

Two actuators with a combined capacity of 1,000 kips (4448kN) and +10 in. (25.4 cm) of stroke were used to impose the specified displacement demand under displacement control. The actuators were attached to a sliding beam on one side and a fixed reaction block on the other [Figure 3(a)].

The sliding load beam shown was an ASTM A992/A992M (ASTM, 2020) W33×201 section with ¾ in. side plates welded to the flanges on both sides to form a box section. The box section was filled with concrete to increase its stiffness. Low-friction polytetrafluoroethylene (PTFE) on greased and polished stainless-steel surfaces facilitated the sliding action with minimal lost resistance. Doubled shear plate connections were attached to the sliding beam and the central anchor block, and the gusset plate connections at each end of the brace fit between the shear plates and was shimmed as needed [Figure 3(c)]. The bolted connection was conservatively designed with 1 in. (25 mm) ASTM F3125/F3125M Gr. A490 (ASTM, 2019) bolts in double shear to minimize local slip and avoid local yielding. The gusset plates were designed by the balanced design procedure to develop the expected capacities of the specific brace section (Roeder et al., 2011).

Extensive instrumentation was attached to each specimen to measure the applied loads and deformations, as well as the distribution of strains and deformations, including out-of-plane (buckling) response. Axial load was measured

Table 1. HSS Sections, Brace Lengths, ASTM Specifications, Producers, and Loading Protocols Used in the Four Test Series Conducted

ATSM Specification		A500C				A1085						
Producer		Yellow	Red	Blue	White	Yellow				Red	Blue	White
Length (mm) (1 mm = 0.039 in.)		6033	6033	6033	6033	6033			4660	6033	6033	6033
Load Protocol		Symmetric Cyclic	Symmetric Cyclic	Symmetric Cyclic	Symmetric Cyclic	Symmetric Cyclic	Chevron	Near Fault	Symmetric Cyclic	Symmetric Cyclic	Symmetric Cyclic	Symmetric Cyclic
HSS Section	10×10×3/8				Series I	Series I						
	8×8×1/2				Series I	Series I				Series II	Series II	Series II
	8×8×3/8				Series I	Series I/III	Series III	Series III	Series IV	Series II	Series II	Series II
	7×7×1/2			Series I		Series I						
	7×7×3/8	Series I				Series I/III	Series III	Series III	Series IV			
	7×7×5/16	Series I				Series I						
	6×6×1/2		Series I			Series I						
	6×6×3/8		Series I			Series I				Series II	Series II	Series II
	6×6×5/16		Series I			Series I						
	5×5×3/8	Series I				Series I/III	Series III	Series III	Series IV	Series II	Series II	Series II

with load cells attached to the actuators. A series of string potentiometers measured axial and out-of-plane deformations of the brace. Strain gauges were attached at the quarter points of the brace to measure axial force and bending moments since the brace remains nearly elastic outside the central region and the regions attached to and near the gusset plates. A noncontact instrumentation system, the Optotrak system by Northern Digital Inc., was used to measure three-dimensional displacements at different locations along the brace. The Optotrak works by observing the movement of affixed LEDs with a special set of cameras and to within a millimeter. LEDs were concentrated within the gusset plate and the end of the brace—that is, the regions where significant inelastic action was expected. The measurements are used to determine local inelastic deformations and strain estimates and to provide a redundant check of key potentiometer readings. Duncan linear potentiometers are also placed at various location where small movements are possible to ensure functionality of the test and test setup. For this setup and instrumentation, the direction of buckling must be controlled in the experiment. To achieve this, each brace was welded to the gusset plate with a small, predetermined eccentricity.

MATERIAL PROPERTIES OF TEST SPECIMENS

Yield stress and tensile stress, the CVN toughness, and the steel thickness were measured for each supplied HSS steel section (including those of the name nominal dimension from different suppliers). All CVN tests were conducted

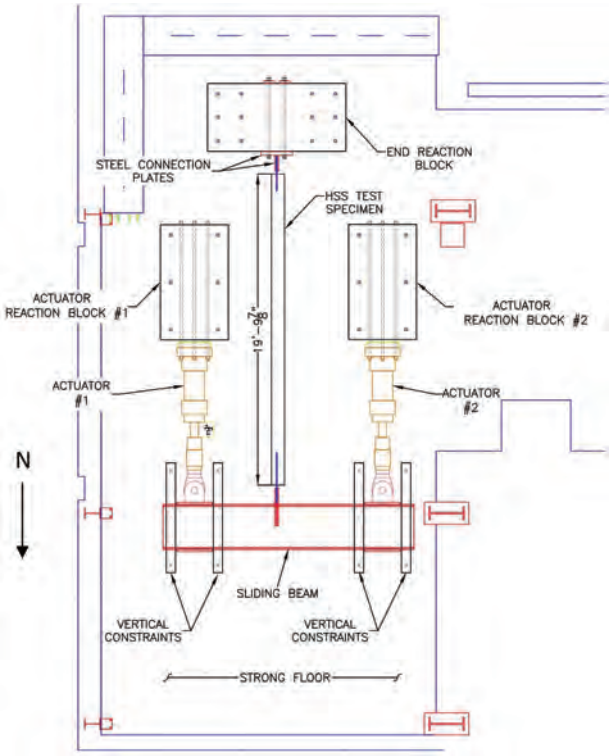

(a) Test setup

(b) Setup with a specimen in place

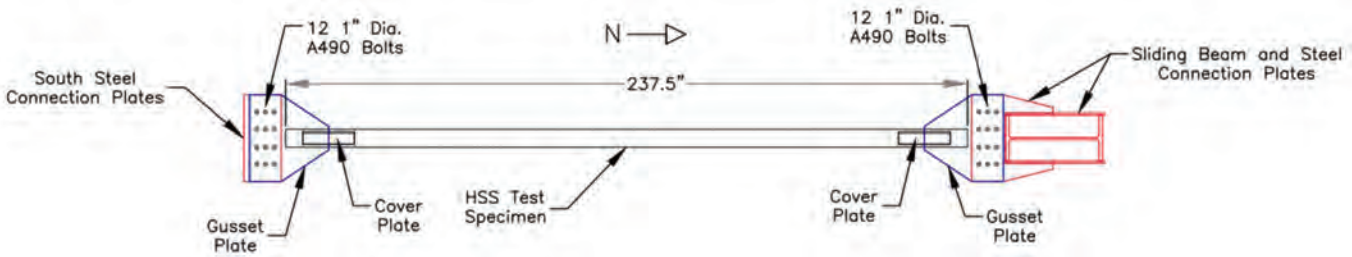

(c) Typical brace and bolted connection

Fig. 3. Test setup and brace specimen connection.

at room temperature. These properties were evaluated and compared to the ASTM standards. In addition, comparisons were made between A500 and A1085 tubes and between different producers of tubes. Table 2 summarizes the measured yield, tensile stress, and CVN toughness for each section produced by each producer. Tube wall thicknesses were measured; all of the thicknesses were within the tolerance of the respected ASTM standard.

As expected, the yield and tensile stress within each ASTM specification varied because of the cold-forming process, but the variation is within the tolerances of the respective ASTM standards. The following statistics were calculated using all of the HSS braces tested as part of this research program.

- The average measured yield stress was 63.95 ksi with a standard deviation of 4.49 ksi.
- The average R_y value was 1.28 with a standard deviation 0.09.
- The average tensile stress was 72.58 ksi with a standard deviation of 4.13 ksi.
- The average R_t value was 1.13 with a standard deviation of 0.066.

Most importantly, the difference between the A500C and A1085 tests was relatively small compared to the standard deviation of the overall data. This suggests that A500C HSS sections outperform expectations because they meet some or all of the requirements of the A1085 standard.

Three CVN tests were completed for each specimen and the reported toughness in Table 2 is the mean value of the three tests. The average CVN toughness for all specimens is 82 ft-lb. This number is somewhat low because energy larger than 120 ft-lb could not be measured, and specimens designated as 120+ exceeded this value.

The average CVN toughness for the A500C specimens was 62 ft-lb, which is approximately 75% of the average value of the A1085 specimens. It is noted that many of the specimens were subsize because the thickness of the steel was less than the size required for the standard CVN test. The subsize specimens are identified with the asterisk in the table, and their CVN toughness values were adjusted by the relative thickness of the specimen. This adjustment appears reasonable and is recommended in ASTM A370 (ASTM, 2023), but there is little documentation to verify that it is appropriate or correct. As a result, the toughness data must be viewed with caution. With this adjustment, two sections fell slightly below the 20 ft-lb limit for A1085 tubes.

Nearly all the toughness specimens were taken from the flat portion of the tube. However, specimens were taken from the corners of two of the thicker tubes. The values from the corners might be smaller than the actual value because of cold working. The CVN toughness of the six coupons taken for the corners were significantly tougher (nearly twice the value) than the CVN toughness taken from the flats of the same tube.

The thickness of all tubes was measured with a micrometer. The variation was well within the tolerances of the A500C and A1085 standards. In general, these combined data suggest that A1085 may consistently have slightly greater CVN toughness, but the overall the difference between the A1085 and A500C tubes is not significant.

TEST PROTOCOLS

The tests in this program were conducted by applying quasi-static cyclic axial displacements to one end of the brace while the other end of the brace was pinned. The two actuators were programmed to run under identical displacement control using MTS Multipurpose Testware software (MTS, 2011). In all cases, tests started with very small cycles at a displacement amplitude of 1$\frac{1}{16}$ in. to ensure that all equipment was functioning correctly. Then small but increasing amplitude cycles were applied until initial brace buckling and tensile yielding occurred.

One of three different displacement histories were applied to each test specimen. Figure 4(a) shows a displacement history based on the ATC-24 protocol (ATC, 1992). The history is symmetric, with displacement amplitudes based on a multiplier times the initial yield deformation until failure. The yield and buckling displacements were determined as a function of the brace length, as served as the basis for the displacement history applied to each brace. Figure 4(a) shows the deflections that were applied to the long (238 in.) specimens. The protocol for the short specimens is the same shape but scaled to the smaller deformations calculated for yield and buckling.

The chevron displacement protocol, shown in Figure 4(b), was based on previous research that showed that beam deflection in chevron configurations results in increased compressive deformations and decreased tensile deformations (Roeder et al., 2019). In this displacement protocol, the target compressive displacements increased in the same progression as the symmetric protocol. However, after initial yielding the tension cycles are limited to the deformation at which the brace axial tension force reaches the magnitude of the recorded brace buckling load.

The near-fault displacement protocol, shown in Figure 4(c), was developed as a modified version of a loading protocol used in previous research to represent nonsymmetric pulse-type demands for a braced frame subjected to near-fault ground motions (Fell et al., 2009). This protocol follows the shape of the compression-dominated near-field loading protocol used by Fell, but this protocol was inverted to be tension dominated and the magnitude of displacements was modified to reflect the buckling and yield deformations.

Table 2. Measured Properties for Test Specimens						
HSS Section	Yield Stress (ksi)	Yield Stress Ratio	Tensile Stress (ksi)	Tensile Stress Ratio	Percent Elongation (%)	CVN Energy (ft-lb)
5×5×⅜ A500 Y	65.38	1.31	71.9	1.16	30.79	17.0*
5×5×⅜ A1085 Y	66.04	1.32	74.6	1.15	32.83	25.0*
6×6×5/16 A500 R	57.37	1.15	72.8	1.17	34.65	81.6*
6×6×5/16 A1085 Y	62.07	1.24	71.9	1.11	34.11	46.0*
6×6×⅜ A500 R	61.19	1.22	76.4	1.23	35.36	56.5*
6×6×⅜ A1085 Y	66.81	1.34	72.6	1.12	31.86	25.0*
6×6×½ A500 R	62.84	1.26	67.1	1.08	33.48	120+
6×6×½ A1085 Y	67.85	1.36	72.0	1.11	34.88	27.8
7×7×5/16 A500 Y	62.71	1.25	70.0	1.13	31.16	23.6*
7×7×5/16 A1085 Y	57.70	1.15	64.1	0.99	33.12	27.8*
7×7×⅜ A500 Y	61.35	1.23	72.2	1.16	30.76	19.0*
7×7×⅜ A1085 Y	61.89	1.24	70.1	1.08	31.32	23.0*
7×7×½ A500 B	57.82	1.16	69.1	1.11	29.6	42.0
7×7×½ A1085 Y	64.38	1.29	71.7	1.10	32.7	28.7
8×8×⅜ A500 W	66.19	1.32	76.5	1.23	34.44	87.1*
8×8×⅜ A1085 Y	60.37	1.21	72.1	1.11	34.2	11.3*
8×8×½ A500 W	65.47	1.31	72.0	1.16	34.27	67.3
8×8×½ A1085 Y	64.42	1.29	75.4	1.16	32.23	40.3
10×10×⅜ A500 W	59.02	1.18	69.5	1.12	34.2	120+*
10×10×⅜ A1085 Y	58.34	1.17	73.8	1.14	34.94	27.5*
5×5×⅜ A1085 R	68.82	1.38	77.52	1.19	34.92	30.9*
5×5×⅜ A1085 W	69.53	1.39	75.03	1.15	38.06	102.4*
5×5×⅜ A1085 B	78.15	1.56	87.62	1.35	27.90	40.9*
6×6×⅜ A1085 R	60.41	1.21	74.29	1.14	33.26	54.0*
6×6×⅜ A1085 W	67.66	1.35	73.22	1.13	37.53	110.2*
6×6×⅜ A1085 B	69.05	1.38	73.59	1.13	34.75	120+*
8×8×⅜ A1085 R	61.20	1.22	75.42	1.16	32.44	77.8*
8×8×⅜ A1085 W	63.19	1.26	70.67	1.09	40.55	94.0*
8×8×⅜ A1085 B	68.24	1.36	71.63	1.10	37.18	120+*
8×8×½ A1085 R	58.54	1.17	64.27	0.99	34.43	120+
8×8×½ A1085 W	58.54	1.17	64.27	0.99	42.02	120+
8×8×½ A1085 B	66.36	1.33	70.51	1.08	39.56	120+

* Indicates tests that were conducted with a subsize Charpy test specimen and with toughness values adjusted by the ratio of the thickness of a standard Charpy specimen to the subsize specimen.

+ Indicates specimen that reached the maximum energy that could be measured.

EXPERIMENTAL RESULTS

For each specimen, the load-displacement response was measured. In addition, the progressive yielding and damage to the specimens was observed during the tests and noted. To determine the damage states and their corresponding deformation demand, clear damage criteria were established as shown in Table 3. These damage states were developed in prior research (Roeder et al., 2012) and relate to potential repair costs and the sequence of behaviors leading to brace fracture as summarized earlier and described in prior research (Lehman et al., 2008). For the brace alone,

the important damage states (DS) on the degree of buckling (DS B1- B3) as well as brace tearing (DS B3-T) and fracture (DS B4) result from cyclic loading and cupping of the tube walls in the plastic hinge region.

Forty-one tests were completed. Table 4 summarizes the results, where P_{Tmax} is the brace maximum tension force, P_{Cmax} is the maximum brace compression force, P_y is the brace yield force calculated with measured material properties, P_{cr} is the brace buckling force calculated with measured material properties, $\Delta_{T,max}$ is the maximum brace elongation in tension prior to brace fracture, $\Delta_{C,max}$ is the maximum brace compressive deformation, Δ_{Acc} is the cumulative brace deformation, $\sum E_{Diss}$ is the cumulative energy dissipation, $A_{g,m}$ is the measured cross-sectional area, and $F_{y,m}$ is the measured yield strength. The last column in Table 4 is the accumulated energy dissipated prior to brace fracture normalized to the tensile force predicted from the measured properties of the tube. This measure is an approximate and relative comparison of the stable cyclic, nonlinear response achieved by each specimen.

Four tests of series I and II are presented in greater detail—specifically, specimen 5×5×⅜ A1085 Y, specimen 6×6×⅜ A1085 Y, specimen 7×7×⅜ A1085 Y, and specimen 8×8×⅜ A1085 Y. These specimens were selected because they have the following properties in common: (1) A1085 HSS sections, (2) same nominal thickness, and (3) same producer. This permits direct comparison based on varied design parameters—that is, the global and local slenderness ratios. Specifically, the four tests have b/t ratios of 10.3, 13, 14.2, and 18.3, which represent members well below the high ductility slenderness limit, members approaching the high ductility limit, members exceeding the high ductility limit and approaching the moderate ductility limit, and members clearly exceeding the moderate ductility limit. Results for series III and IV are focused on a single parameter and are discussed separately.

Impact of Width-to-Thickness Ratio

Figure 5 shows the axial force/deformation plots for the highlighted specimens (highlighted specimens are shaded in Table 4), and Figure 6 provides photos of these specimens at the maximum compressive deformation prior to initiation of tearing. The following summarizes the observed and measured response of each of the highlighted specimens.

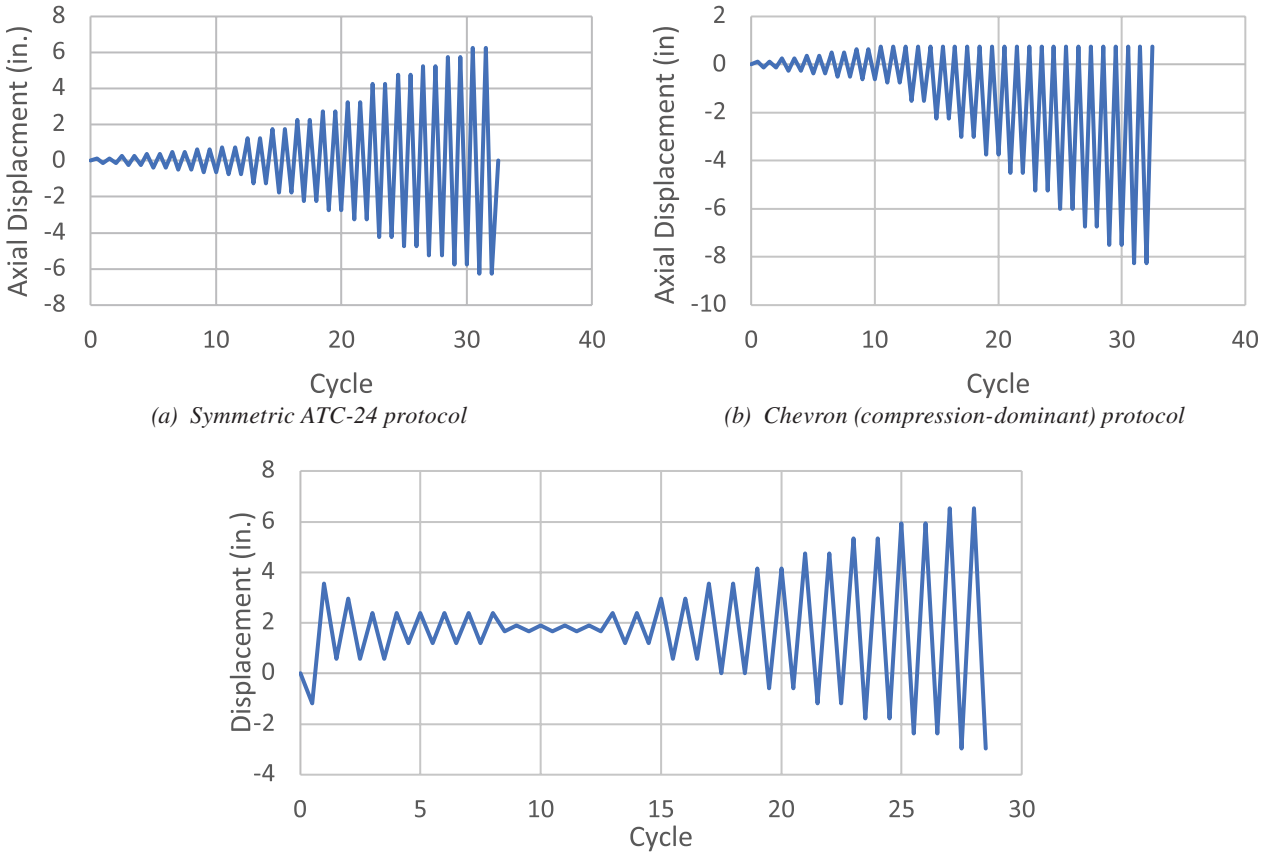

(a) Symmetric ATC-24 protocol

(b) Chevron (compression-dominant) protocol

(c) Near-fault (tension-dominant) protocol

Fig. 4. Test protocols.

Table 3. Brace Damage States for Performance Assessment			
Sketch/Photograph of Damage State	**Abbreviation**	**Damage State**	**Description**
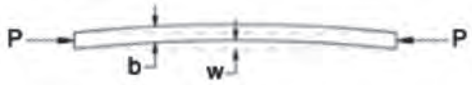	B1	Initial global buckling	Brace midspan deflection visible but less than the brace depth
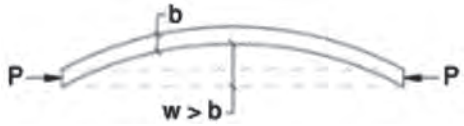	B2	Moderate global buckling	Brace midspan deflection exceeds the brace depth
	B3 – C	Local cupping deformations	Visible local cupping deformation near midpoint of the brace
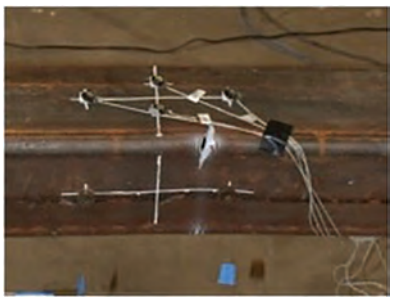	B3 – T	Striations and tearing	Striation lines begin in the cupped (plastic hinge) region of brace
	B4	Brace fracture	Brace fractures through the entire cross section

Table 4. Summary of Test Specimen Performance with Highlighted Specimens Indicated							
HSS Section	$P_{T,max}$ (kips) ($P_{T,max}/P_y$)	$P_{C,max}$ (kips) ($P_{C,max}/P_{Cr}$)	$\Delta_{T,max}$ (in.) (Drift %)	$\Delta_{C,max}$ (in.) (Drift %)	Δ_{range} (in.) (Drift %)	Δ_{Acc} (in.) (Drift %)	$\frac{\sum E_{Diss}}{A_{g,m}F_{y,m}}$
5×5×⅜ A500 Y	432.50 (1.04)	−95.30 (0.99)	5.13 (4.28)	4.89 (4.07)	10.02 (8.35)	119.54 (99.65)	20.57
5×5×⅜ A1085 Y	443.60 (1.02)	−98.38 (0.97)	5.25 (4.38)	5.50 (4.59)	10.75 (8.96)	132.02 (110.05)	21.74
6×6×5⁄16 A500 R	409.70 (1.06)	−125.75 (0.82)	3.06 (2.55)	3.26 (2.71)	6.31 (5.26)	52.34 (43.63)	13.29
6×6×5⁄16 A1085 Y	456.40 (1.07)	139.80 (0.87)	3.13 (2.61)	3.12 (2.60)	6.25 (5.21)	51.33 (42.79)	12.57
6×6×⅜ A500 R	511.00 (1.05)	−168.70 (0.96)	3.74 (3.12)	3.72 (3.10)	7.46 (6.22)	65.80 (54.85)	16.45
6×6×⅜ A1085 Y	547.90 (1.01)	−180.00 (0.97)	3.52 (2.93)	3.52 (2.93)	7.04 (5.87)	56.61 (47.19)	13.63
6×6×½ A500 R	646.20 (1.02)	−218.70 (1.01)	4.45 (3.71)	4.06 (3.39)	8.51 (7.10)	80.64 (67.22)	17.25
6×6×½ A1085 Y	727.20 (1.06)	−218.60 (0.97)	4.67 (3.89)	5.12 (4.27)	9.79 (8.16)	97.41 (81.21)	22.36
7×7×5⁄16 A500 Y	496.60 (1.05)	−209.80 (0.88)	1.73 (1.44)	1.83 (1.53)	3.56 (2.97)	20.29 (16.91)	5.82
7×7×5⁄16 A1085 Y	478.10 (1.05)	−201.50 (0.80)	1.99 (1.66)	2.31 (1.92)	4.29 (3.58)	27.94 (23.30)	8.01
7×7×⅜ A500 Y	570.90 (1.06)	−231.80 (0.83)	2.51 (2.09)	2.79 (2.33)	5.30 (4.42)	35.26 (29.40)	10.49
7×7×⅜ A1085 Y	615.90 (1.07)	−254.90 (0.87)	2.36 (1.97)	2.85 (2.38)	5.21 (4.35)	37.42 (31.20)	9.76
7×7×½ A500 B	710.40 (1.06)	−278.80 (0.80)	3.59 (2.99)	4.16 (3.47)	7.75 (6.46)	70.86 (59.08)	19.31
7×7×½ A1085 Y	805.10 (1.04)	−305.70 (0.84)	3.48 (2.90)	4.41 (3.68)	7.89 (6.58)	70.13 (58.46)	18.21
8×8×⅜ A500 W	702.70 (1.02)	−359.98 (0.93)	1.24 (1.04)	1.90 (1.58)	3.14 (2.62)	18.10 (15.09)	4.97
8×8×⅜ A1085 Y	672.60 (1.02)	−328.80 (0.81)	2.18 (1.82)	2.18 (1.82)	4.36 (3.63)	27.43 (22.87)	9.18
8×8×½ A500 W	905.97 (1.03)	−434.72 (0.88)	2.71 (2.26)	2.80 (2.34)	5.51 (4.60)	38.25 (31.89)	12.66
8×8×½ A1085 Y	921.90 (1.02)	−418.20 (0.82)	2.96 (2.46)	3.32 (2.77)	6.28 (5.23)	44.07 (36.74)	13.29
10×10×⅜ A500 W	785.40 (1.01)	−480.10 (0.79)	2.10 (1.75)	2.48 (2.07)	4.58 (3.81)	25.71 (21.43)	5.96
10×10×⅜ A1085 Y	812.80 (1.01)	−507.60 (0.81)	1.60 (1.33)	1.84 (1.53)	3.44 (2.87)	15.66 (13.05)	4.67
5×5×⅜ A1085 R	456.59 (1.01)	−114.23 (1.13)	4.91 (4.09)	5.14 (4.29)	10.05 (8.38)	120.09 (100.11)	18.79

Table 4. Summary of Test Specimen Performance with Highlighted Specimens Indicated (continued)							
HSS Section	$P_{T,max}$ (kips) ($P_{T,max}/P_y$)	$P_{C,max}$ (kips) ($P_{C,max}/P_{Cr}$)	$\Delta_{T,max}$ (in.) (Drift %)	$\Delta_{C,max}$ (in.) (Drift %)	Δ_{range} (in.) (Drift %)	Δ_{Acc} (in.) (Drift %)	$\frac{\sum E_{Diss}}{A_{g,m}F_{y,m}}$
5×5×⅜ A1085 W	468.27 (1.03)	–110.19 (1.09)	4.72 (3.93)	5.27 (4.39)	9.99 (8.32)	109.31 (91.13)	17.64
5×5×⅜ A1085 B	538.20 (1.03)	–126.44 (1.25)	3.93 (3.28)	5.07 (4.23)	9.00 (7.51)	98.28 (81.93)	15.50
6×6×⅜ A1085 R	521.04 (1.08)	–178.82 (0.97)	3.96 (3.30)	4.14 (3.45)	8.09 (6.75)	73.05 (60.89)	17.30
6×6×⅜ A1085 W	549.55 (1.00)	–185.84 (1.00)	3.66 (3.05)	4.04 (3.37)	7.70 (6.42)	65.74 (54.81)	14.62
6×6×⅜ A1085 B	581.67 (1.03)	–177.88 (0.96)	2.97 (2.48)	3.26 (2.72)	6.23 (5.19)	50.27 (41.91)	10.74
8×8×⅜ A1085 R	660.41 (0.99)	–323.69 (0.80)	2.68 (2.23)	1.77 (1.48)	4.45 (3.71)	25.76 (21.48)	8.17
8×8×⅜ A1085 W	711.95 (1.02)	–361.03 (0.89)	2.31 (1.93)	2.28 (1.90)	4.59 (3.83)	26.46 (22.06)	8.30
8×8×⅜ A1085 B	763.00 (1.01)	–363.94 (0.90)	1.74 (1.45)	2.55 (2.12)	4.29 (3.57)	24.55 (20.47)	6.71
8×8×½ A1085 R	819.18 (1.04)	–425.29 (0.83)	3.31 (2.76)	2.95 (2.46)	6.26 (5.21)	47.25 (39.39)	11.77
8×8×½ A1085 W	964.72 (1.01)	–446.26 (0.87)	2.83 (2.36)	3.28 (2.73)	6.10 (5.09)	45.42 (37.86)	13.10
8×8×½ A1085 B	938.58 (0.98)	–478.57 (0.94)	3.03 (2.53)	3.05 (2.55)	6.08 (5.07)	39.67 (33.07)	10.93
5×5×⅜ A1085 Y Chevron	409.06 (0.94)	–93.31 (0.92)	3.64 (3.03)	7.82 (6.52)	11.46 (9.55)	229.47 (191.30)	23.12
5×5×⅜ A1085 Y Near Fault	464.24 (1.07)	–95.36 (0.94)	7.88 (6.57)	4.34 (3.62)	12.22 (10.19)	152.72 (127.32)	24.92
7×7×⅜ A1085 Y Chevron	258.35 (0.45)	–257.40 (0.88)	1.16 (0.97)	4.24 (3.54)	5.41 (4.51)	34.04 (28.37)	5.81
7×7×⅜ A1085 Y Near Fault	670.92 (1.16)	–255.17 (0.87)	4.08 (3.40)	1.50 (1.25)	5.57 (4.65)	42.55 (35.47)	12.78
8×8×⅜ A1085 Y Chevron	332.92 (0.50)	–320.72 (0.79)	1.10 (0.92)	3.58 (2.98)	4.68 (3.90)	25.74 (21.46)	5.32
8×8×⅜ A1085 Y Near Fault	716.32 (1.08)	–308.41 (0.76)	3.95 (3.29)	1.03 (0.86)	4.98 (4.15)	32.37 (26.98)	11.43
5×5×⅜ A1085 Y Short	438.58 (1.01)	–140.80 (0.83)	3.64 (3.93)	3.45 (3.73)	7.10 (7.66)	76.29 (63.60)	15.94
7×7×⅜ A1085 Y Short	617.53 (1.07)	–327.91 (0.84)	1.56 (1.68)	1.74 (1.88)	3.30 (3.57)	19.88 (16.57)	7.10
8×8×⅜ A1085 Y Short	666.42 (1.01)	–393.60 (0.78)	1.61 (1.74)	1.65 (1.78)	3.27 (3.52)	19.70 (16.42)	6.98

Specimen 5×5×⅜ A1085 Y buckled at a compressive load of 98.4 kips, which is the peak compressive force, at a compressive axial displacement of 0.19 in. The B2 damage state was noted during the 1.25 in. compressive-displacement cycles. The specimen reached a maximum tensile force of 443.6 kips at an axial displacement of 1.83 in., and the tensile forces slowly decreased during later cycles. Local cupping at the center of the specimen was observed at a compressive axial displacement of just over 5 in. Tearing at the center of the specimen was initially observed during the second cycle of the 5.75 in. target displacement, and the tearing quickly spread across the east, top, and bottom walls of the section. The brace fractured in tension during this same cycle, at an axial displacement of 5.25 in.

Specimen 6×6×⅜ A1085 Y buckled at a compressive force of 180 kips at a displacement of 0.15 in. The B2 damage state was observed during the 1.75 in. target displacement cycles. This specimen reached a peak tensile force of 547.9 kips at an axial displacement of 1.76 in., and the peak tensile forces decreased slightly in subsequent cycles at larger displacements. Local cupping deformations were initially observed at an axial displacement of about 3.06 in. Striations and tearing developed at the center of the brace during the second cycle of this 3.75 in. target displacement, but the brace did not fracture at the peak tensile displacement. Only the west wall of the specimen remained intact, and when the loading was reversed and the brace was put into compression, it fractured at a displacement of 0.55 in. prior to reaching its neutral position.

Specimen 7×7×⅜ A1085 Y buckled at a compressive force of 254.9 kips at a displacement of 0.27 in. Local cupping was observed at a compressive displacement of 2.27 in.

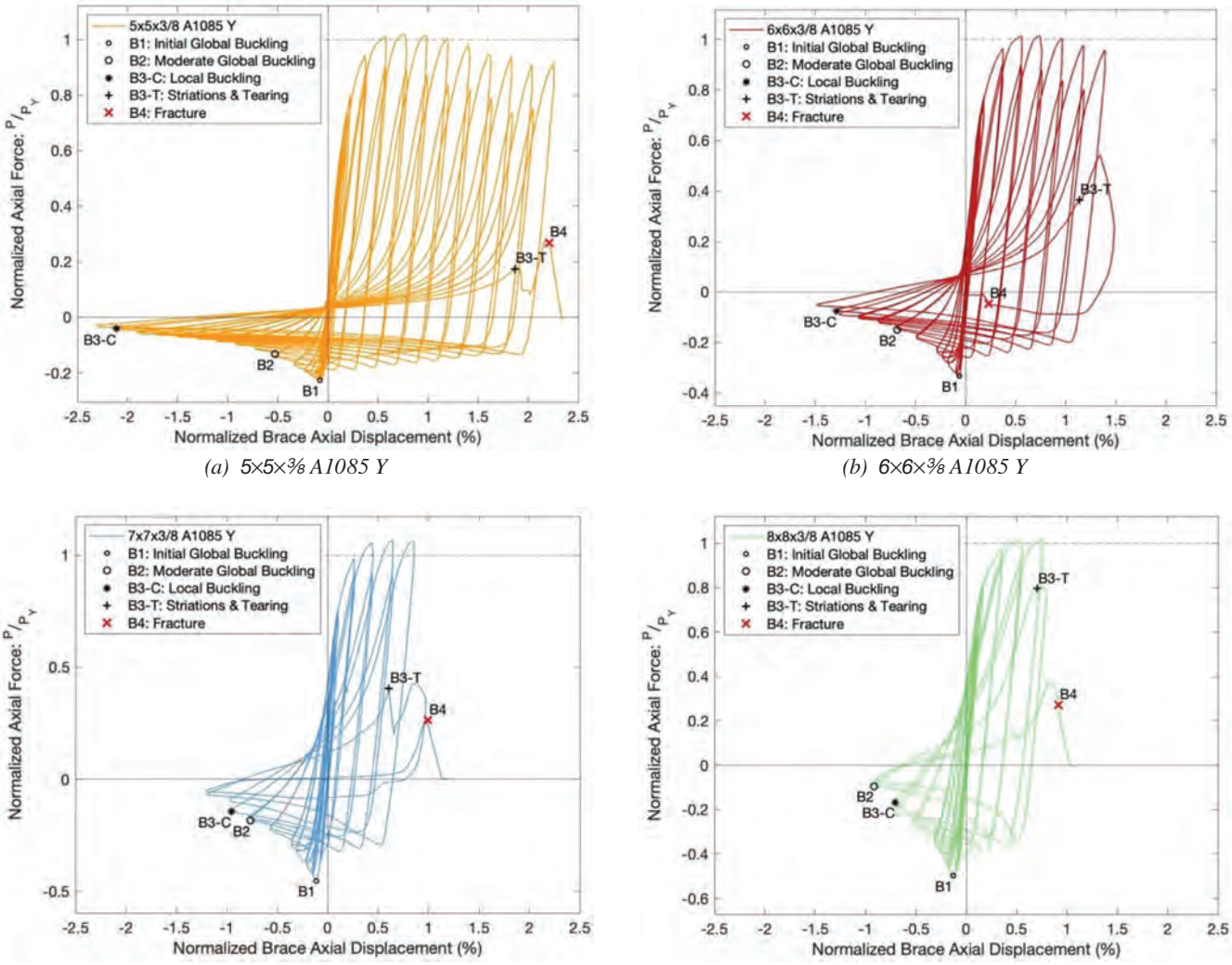

(a) 5×5×⅜ A1085 Y

(b) 6×6×⅜ A1085 Y

(c) 7×7×⅜ A1085 Y

(d) 8×8×⅜ A1085 Y

Fig. 5. Axial force/deflection curve for four highlighted braces.

A maximum tensile force of 615.9 kips was reached at an axial displacement of 1.53 in. The brace eventually fractured during the tension portion of the first 3.25 in. target displacement cycle at an axial displacement of 2.31 in.

Specimen 8×8×⅜ A1085 Y buckled at a compressive force of 328.8 kips, which was the maximum compressive force, and an axial displacement of 0.31 in. The maximum tensile force achieved was 672.6 kips at an axial displacement of 1.2 in. Local cupping was initially observed at an axial displacement of 1.68 in. As the brace was cycled into tension during the second 2.25 in. target-displacement cycle, striations and tearing developed at the center of the brace. The tearing spread across the east and bottom walls of the tube, leaving the west wall and much of the top wall intact. Complete fracture occurred at an axial displacement of about 2.18 in.

Figure 6 shows the damage state of cupping just prior to brace tearing and fracture as well as the deformation at which this state occurred. Together, Figures 5 and 6 show that the severe cupping state B3-C occurred at sequentially smaller compressive deformations as the b/t ratio increased. (Recall that the HSS sections with larger widths have increased b/t ratios because the thickness of the four specimens is the same.) Further, Figure 6 shows that cupping deformation are concentrated over a shorter length as the b/t ratio increased.

The length of cupping can be assessed relative to the specimen depth. The HSS5×5×⅜ and the HSS6×6×⅜ sections meet the high ductility demand slenderness limit, and the cupping is clearly distributed over a longer (approximate 6 in.) length. The HSS8×8×⅜ section has a higher b/t ratio, which exceeds both the highly and moderately

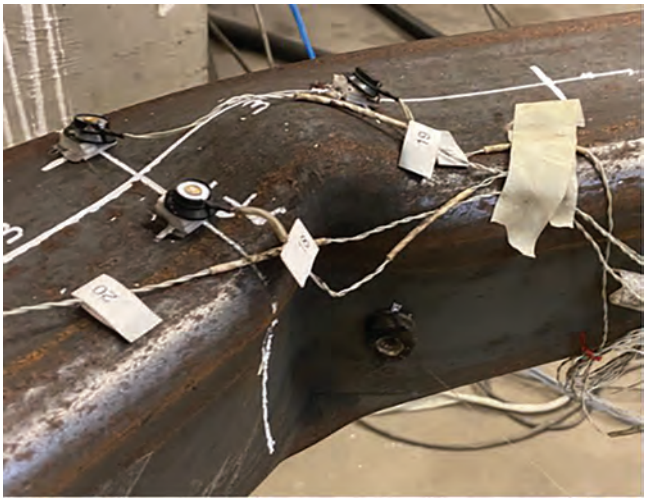

(a) 5×5×⅜ A1085 Y

(b) 6×6×⅜ A1085 Y

(c) 7×7×⅜ A1085 Y

(d) 8×8×⅜ A1085 Y

Fig. 6. Severe cupping (state B3-C) just prior to tearing for the four highlighted specimens.

ductile slenderness limits; its cupping is distributed over a length that is approximately one-third of the highly ductile sections—that is, approximately 2 in. The largest inelastic strains develop in the cupped region, but the strain is distributed over a shorter length with larger b/t ratios, which leads to earlier fracture.

Impact of Loading History

The series III tests evaluated three different loading protocols; specifically, it compares chevron (compression-dominated) and near-fault (tension-dominated) test protocols with the conventional symmetric ATC-24 protocol used for the rest of the tests. Figure 7 shows the force-deflection behavior of A1085 5×5×⅜ Y braces tested under the compression-dominant, chevron, and tension-dominant, or near-fault, protocol. Figures 7(a) and 7(b) are compared to Figure 5(a) to evaluate the impact of the three different load histories on the response of the specimens. The chevron test shown in Figure 7(a) ran out of actuator stroke in compression well before specimen failure, and large tensile deformations were then applied to induce brace fracture. The near-fault protocol was completed to failure. The chevron and near-fault hysteretic behaviors are more one-sided than the ATC-24 protocol test. However, beyond this obvious difference, the behavior is very similar. Note the ATC-24 test achieved +2.25% axial deformation prior to brace fracture, and this resulted in 4.5% axial deformation range. The chevron test achieved –3.25% and 1.5% for a 4.75% range. The near fault achieved –1.5% and +3.25% for a 4.75% range. The maximum compressive forces were 98.4 kips, 93.3 kips, and 95.4 kips, respectively. The maximum tensile forces were 432.4 kips, 409.1 kips, and 464.2 kips.

There is very little difference in the post-yield (i.e., inelastic) behavior for the three displacement histories used in this study. The resistance of the specimens subjected to the near-fault protocol is slightly larger than the same specimen subjected to either of the other two histories. This difference is most likely due to the greater strain hardening with the near-fault protocol. The deformation range is similar in all cases but slightly smaller for the symmetric ATC-24 load history. This suggests that the symmetric ATC-24 test protocol is the more damaging than the other two for a given drift range.

Similar tests were performed with HSS7×7×⅜ and HSS8×8×⅜ braces with the same general results. This quite clearly shows that focusing on the total deformation range rather than the maximum brace deformation is a rational way of evaluation brace deformation capacity. This has been noted in other prior studies (Lehman et al., 2008).

Series IV consisted of three tests of these same three brace sizes with shorter brace lengths to clearly evaluate the impact of Kl/r on brace response. Figure 8 shows the force-deformation behaviors of the three shorter brace lengths and these figures can be compared to longer brace lengths in Figures 5(a), 5(b), and 5(c).

These specimens were subjected to that ATC-24 deformation protocol, which was adapted to the shorter brace length by adjusting the yield displacement. The 5×5×⅜ A1085 Y Short test specimen developed a maximum compressive force of 140.8 kips and a maximum tensile force of 438.6 kips. This buckling force is larger than the 98.4 kips achieved with 5×5×⅜ A1085 Y because of the smaller KL/r value, but the tensile resistance was similar at 443.6 kips. The axial deformations varied from –2% to 1.6% for an axial deformation range of 3.6% compared to 4.5% achieved by the longer specimen.

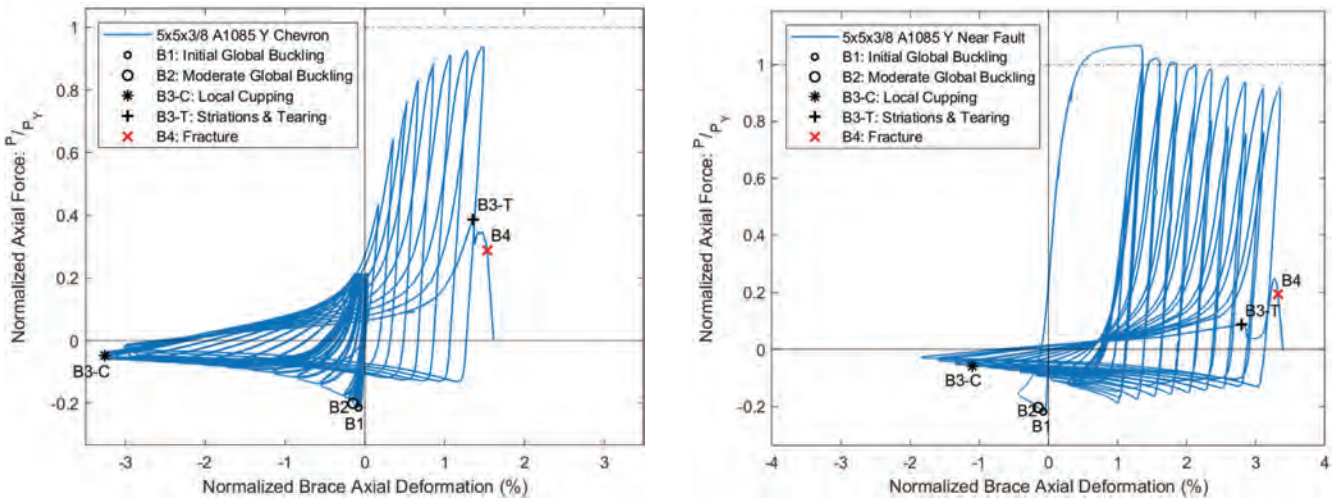

(a) Chevron test protocol *(b) Near-fault test protocol*

Fig. 7. Near-fault and chevron test protocol with A1085 5×5×⅜ braces.

The 7×7×3/8 A1085 Y Short test specimen developed a compressive force of 327.9 kips and tensile force of 617.5 kips. The longer specimen, 7×7×3/8 A1085 Y, developed a 254.9 kip compressive force due to its larger KL/r value and a similar tensile force of 615.9 kips. The shorter specimen developed an axial deformation range of approximately 1.75%, while the longer specimen achieved approximately 2.75%.

Specimen 8×8×3/8 A1085 Y Short developed a compressive force of 393.6 kips and a maximum tensile force of 666.4 kips. The companion long specimen, 8×8×3/8 A1085 Y, developed a 328.8 kip compressive force due to its larger KL/r value and a similar tensile resistance of 672.6 kips. The axial deformation range for the short and long specimen was similar at approximately 1.5%.

These comparisons clearly show that the normalized inelastic deformation capacity tends to be smaller for shorter specimens, and examination of the photos of the cupped regions suggests that the probable cause is the plastic hinging and cupping of the buckled braced that is concentrated over a shorter length with shorter braces. This result is logical. Cupping is caused by plastic hinging under compressive loading. The length of the cupped region occurs over a shorter length for shorter braces due to the local deformations in the shorter plastic-hinge region.

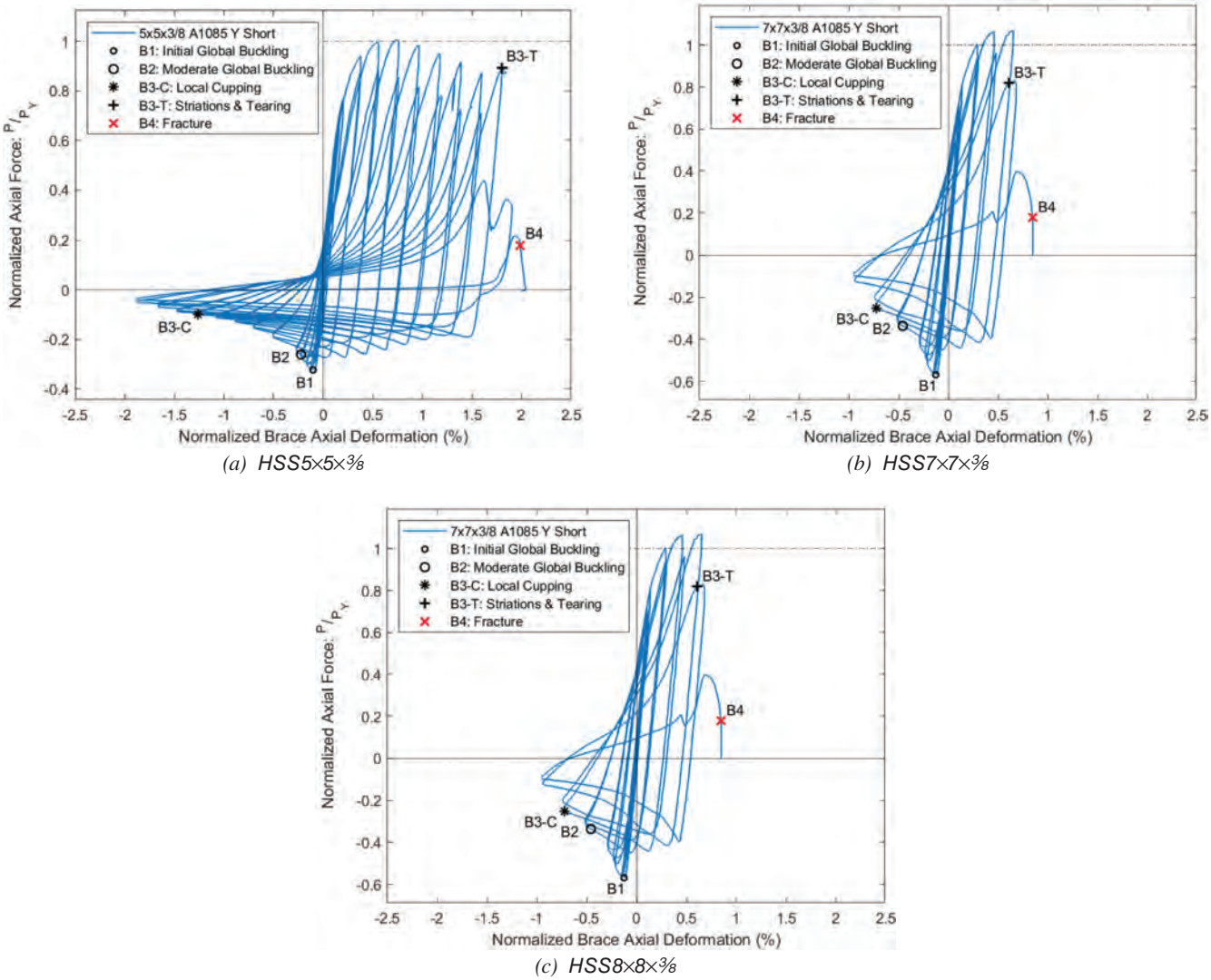

(a) HSS5×5×3/8

(b) HSS7×7×3/8

(c) HSS8×8×3/8

Fig. 8. Effect of shorter brace length.

EFFECT OF LOCAL SLENDERNESS OF BRACED FRAME DESIGN

Inelastic axial deformation of HSS braces is the primary yield mechanism in concentrically braced frames (CBFs). Through yielding in tension, buckling in compression, and post-buckling deformation, the brace is the main source of energy dissipation and inelastic deformation needed to resist demands from major earthquakes. As the brace experiences large axial deformations due to story drift, the midspan of the buckled brace forms a plastic hinge, and the brace develops local deformations or local cupping, which will ultimately lead to brace fracture. The ability to withstand large inelastic deformations without brace fracture is the basis of good seismic performance. The local compactness ratio, b/t, and global slenderness ratio, KL/r, have a significant impact on the initiation of local cupping and fracture of HSS braces. An HSS brace that has smaller local slenderness, b/t, and a larger global slenderness, KL/r, normally develops larger inelastic deformations prior to local cupping and fracture and that cupping is spread over a longer length.

Deformation demands for CBFs are usually stated in terms of story drift. As a result, the axial deformations for each test were converted to story drifts in Table 4, assuming that the total story drift is a result of the brace; this is a conservative approximation as additional deformation results from gusset plate yielding and frame action. As noted with prior discussion and shown in Figure 1, story drift and drift range are conservatively estimated as two times the normalized axial deformations.

For SCBFs, story-drift demand is estimated as +2.5% in AISC 341-22 (AISC, 2022). There is no specific limit postulated for OCBFs, but it is expected to be less than that for SCBFs since their response modification factor, R, is smaller and the resulting seismic design force is significantly larger. In addition, OCBFs are not permitted in high-seismic regions, and, as such, have received less attention in the literature, suggesting this system should be considered in future studies.

In a past study, Hsiao performed research that provides some insight on this expected demand (Hsiao et al., 2013). In that study, CBFs were designed to different resistance levels with R values between 3 and 8 for the seismic hazard in Seattle, Washington. The buildings were designed to seismic design standards for 3-, 8-, and 20-story height with the floor plans used for the SAC Steel Project (FEMA, 2000). In the study by Hsaio et al., SCBF requirements (geometric limits on the framing members as well as the brace, connection design) were used for all of the simulation models. Validated nonlinear models were developed to simulate the inelastic deformation of the brace, the frame and the connections including brace yielding, buckling, post-buckling, fracture, and post-fracture performance. The models were verified and calibrated to measured behavior from experimental research. Then 20 earthquake acceleration records were selected and scaled to the to the seismic hazard for the building location for a 2% probability of exceedance in 50 years and 10% probability of exceedance in 50 years seismic events. Nonlinear response history analyses were performed, and statistical evaluation of the response and expected damage were made. Figure 9 is a plot of the average maximum story drift for each level of the structure for the various building heights, design criteria, and seismic hazard. The plot clearly shows that the drift demand depends on the seismic event, the value of R, and the number of stories. Because the latter is not accounted for the building code, it will not be discussed here.

SCBFs currently have an R value of 6, and Figure 9 shows a 2.5% story-drift limit is about right for the three-story SCBFs. For taller buildings the average maximum story drift (MSD in Figure 9) is less than 1% for $R = 6$ and the 2% probability of exceedance in 50-year event.

OCBFs are designed for a response modification factor of 3.25 (simplified to 3 here), and Figure 9 would suggest that this requires a deformation capacity of about 1.0%

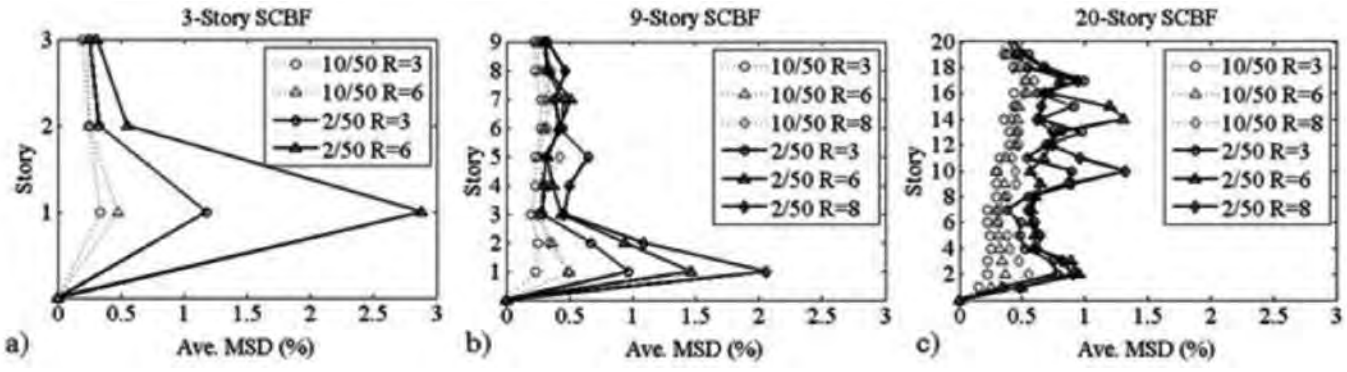

Fig. 9. Average maximum seismic response of OCBF and SCBFs (Hsiao et al., 2013b).

story drift prior to brace fracture for all three buildings. The experimental data discussed earlier show that story-drift range is a more accurate measure of the deformation capacity of an HSS brace because it is not influenced greatly by test protocol or seismic excitation. Thus, a 2.5% story-drift target in one direction for SCBFs is expressed as a story-drift range of 5%. The prior analysis does not provide data on drift range, but the maximum story drift of 2.5% implies a drift range less than 5%. These data are for a single location and should not be considered conclusive, but the data suggest that a maximum story-drift demand of approximately 2.5% is appropriate for SCBFs and a demand of 1.0% is appropriate for OCBFs.

Figure 10 shows the relationship between local compactness and story-drift range from the test data of this experimental research study. The measured yield stress is used to plot the data point for each specimen. The figure shows that a decrease in the local compactness ratio is associated with an increase in story-drift range. This figure clearly shows the importance of local slenderness limits for ensuring the inelastic deformation capacity of CBFs. All specimens meeting the highly ductile limit achieved a story-drift range of above 5%, indicating that the current highly ductile limit is sufficient and slightly conservative. Additionally, all the specimens achieved the 2.0% drift range as proposed for the moderately ductile limit and OCBF design with $1.0\sqrt{\frac{E}{R_yF_y}}$ as the local slenderness limit. Using this limit should provide satisfactory OCBF performance and greatly increase the number of rectangular HSS braces that are suitable for OCBF design. The figure includes the long (238 in.) specimens as well as both A500C and A1085 tubes; shorter specimens would have somewhat reduced deformation capacity as noted earlier.

Figure 11 illustrates the effect of the KL/r ratio. All the A500C and A1085 specimens that meet the AISC 341 highly ductile local compactness requirement achieved a story-drift range of at least 5%, regardless of value of KL/r.

Figures 10 and 11 show that the deformability of HSS braces depends on the local slenderness ratio, b/t, and the global slenderness ratio, KL/r. The scatter in Figure 10 around a single value of b/t is largely due to differences in KL/r. Likewise, the scatter in Figure 11 is largely due to differences in b/t. The effects of these ratios are not independent of one another, and their interaction should be considered in design limits and numerical models simulating buckling brace behavior.

SUMMARY AND CONCLUSIONS

ASTM A500C and A1085 rectangular HSS sections are used for braces used in CBFs. In comparison with the A500C standard, HSS sections meeting the A1085 standard must satisfy a tighter tolerance on wall thickness and maximum yield stress, as well as meet a minimum CVN toughness. In comparison to A500C HSS sections, A1085 HSS sections are newer (introduced in 2013) and therefore are not as common in structural steel construction. The

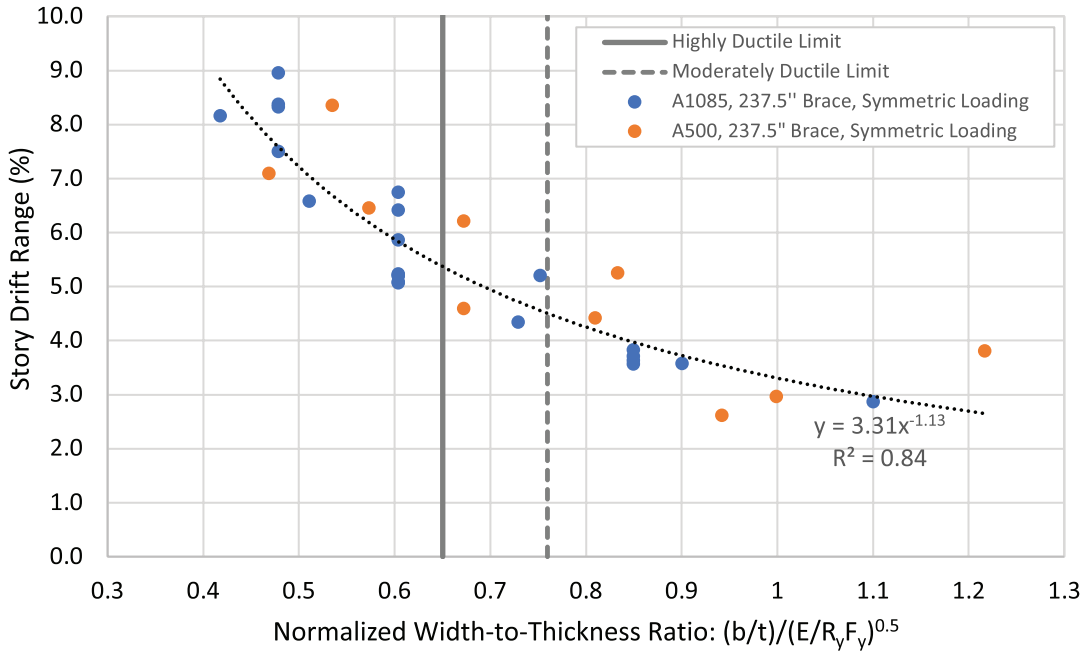

Fig. 10. Story-drift range vs. normalized width-to-thickness ratio.

tolerances on the A1085 HSS braces make them particularly attractive for seismic design because of the control on the geometry, toughness, and strength, yet there have been few tests of CBFs using A1085 HSS braces. As such, this research study was undertaken to investigate the differences in the two steel grades and the effect of those differences on the cyclic axial inelastic behavior of the brace and, therefore, the CBF.

Large-scale experiments and material testing were completed at the University of Washington Structural Engineering Testing Laboratory. Forty-one specimens were tested. The specimens were tested in four series. The first two series evaluated both A500 and A1085 HSS braces with b/t ratios ranging from of 9 to 25.7 and KL/r ratios ranging from about 60 to 127. The range of b/t values also permitted a study of the current limits in AISC 341 (2022) for high and moderate ductility limits, with the high ductility limit being set for SCBFs and the moderate ductility limit for OCBFs. In addition, series 3 and 4 tests permitted a direct comparison of several other study parameters, including (1) type of HSS (A500C or A1085); (2) HSS producer; (3) global slenderness ratio, KL/r; (4) local slenderness ratio, b/t; and (5) loading protocol (symmetric or chevron or near fault). The cyclic response of each brace specimens was analyzed to assess deformation capacity, energy dissipation capacity, and variations between manufacturers and materials.

The major conclusions from this work include:

- Deformability: The ductility (and energy dissipation capacity) of HSS bracing members is most significantly affected by both the local and global slenderness ratios (b/t and KL/r), which are interdependent.
- Cyclic response: The cyclic deformation capacity and energy dissipation increases with a decrease in local slenderness ratios and increase in global slenderness ratio.
- Steel grade: The variability between producers of A500C and A1085 were negligible. The variation in wall thickness was slightly greater for A500C braces, and A1085 have somewhat greater CVN toughness, but material properties were not significantly different.
- Local and global slenderness ratios: These ratios affect system deformability. Identical braces with identical b/t ratios provide greater inelastic deformation capacity with larger KL/r. Braces with similar KL/r will have more deformation capacity as the b/t ratios decreases.
- Deformation range: The defortmation range is a key engineering demand parameter for buckling braces. Under symmetric, cyclic loading, the response of the brace depends on the tension capacity, and the fracture life of the brace is determined by the response in compression, as affected by local and global slenderness limits. The maximum tensile deformation depends on

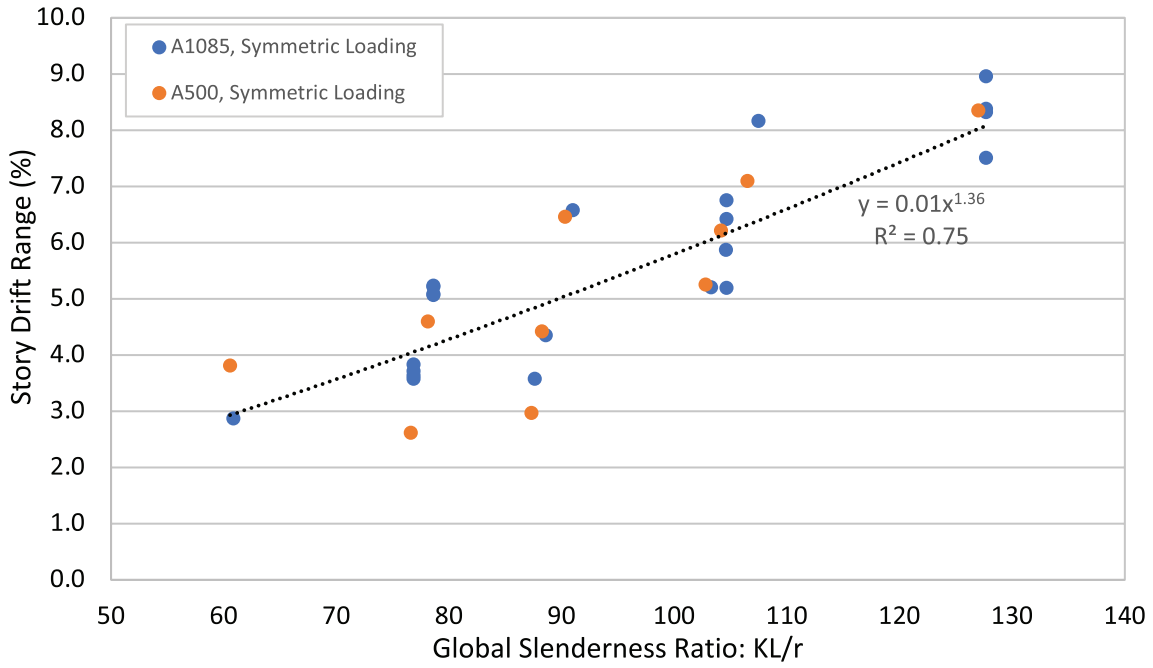

Fig. 11. Story drift range vs. global slenderness.

imposed deformation history, and therefore, the highest tensile displacements were measured for the symmetric and pulse-type (tension-dominated) history. However, the deformation range does not depend on imposed displacement history. Therefore, story drift range is a better measure of the maximum deformation capacity, rather than the maximum drift in any single direction. Further, the symmetric protocol provides a more conservative estimate of deformation capacity than the other protocols.

Additional research is needed to fully explore the range of b/t ratios for both types of HSS braces. In particular, HSS braces with larger b/t ratios (above 25) should be tested to investigate the possibility of increasing the moderately ductile limit from $0.76\sqrt{\frac{E}{R_yF_y}}$ to $1.0\frac{E}{R_yF_y}$; the latter term is supported by the results presented herein. In addition, the results of these tests should be used to update nonlinear models to investigate the impact of changes in the b/t limits on building performance. In addition, the research clearly shows that both local slenderness and global slenderness impact the deformability of square HSS braces. This interaction might be included in future revisions of AISC 341, Table D1.1a. Finally, the results of any future research study should be combined with this data to revisit both the highly ductile and the moderately ductile limits in AISC 341.

ACKNOWLEDGMENTS

This collaborative research study was jointly funded by AISC and members of the Steel Tube Institute. The authors are grateful for the financial support and material donations from these organizations.

REFERENCES

AISC (2022), *Seismic Provisions for Structural Steel Buildings*, ANSI/AISC 341-22, American Institute of Steel Construction, Chicago, Ill.

ASTM (2019), *Standard Specification for High-Strength Structural Bolts and Assemblies, Steel and Alloy Steel, Heat Treated, Inch Dimensions 120 ksi and 150 ksi Minimum Tensile Strength, and Metric Dimensions 830 MPa and 1040 MPa Minimum Tensile Strength*, ASTM F3125/F3125M-19, ASTM International, West Conshohocken, Pa.

ASTM (2020), *Standard Specification for Structural Steel Shapes*, ASTM A992/A992M-20, ASTM International, West Conshohocken, Pa.

ASTM (2021), *Standard Specification for Cold-Formed Welded and Seamless Carbon Steel Structural Tubing in Rounds and Shapes*, ASTM A500/500M-21a, ASTM International, West Conshohocken, Pa.

ASTM (2022), *Standard Specification for Cold-Formed Welded Carbon Steel Hollow Structural Sections (HSS)*, ASTM A1085/1085M-22, ASTM International, West Conshohocken, Pa.

ASTM (2023), *Standard Test Methods and Definitions for Mechanical Testing of Steel Products*, ASTM A370-23, ASTM International, West Conshohocken, Pa.

ATC (1992), "Guidelines for Cyclic Seismic Testing of Components of Steel Structures for Buildings," Report ATC-24, Applied Technology Council, Redwood City, Calif.

Ballard, R. (2015), "Impact of Connection Type on Performance of Non-Seismic Concentrically Braced Frames," MS Thesis, University of Washington, Seattle, Wash.

Clark, K.A. (2009), "Experimental Performance of Multi-Story X-Braced SCBF Systems," MS Thesis, University of Washington, Seattle, Wash.

Fell, B.V., Kanvinde, A.M., Deierlein, G.G., and Myers, A.T. (2009), "Experimental Investigation of Inelastic Cyclic Buckling and Fracture of Steel Braces," *Journal of Structural Engineering*, Vol. 135, No. 1, pp. 19–32.

FEMA (2000), "State of the Art Report on Systems Performance of Steel Moment Frames Subject to Earthquake Ground Shaking," FEMA 355C, Federal Emergency Management Agency, Washington, D.C.

Han, S.-W., Kim, W. T., and Foutch, D.A. (2007), "Seismic Behavior of HSS Bracing Members According to Width-Thickness Ratio under Symmetric Cyclic Loading," *Journal of Structural Engineering*, Vol. 133, No. 2, pp. 264–273.

Herman, D.J. (2007), "Further Improvements on an Understanding of Special Concentrically Braced Frame Systems," MS Thesis, University of Washington, Seattle, Wash.

Hsiao, P-C, Lehman, D.E., and Roeder, C.W. (2013), "Evaluation of Response Modification Coefficient and Collapse Potential of SCBFs," *Earthquake Engineering and Structural Dynamics,* Vol. 42, No. 10, pp. 1547–1564.

Ibarra, S.M. (2018), "Experimental Investigation of Chevron Special Concentrically Braced Frames with a Yielding Beam Plastic Mechanism," MS Thesis, University of Washington, Seattle, Wash.

Johnson, M. (2014), "Seismic Behavior of Bolted Connections in Non-Seismic Braced Frames," MS Thesis, University of Washington, Seattle, Wash.

Johnson, S.M. (2005), "Improved Seismic Performance of Special Concentrically Braced Frames," MS Thesis, University of Washington, Seattle, Wash.

Kotulka, B.A. (2007), "Analysis for a Design Guide on Gusset Plates Used in Special Concentrically Braced Frames," MS Thesis, University of Washington, Seattle, Wash.

Lee, S. (1988), "Seismic Behavior of Hollow and Concrete-Filled Square Tubular Bracing Members," Report UMCE 87-11, University of Michigan, Ann Arbor, Mich.

Lehman, D.E., Roeder, C.W., Herman, D., Johnson, S., and Kotulka, B., (2008), "Improved Seismic Performance of Gusset Plate Connections," *Journal of Structural Engineering*, ASCE, Vol. 134, No. 6, pp. 890–901.

Liu, Z. and Goel, S.C. (1987), "Investigation of Concrete-Filled Steel Tubes under Cyclic Bending and Buckling," University of Michigan, Ann Arbor, Mich.

Lumpkin, E.J. (2009), "Enhanced Seismic Performance of Multi-Story Special Concentrically Brace Frames Using a Balanced Design Procedure," MS Thesis, University of Washington, Seattle, Wash.

MTS (2011), MTS Model 793.10 MuliPurpose TestWare and Series 793 Application Software, MTS Systems Corporation, Eden Prairie, Minn.

Powell, J.A. (2010), "Evaluation of Special Concentrically Braced Frames for Improved Seismic Performance and Constructability," MS Thesis, University of Washington, Seattle, Wash.

Richard, J. (2009), "Etude du Comportemenet Sismique de Bâtiments Industriels aveć Systèmes de Contreventement en Acier de Faible Ductilitè," PhD Dissertation, Ecole Poly-technique de Montrèal, Montreal, Quebec, Canada.

Roeder, C., Sen, A., Terpstra, C., Ibarra, S. Liu, R., Lehman, D., and Berman, J. (2019), "Effect of Beam Yielding on Chevron Braced Frames," *Journal of Constructional Steel Research*, Vol. 159, pp. 428–441. DOI: 10.1016/j .jcsr.2019.04.04

Roeder, C.W., Lumpkin, E., and Lehman, D.E. (2011), "A Balanced Design Procedure for Special Concentrically Braced Frames," *Journal of Constructional Steel Research*, Vol. 62, pp. 1760–1776.

Roeder, C.W., Lumpkin, E., and Lehman, D.E. (2012), "Seismic Performance Assessment of Concentrically Braced Steel Frames," *Earthquake Spectra*, Vol. 28, No. 2, pp. 709–727.

Sen, A.D. (2014), "Seismic Performance of Chevron Concentrically Braced Frames with Weak Beams." MS Thesis, University of Washington, Seattle, Wash.

Sen, A.D. (2018), "New Methods for Seismic Performance Evaluation and Retrofit of Nonductile Concentrically Braced Frames," A dissertation submitted in partial fulfillment of degree of Doctor of Philosophy, University of Washington, Seattle, Wash.

Shaback, B. and Brown, T. (2003), "Behaviour of Square Hollow Structural Steel Braces with End Connections under Reversed Cyclic Axial Loading," *Canadian Journal of Civil Engineering*, Vol. 30, No. 4, pp. 745–753.

Swatosh, M.A. (2016), "Seismic Evaluation and Retrofit of Concentrically Braced Frames," MS Thesis, University of Washington, Seattle, Wash.

Sloat, D.A. (2014), "Evaluation and Retrofit of Non-Capacity Designed Braced Frames," MS Thesis, University of Washington, Seattle, Wash.

Yang, F. and Mahin, S.A. (2005), *Limiting Net Section Failure in Slotted HSS Braces*, Structural Steel Education Council, Moraga, Calif.

Uriz, P. and Mahin, S.A. (2008), "Toward Earthquake-Resistant Design of Concentrically Braced Steel-Frame Structures," PEER 2008/08, Pacific Earthquake Engineering Research Center, Berkeley, Calif.

Four-Bolt Unstiffened End-Plate Moment Connections with 36-in.-Deep Beams for Intermediate Moment Frames

Maria A. Mercado-Celin, Matthew R. Eatherton, and Thomas M. Murray

ABSTRACT

Previous testing has shown that four-bolt extended, unstiffened end-plate moment connections can be used with beams up to 24 in. deep and develop sufficiently ductile performance to satisfy seismic qualification. It is desirable to extend this depth limit to allow deeper beams for intermediate moment frames. Three moment connection specimens using built-up 36-in.-deep beams with a four-bolt extended, unstiffened end-plate moment connection were tested to determine if they satisfy the intermediate moment frame qualification criteria given in AISC 341-16 (2016a). The web of the specimens satisfied the moderately ductile section criteria for web slenderness, which is required for intermediate moment frames, but not highly ductile section criteria required for special moment frames.

All three specimens passed qualification criteria for intermediate moment frames (IMFs) as given in AISC 341-16 by retaining at least 80% of the nominal plastic moment strength through 2% story drift. The observed failure modes included lateral torsional buckling of the specimen, flange local buckling, net section fracture of the beam flange, and failure of the beam flange-to-beam web fillet weld. The results of these tests support current moderately ductile limits associated with lateral bracing and cross-section slenderness, given that the associated specimens reached IMF qualification criteria but not special moment frame (SMF) criteria. It was concluded that four-bolt extended, unstiffened end-plate moment connections satisfy intermediate moment frame requirements with a beam depth of 36 in. and that a modification is needed for beam web to flange welds in built-up sections near the moment connection.

Keywords: end-plate moment connection, intermediate moment frame, lateral-torsional buckling, beam net section fracture, moderately ductile section.

INTRODUCTION

Previous cyclic testing on four-bolt extended, unstiffened (4E) end-plate moment connections with beams deeper than 24 in. have failed to satisfy the intermediate or special moment frame (IMF or SMF) qualification criteria given in the 2016 edition of the AISC *Seismic Provisions for Structural Steel Buildings* (AISC, 2016a), hereafter referred to as AISC 341-16. Ryan and Murray (1999) tested one 4E specimen with a 55-in.-deep beam that resulted in bolt fracture at 0.01 rad rotation, and Blumenbaum and Murray (2004) tested two 4E specimens with 60-in.-deep rafters that resulted in bolt fracture and out-of-plane buckling at 0.01 rad to 0.02 rad. of inelastic rotation. Conversely, tests by Sumner et. al. (2000) and Meng and Murray (1996) reported successful SMF qualification tests of 4E moment connection specimens with W24×68 and W24×76 sections.

To facilitate longer spans, it is desirable to allow the use of 4E connections in IMF or SMF with beams deeper than 24 in. For that reason, a testing program was conducted to determine the required connection detailing such that the connection has sufficient ductility to achieve IMF qualification criteria with 36-in.-deep beams. The testing program utilized specimens with beam webs satisfying moderately ductile, but not highly ductile criteria and beam lateral bracing that satisfied either IMF or SMF criteria. In addition to evaluating IMF qualification, this study also represents a unique opportunity to investigate the distinction between IMF and SMF in terms of inelastic lateral torsional buckling and local buckling behavior.

EXPERIMENTAL PROGRAM

Test Specimens

The specimens were designed according to the procedures in the 2022 AISC *Prequalified Connections for Special and Intermediate Moment Frames for Seismic Applications* (AISC, 2022), hereafter referred to as AISC 358-22. The test beams were built-up sections with ⅝ in. × 8 in. flanges and ½-in.-thick webs. The flanges satisfy highly ductile

Maria A. Mercado-Celin, Graduate Research Assistant, Virginia Polytechnic Institute and State University, Blacksburg, Va. Email: mariamercado@vt.edu

Matthew R. Eatherton, Professor, Virginia Polytechnic Institute and State University, Blacksburg, Va. Email: meather@vt.edu (corresponding)

Thomas M. Murray, Emeritus Professor, Virginia Polytechnic Institute and State University, Blacksburg, Va. Email: thmurray@vt.edu

Paper No. 2023-07

Table 1. Test Matrix					
Specimen Identification	Beam Depth, *d* (in.)	Bolts	End-Plate Thickness (in.)	Double Fillet Weld Length (in.)[1]	Lines of Lateral Bracing
4E-1.5-1.75-36a	36	1½ in. A490	1¾	24	2
4E-1.5-1.75-36b	36	1½ in. A490	1¾	24	3
4E-1.5-1.75-36c	36	1½ in. A490	1¾	48	3

[1] Length of double-sided fillet weld at the beam web-to-beam flange, measured from the outside face of the end-plate (see dimension L3 in Figure 1).

Table 2. Specimen Thicknesses (all units are inches)								
Specimen	Web Thickness		Lower-Flange Thickness		Upper-Flange Thickness		End-Plate Thickness	
	Nominal	Measured	Nominal	Measured	Nominal	Measured	Nominal	Measured
4E-1.5-1.75-36a	0.50	—	0.625	0.628	0.625	0.624	1.75	1.781
4E-1.5-1.75-36b	0.50	0.535	0.625	0.64	0.625	0.625	1.75	1.765
4E-1.5-1.75-36c	0.50	0.535	0.625	0.625	0.625	0.64	1.75	1.765

Table 3. Specimen Dimensions			
Specimen	Length, L1	Length, L2	Length, L3
4E-1.5-1.75-36a	20'-2⅞"	5'-0"	24"
4E-1.5-1.75-36b	23'-8⅞"	8'-6"	24"
4E-1.5-1.75-36c	23'-8⅞"	8'-6"	48"

Table 4. Material Properties								
Specimen	Element	Material Specification	From Mill Report			Measured Properties		
			F_y (ksi)	F_u (ksi)	Elongation	F_y (ksi)	F_u (ksi)	Elongation
4E-1.5-1.75-36a	Beam flange	A529 Gr. 55	55.4	76.6	25%	53.7	74.1	41%
4E-1.5-1.75-36a	Beam web	HSLA55	64.8	78.5	32%	—	—	—
4E-1.5-1.75-36a	End plate	A572 Gr. 50	59.0	82	38%	—	—	—
4E-1.5-1.75-36b,c	Beam flange	A529 Gr. 55	56.6	77.7	23%	53.1	77.3	38%
4E-1.5-1.75-36b,c	Beam web	HSLA55	64.9	76.1	34%	59.7	72.9	24%
4E-1.5-1.75-36b,c	End plate	A572 Gr. 50	55.2	81.4	25%	—	—	—

section criteria, per AISC 341-16 (AISC, 2016a), and the webs satisfy moderately ductile section criteria. The detailing of the moment connection satisfied requirements of AISC 358-22. Table 1 is the text matrix, Figure 1 shows beam and end-plate details, and Tables 2 and 3 give specific dimensions. The built-up beams were fabricated using A572/A572M (ASTM, 2021) Grade 55 steel for the flanges, HSLA55 steel for the webs, and A572 Grade 50 for the end plates with material properties given in Table 4.

The specimen identification is given with the bolt configuration ("4E" for four-bolt extended, unstiffened), bolt diameter ["1.5" for the 1.5 in. ASTM F3125/3125M (ASTM, 2022) Grade A490 bolts], end-plate thickness (1.75 in.), beam depth (36 in.), and then a letter to distinguish among the three specimens. The specimens are therefore labeled, 4E-1.5-1.75-36a, 4E-1.5-1.75-36b, and 4E-1.5-1.75-36c.

In accordance with AISC 358-22, Section 6.3.1(1), the beam web-to-beam flange weld was specified to be ⅜ in. double-sided fillet with a minimum required length of 24 in., which was used for Specimens 4E-1.5-1.75-36a and 4E-1.5-1.75-36b. The length of double-sided fillet weld was increased to 48 in. for Specimen 4E-1.5-1.75-36c.

To make efficient use of the steel beams, both ends of each beam had end plates attached so that two unique specimens

could be created with one beam. A set of four holes in the beam flange were included in all specimens, centered at a distance, L2, from the outside face of the end plate (see Figure 1 and Table 3). The holes in the beam flange facilitate connection to the actuator when testing the far side end-plate connection. The distance from outside face of end plate to centerline of the bolt holes, L2, was extended for Specimens 4E-1.5-1.75-36b and 4E-1.5-1.75-36c.

Test Setup

Three tests were conducted in accordance with AISC 341-16, Chapter K, at the Thomas M. Murray Structural Engineering Laboratory at Virginia Tech. A schematic of the test setup is shown in Figure 2, and a photograph is in Figure 3. The setup used in this study simulated an exterior moment connection in a structure with 32-ft-wide bays and a 12 ft story height. The reaction column was a W14×398. Force was applied by an MTS 201.70 servo hydraulic actuator with a ±10 in. stroke and a tension capacity of 220 kips.

Lateral bracing for specimen 4E-1.5-1.75-36a was provided at the end of the plastic hinge and near the point of loading as shown in Figure 2. This lateral bracing satisfies IMF requirements in AISC 341-16, Section D1.2a.1, but not SMF requirements in Section D1.2b. An additional line of lateral bracing was added for specimen 4E-1.5-1.75-36b and specimen 4E-1.5-1.75-36c (see Figure 3), to meet the unbraced length required for SMF. More details are provided in the section on lateral torsional buckling of Specimen 4E-1.5-1.75-36a.

Lateral bracing consisted of steel frames with adjustable steel angles that were moved until the face of the angle was approximately 1/16 in. away from the flange tips. Lithium grease was applied to the face of the angles to reduce friction during the test. An example of the lateral bracing is shown in Figure 4.

Instrumentation Plan

The instrumentation plan is shown in Figure 5. String potentiometers SP_01, SP_02, SP_03, and SP_08 were used to measure column movement. String potentiometers SP_04 and SP_05 measured beam vertical movement. Sensors SP_06 and SP_07 measured axial deformation of the plastic hinge zone, while SP_09 measured vertical end-plate movement with respect to the column. Two instrumented spring calipers, CLP_01 and CLP_02, were used to measure the end-plate separation from the column flange. Linear potentiometers LP_01 and LP_02 measured panel-zone shear deformations. The applied force and displacement were

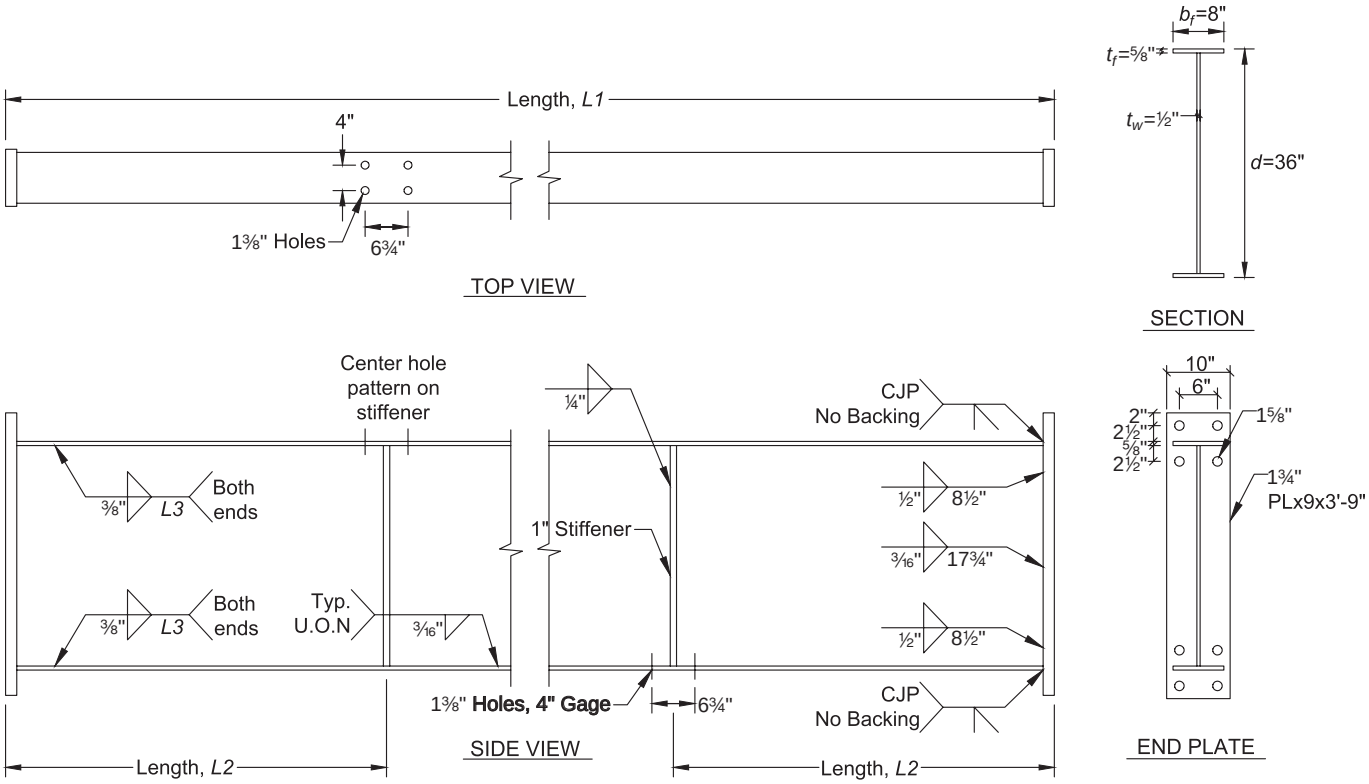

Fig. 1. Details of the beam.

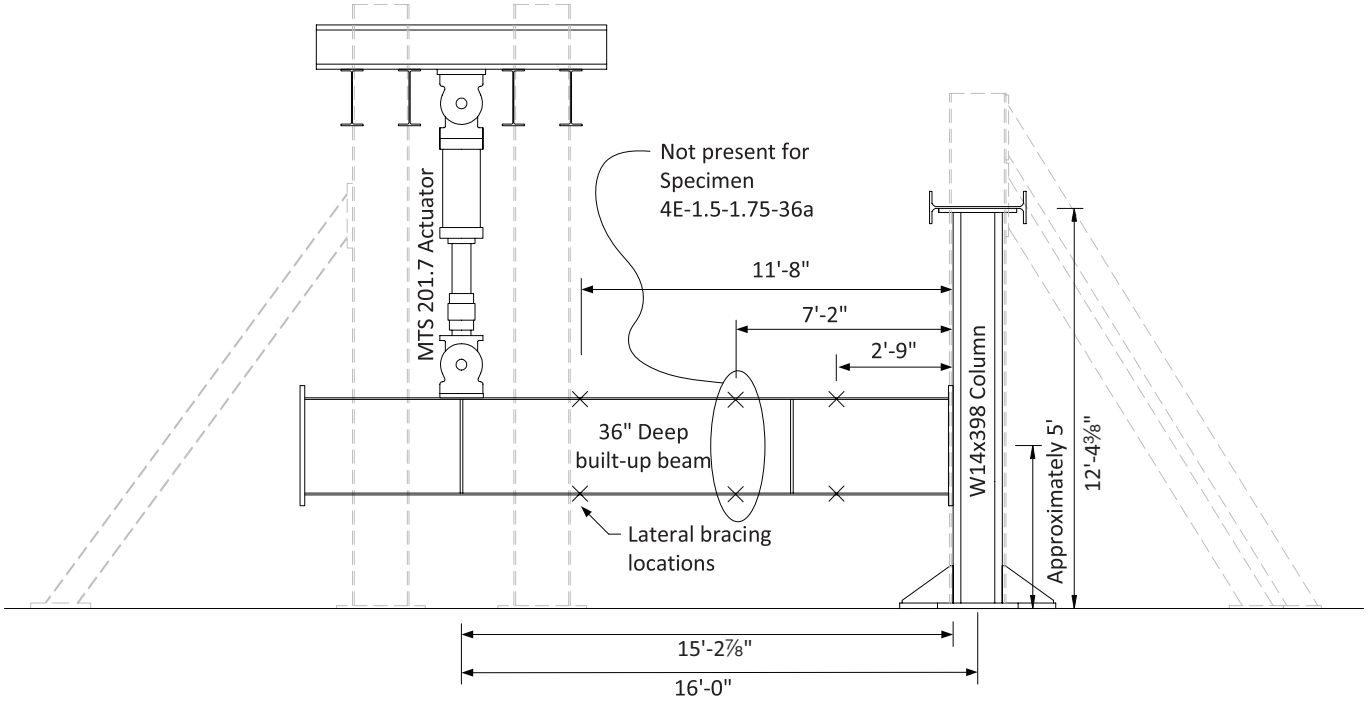

Fig. 2. Schematic of test setup.

Fig. 3. Photograph of the test setup.

Fig. 4. Beam lateral bracing.

Table 5. AISC 341-16 Displacement Protocol for Moment Connection Tests		
Story Drift Target		Number of Cycles
Radians	Percent	
0.00375	0.375	6
0.005	0.5	6
0.0075	0.75	6
0.01	1	4
0.015	1.5	2
0.02	2	2
0.03	3	2
0.04	4	2
0.045	4.5	Until fracture

measured by the actuator's internal load cell and displacement transducer. All sensors were connected to a National Instruments data acquisition system, which was managed using National Instruments Signal Express software (NI, 2015). Measurements from all sensors were recorded at 3 Hz.

Displacement Protocol and Qualification Criteria for IMF and SMF

The cyclic displacement protocol from AISC 341-16, Chapter K, for qualification testing of IMF and SMF moment connections was used and is given in Table 5. The maximum displacement that could be applied corresponded to

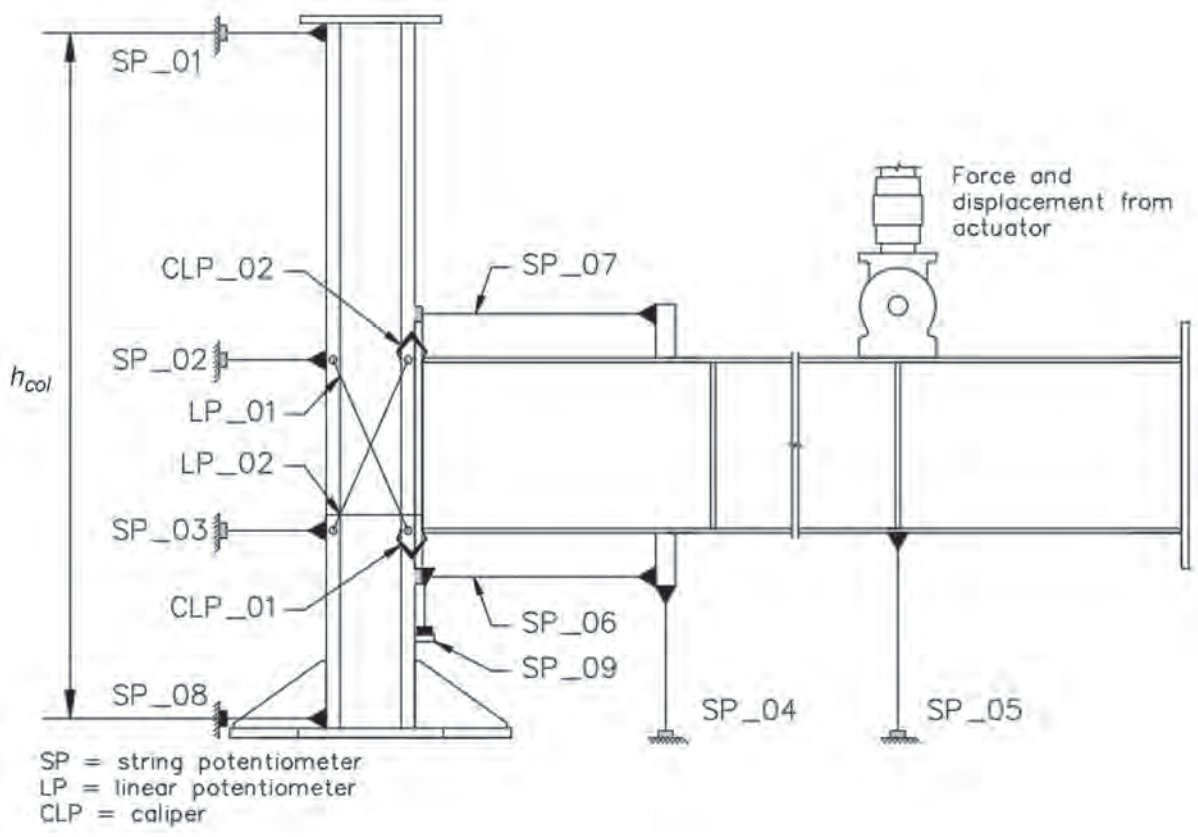

Fig. 5. Instrumentation plan for tests.

4.5% story drift based on the location and maximum stroke of the actuator. The displacement rate was 0.00025 rad/s, which corresponds to a vertical displacement at the actuator of approximately 2.88 in./min.

The story drift was calculated real-time within the MTS control software (MTS, 2012) using external feedback, and then used to control the actuator displacement to produce the story drifts given in Table 5. The applied story drift, θ_{APP}, was calculated in the MTS MultiPurpose Testware (MTS, 2011) calculations module using Equation 1.

$$\theta_{APP} = \frac{-\delta_{SP\text{-}05}}{L_{cl}} - \frac{\delta_{SP\text{-}01} - \delta_{SP\text{-}08}}{h_{col}} \quad (1)$$

where

L_{cl} = distance from the actuator centerline to column centerline, 192 in.

h_{col} = distance between SP_01 and SP_08, 137 in.

$\delta_{SP\text{-}01}$ = displacement measured by SP_01, in.

$\delta_{SP\text{-}05}$ = displacement measured by SP_05, in.

$\delta_{SP\text{-}08}$ = displacement measured by SP_08, in.

The qualification criteria for intermediate moment frame connections in AISC 341-16 states that the connection must maintain a moment strength at the face of the column of at least 80% of the nominal beam plastic moment strength through the first cycle of 2% story drift. For special moment frame connections, the requirement is similar but is evaluated at the first cycle of 4% story drift. The moment at the face of the column was calculated as the applied load multiplied by the distance from the actuator to the face of the column, 15.23 ft. Based on the beam cross section shown in Figure 1 with plastic section modulus, Z_x = 328 in.^{3}, and a nominal yield stress of F_y = 55 ksi, the nominal plastic moment strength of the beam is M_p = 1,500 kip-ft.

RESULTS

IMF Qualification

All three specimens passed qualification criteria for intermediate moment frames (IMFs) as given in AISC 341-16 by retaining at least 80% of the nominal plastic moment strength through 2% story drift. Table 6 gives the moment strength for each specimen at the positive and negative peak during the first cycle at 2% story drift, values significantly larger than $0.8M_p$ = 1,200 kip-ft. The three specimens had almost identical behavior through the 2% story drift cycles, as shown in Figure 6, with no observable flange local buckling or strength degradation while the flanges yielded. The measured initial stiffness of the specimens was 158,000 kip-ft/rad that, after removing the elastic beam stiffness of 193,000 kip-ft/rad, results in a connection stiffness of 863,000 kip-ft/rad. The minimum connection stiffness to be considered a fully restrained connection per the AISC *Specification for Structural Steel Buildings* (AISC, 2016b), hereafter referred to as AISC 360-16, Section B3.4 Commentary, is $20EI/L$ = 644,000 kip-ft/rad using a beam span equal to 32 ft less the column depth. Since the measured connection stiffness is greater than this minimum, the connection is considered fully restrained.

Specimen 4E-1.5-1.75-36c survived to the 4% story drift cycles, but as shown in Table 6 and due to local buckling of the beam section, the moment strength dropped to approximately 95% of the required moment strength to reach special moment frame (SMF) qualification (1,150 kip-ft compared to the required 1,200 kip-ft). The end-plate separation remained small for all tests with a maximum value of approximately 0.12 in. for one specimen and was less than 0.05 in. for the other two specimens. There was no observed yielding or damage to the end-plates or bolts during any of the tests. This suggests that the design procedures in AISC 358 for the end plate and bolts were sufficient for this connection.

Specimen Response

The first two specimens experienced several undesirable limit states that were progressively mitigated until the third specimen for which all these limit states were prevented. As shown in Table 7, Specimens 4E-1.5-1.75-36a and 4E-1.5-1.75-36b survived to the 3% story drift cycles, while Specimen 4E-1.5-1.75-36c exhibited excellent fracture resistance and ductility surviving multiple cycles at 4.5% story drift before the test was stopped. The individual limit states for Specimens 4E-1.5-1.75-36a and 4E-1.5-1.75-36b are discussed in the subsequent paragraphs. Figure 7 shows the final condition of each specimen. Greater deformations were achieved as the specimens and test setup were retrofitted based on the failure modes observed.

Beam Net Section Fracture of Specimen 4E-1.5-1.75-36a (Not Related to Qualification)

Specimen 4E-1.5-1.75-36a experienced a net section fracture of the beam at the location of a set of holes approximately 4.75 ft from the face of the column, as shown in Figure 8. AISC 360-16, Section F13 (AISC, 2016b), provides a way to check for such a limit state based on a ratio of the flange net area to the flange gross area. The required moment strength at the location of the bolt holes associated with the beam developing the maximum probable moment strength, M_{pr}, at the column face is calculated as, M_u = 1,230 kip-ft. The nominal moment strength calculated in accordance with AISC 360-16, Section F13, is found to be M_n = 1,040 kip-ft, which is less than the required moment strength, M_u, and therefore suggests that the beam flange is susceptible to beam net section fracture. It is noted that

Table 6. Summary of Qualification Status for Each Specimen				
Specimen	First Cycle at Story Drift of	Moment at Positive Peak[1]	Moment at Negative Peak[1]	Qualification[2]
4E-1.5-1.75-36a	2%	1660 kip-ft	1620 kip-ft	IMF
4E-1.5-1.75-36b	2%	1650 kip-ft	1760 kip-ft	IMF
4E-1.5-1.75-36c	2%	1710 kip-ft	1710 kip-ft	IMF
	4%	1210 kip-ft	1150 kip-ft	

[1] Moment calculated at the column face
[2] Qualification is reached if moment strength is greater than $0.8M_p$ = 1200 kip-ft

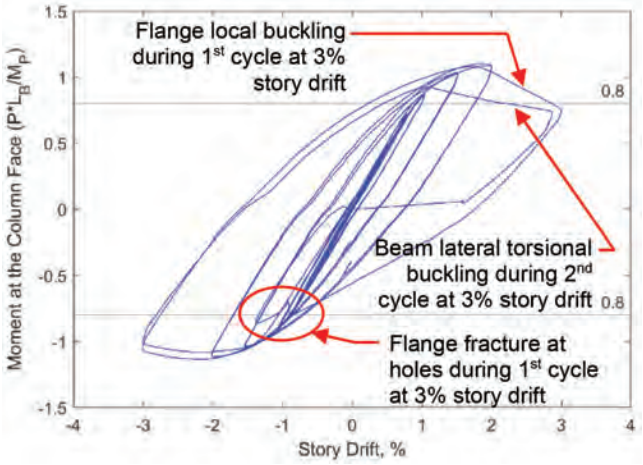

(a) Specimen 4E-1.5-1.75-36a

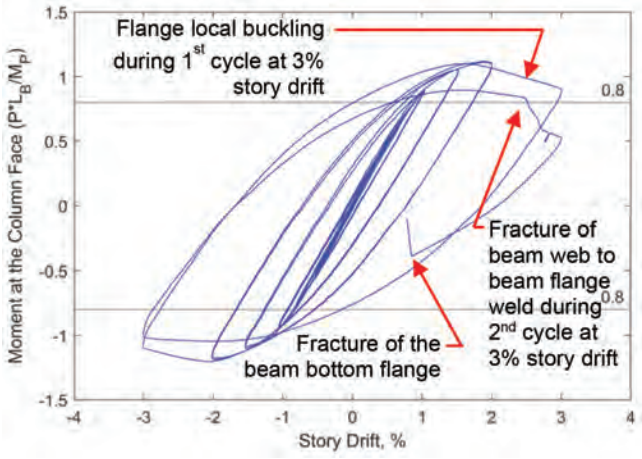

(b) Specimen 4E-1.5-1.75-36b

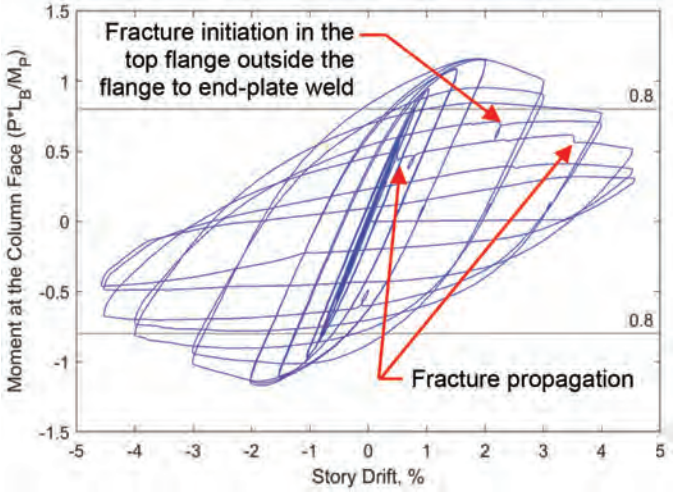

(c) Specimen 4E-1.5-1.75-36c

Fig. 6. Hysteretic behavior of the three specimens.

Table 7. Summary of Failure Mode for Each Specimen		
Specimen	**Peak Story Drift Attained**	**Failure Mode**
4E-1.5-1.75-36a	2 cycles at 3%	Lateral torsional buckling
4E-1.5-1.75-36b	2 cycles at 3%	Fracture of beam web-to-beam flange weld, then flange fracture
4E-1.5-1.75-36c	3 cycles at 4.5%	Flange local buckling, fracture of the beam flange outside the CJP weld at the end-plate

at the time of fracture, the moment at the face of the column was approximately 65% of M_{pr}, which was used in the calculation, but during the previous cycle, the moment at the column face was close to M_{pr}. It is possible that net section fracture initiated during the previous cycle but was not noticed. The specimen was repaired by welding a flange plate to the outside of the bottom flange, as shown in Figure 9, in an effort to continue the test.

For Specimens 4E-1.5-1.75-36b and 4E-1.5-1.75-36c, the distance from the column face to the first set of bolt holes was increased to approximately 8.25 ft, which was selected so that the required moment strength, M_u = 750 kip-ft was

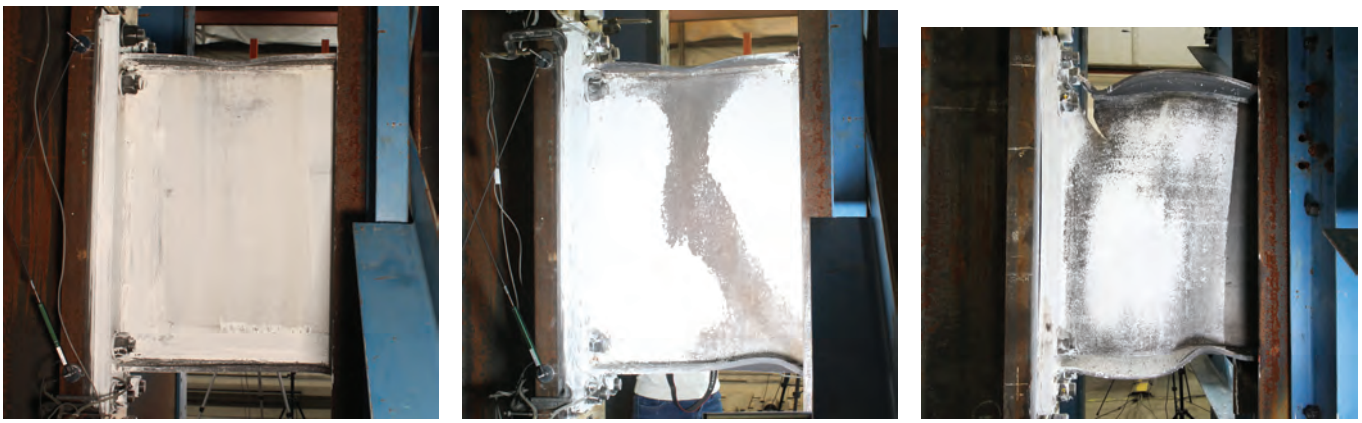

(a) Specimen 4E-1.5-1.75-36a *(b) Specimen 4E-1.5-1.75-36b* *(c) Specimen 4E-1.5-1.75-36c*

Fig. 7. Final state at the connection of each specimen.

Fig. 8. Bottom flange fracture at bolt holes of Specimen 4E-1.5-1.75-36a.

Fig. 9. Bottom flange repair with welded plate of Specimen 4E-1.5-1.75-36a.

less than the design moment, ϕM_n = 778 kip-ft. Neither of these specimens experienced net section fracture of the beam, suggesting that the requirements of AISC 360, Section F13, were effective in addressing this limit state.

Lateral Torsional Buckling of Specimen 4E-1.5-1.75-36a

After the bottom flange repair, Specimen 4E-1.5-1.75-36a was further tested and underwent lateral torsional buckling in the unbraced length equal to 107 in, as shown in Figure 10. According to AISC 341-16, Section D1.2, the maximum unbraced length for moderately ductile, $L_{b,Mod}$, and highly ductile, $L_{b,High}$, are given by Equations 2 and 3.

$$L_{b,Mod} = \frac{0.19 r_y E}{R_y F_y} \tag{2}$$

$$= \frac{0.19(1.40 \text{ in.})(29{,}000 \text{ ksi})}{(1.1)(55 \text{ ksi})}$$

$$= 128 \text{ in.}$$

$$L_{b,High} = \frac{0.095 r_y E}{R_y F_y} \tag{3}$$

$$= \frac{0.095(1.40 \text{ in.})(29{,}000 \text{ ksi})}{(1.1)(55 \text{ ksi})}$$

$$= 64 \text{ in.}$$

where

E = modulus of elasticity, ksi

F_y = nominal yield stress, ksi

R_y = ratio of the expected yield stress to the specified minimum yield stress

r_y = radius of gyration about the y-axis, in.

The provided unbraced length for Specimen 4E-1.5-1.75-36a was 107 in., meeting the moderately ductile section requirements for IMF but not the highly ductile section requirements for SMF. This is consistent with the results obtained where Specimen 4E-1.5-1.75-36a experienced lateral torsional buckling after passing 2% story drift cycles (IMF) but before reaching 4% story drift (SMF).

The unbraced length for Specimen 4E-1.5-1.75-36c, was 54 in., which satisfied the highly ductile section and thus SMF design requirements. This is also consistent with the resulting behavior in that the specimen reached and exceeded 4% story drift without experiencing lateral torsional buckling.

Buckling and Fracture Behavior of Specimen 4E-1.5-1.75-36b

Specimen 4E-1.5-1.75-36b underwent beam flange and web local buckling, shown in Figures 11 and 12, with associated reduction in moment strength. In addition, Figure 13 shows the weld fracture at the beam web to the beam flange joint where the weld transitioned from a ⅜ in. double-sided fillet weld to a 5⁄16 in. single-sided fillet weld. The requirement for the double-sided fillet weld comes from AISC 358-22, Section 6.3.1(1), which requires specific welds at moment-connected ends of welded built-up sections, within at least the depth of beam or three times the width of flange, whichever is less. In this region, the beam web and flanges shall be connected using either a complete-joint-penetration (CJP) groove weld or a pair of fillet welds, each having a size 75% of the beam web thickness but not less than ¼ in. For the specimens in this study, the requirement results in a ⅜ in. double-sided fillet weld (or CJP weld) that extends for 24 in. Beyond this region, the beam web to flange weld is

Fig. 10. Lateral torsional buckling of the beam of Specimen 4E-1.5-1.75-36a.

designed for shear transfer that, for these specimens, allows the use of a 3⁄16 in. single-sided fillet weld. This type of single-sided weld is common for the web to flange joint in built-up beams typically used in metal buildings.

Previously tested 4E specimens that satisfied SMF requirements used sections satisfying highly ductile section criteria (Meng and Murray, 1996) and generally resulted in local buckling confined to a length of the beam that was the lesser of the depth of the beam or three times the flange width. It is also noted that other previous end-plate moment connection tests (configurations other than 4E) with built-up beam sections satisfying highly ductile section criteria did not experience this type of beam web to flange weld fracture (Szabo et al., 2017; Zarat-Basir et al., 2020). Specimen 4E-1.5-1.75-36b in the current test series had a beam web that satisfied moderately ductile section criteria, but not highly ductile section criteria, and experienced local buckling that extended over a length of approximately 4 ft (Figure 12). Previous tests with built-up beam sections satisfying moderately ductile but not highly ductile section

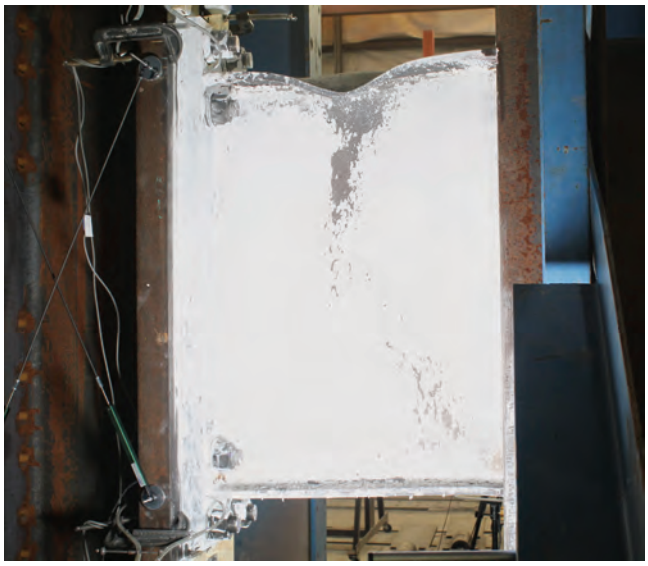

Fig. 11. Flange local buckling during the first cycle at 3% story drift.

Fig. 12. Beam flange local buckling extending approximately 3 ft to 4 ft from the face of the column.

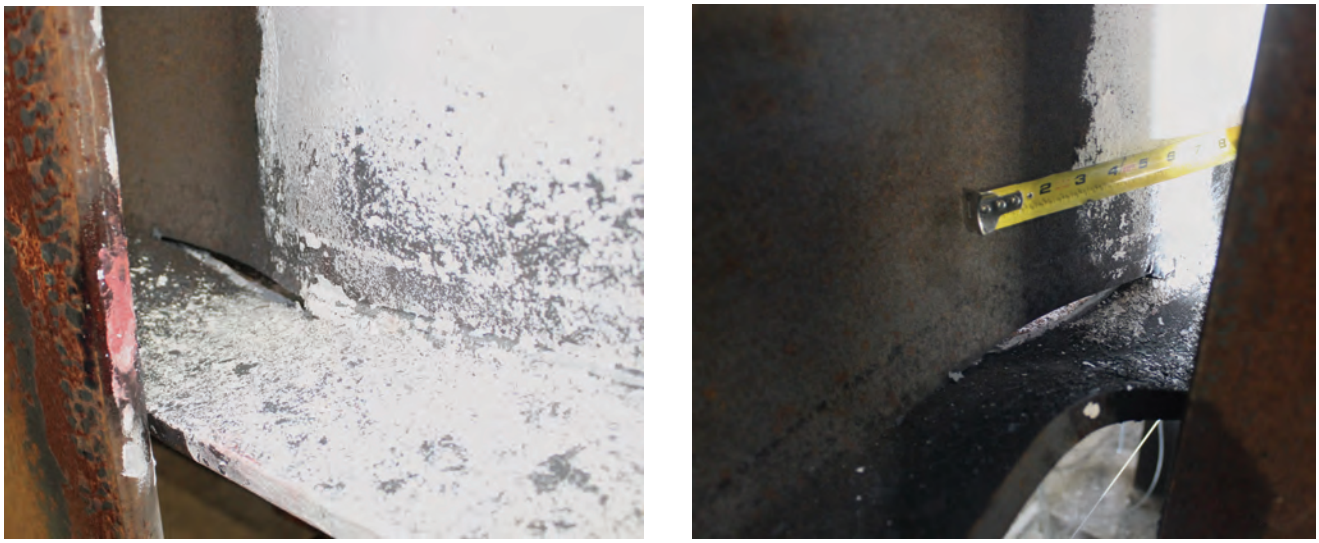

Fig. 13. Fracture of beam web to beam flange weld of Specimen 4E-1.5-1.75-36b.

criteria similarly showed buckling over larger lengths (Blumenbaum and Murray, 2004). The larger zone of local buckling either caused or was exacerbated by the fracture of the weld joining the beam web and flange for Specimen 4E-1.5-1.75-36b.

It appears that the larger web slenderness, compared to previous SMF qualification tests, contributed to the local buckling extending over a longer length and the observed weld fracture. Therefore, it is concluded that moment connections with moderately ductile section classification designed for IMF require longer length of the larger beam web to flange weld. Based on the successful test results of Specimen 4E-1.5-1.75-36c, where the beam web to flange weld did not fracture, a weld length double that currently required in AISC 358-22, Section 6.3.1(1), is recommended with beams satisfying moderately ductile section classification.

CONCLUSIONS AND RECOMMENDATIONS

Three specimens were tested to evaluate whether four-bolt extended, unstiffened moment connections with 36-in.-deep built-up beams can satisfy IMF qualification criteria in AISC 341-16 (2016a). All three specimens satisfied IMF qualification criteria by retaining a moment strength at the face of the column flange greater than 80% of the nominal plastic moment strength of the beam through a cyclic displacement protocol up to 2% story drift. The specimens exhibited excellent behavior through the 2% story drift cycles with only yielding of the section, no observed local buckling, and no undesirable limit states.

The test results support the beam net section fracture requirements in AISC 360-16, Section F13 (2016b), which successfully predicted net section fracture of the beam in the first specimen and the lack of net section fracture in the following two specimens. The test results also verified the difference in requirements for IMF and SMF in two ways: (1) The first specimen, which satisfied moderately ductile lateral bracing requirements, but not highly ductile requirements, experienced lateral torsional buckling after reaching 2% story drift (IMF), but before reaching 4% story drift (SMF). (2) The beam webs satisfied moderately ductile section classification but not highly ductile section classification. Local buckling of the beam in the third specimen occurred after satisfying the qualification requirements for IMF, but led to a severe reduction in moment strength at 4% story drift which was less than required for SMF qualification.

Based on the results of this study, the following recommendations are made for modifying the requirements in AISC 358-22 (2022):

1. Table 6.1 should be modified to allow a beam depth up to 36 in. for the four-bolt unstiffened (4E) connection configuration for use in intermediate moment frames.
2. Section 6.3.1(1) should be modified to extend the length of the larger weld (CJP or double-filled weld) to a length that is double the current requirement—that is, two times the depth of the beam or six times the flange width, whichever is less, when the beam section satisfies moderately ductile section classification but not highly ductile section classification.

In addition to these recommended changes, net section fracture of the beams and columns in seismic moment frames should be prevented at the location of any holes. For the specimens tested herein, net section fracture was avoided when the design moment strength, calculated in accordance with AISC 360-16, Section F13, was greater than the required moment strength at the hole location, calculated based on the beam reaching its probable maximum moment at the plastic hinge.

ACKNOWLEDGMENTS

This research was supported by the Metal Building Manufacturers Association (MBMA) with in-kind funding provided by Bluescope Buildings North America, Kansas City, Missouri. The authors thank the members of the MBMA advisory committee for their input during this project.

REFERENCES

AISC (2016a), *Seismic Provisions for Structural Steel Buildings,* ANSI/AISC 341-16, American Institute of Steel Construction, Chicago, Ill.

AISC (2016b), *Specification for Steel Structural Buildings,* ANSI/AISC 360-16*,* American Institute of Steel Construction, Chicago, Ill.

AISC (2022), *Prequalified Connections for Special and Intermediate Steel Moment Frames for Seismic Applications,* ANSI/AISC 358-22, American Institute of Steel Construction, Chicago, Ill.

ASTM (2021), *Standard Specification for High-Strength Low-Alloy Columbium-Vanadium Structural Steel*, ASTM A572/572M-21e1, ASTM International, West Conshohocken, Pa.

ASTM (2022), *Standard Specification for High-Strength Structural Bolts and Assemblies, Steel and Alloy Steel, Heat Treated, In. Dimensions 120 ksi and 150 ksi Minimum Tensile Strength, and Metric Dimensions 830 MPa and 1040 MPa Minimum Tensile Strength*, ASTM F3125/3125M-22, ASTM International, West Conshohocken, Pa.

Blumenbaum, S. and Murray, T.M. (2004), "Response of Cyclically Loaded Extended End-Plate Moment Connections when Used with Welded Built-Up Sections," Virginia Tech Structural Engineering and Materials Report No. CEE/VPI-ST-04/02, Blacksburg, Va.

Meng, R.L. and Murray, T.M. (1996), "Moment End-Plate Connections for Seismic Loading," Virginia Tech Structural Engineering Report No. CE/VPI-ST-96/04, Blacksburg, Va.

MTS (2011), MTS Model 793.10 MultiPurpose TestWare and Series 793 Application Software, MTS Systems Corporation, Eden Prairie, Minn.

MTS (2012), MTS Series 793 Control Software, MTS Systems Corporation, Eden Prairie, Minn.

NI (2015), SignalExpress Getting Started with Signal-Express, National Instruments, Austin, Tex.

Ryan, J.C., Jr., and Murray, T.M. (1999), "Evaluation of the Inelastic Rotation Capability of Extended End-Plate Moment Connections," Virginia Tech Structural Engineering and Materials Report No. CE/VPI-ST 99/13, Blacksburg, Va.

Sumner, E.A., Mays, T.W., and Murray, T.M. (2000), "Cyclic Testing of Bolted Moment End-Plate Connections," SAC Report No. SAC/BD-00/21, Virginia Tech Structural Engineering Report No. CE/VPI-ST 00/03, Blacksburg, Va.

Szabo, T., Eatherton, M.R., He, X., and Murray, T.M. (2017), "Study of a Twelve Bolt Extended Stiffened End-Plate Moment Connection," Virginia Tech Structural Engineering and Materials Report No. CE/VPI-ST-17/02, Blacksburg, Va.

Zarat-Basir, M., Eatherton, M.R., and Murray, T.M. (2020), "Testing of Stiffened and Unstiffened Twelve Bolt Extended End-Plate Moment Connections," Virginia Tech Structural Engineering and Materials Report No. CE/VPI-ST-20/01, Blacksburg, Va.

Guide for Authors

Scope

Engineering Journal is dedicated to the improvement and advancement of steel construction. Its pages are open to all who wish to report on new developments or techniques in steel design, research, the design and/or construction of new projects, steel fabrication methods, or new products of significance to the uses of steel in construction. Only original papers should be submitted.

General

Papers intended for publication should be submitted by email Margaret Matthew, editor, at **matthew@aisc.org**.

The articles published in the *Engineering Journal* undergo peer review before publication for (1) originality of contribution; (2) technical value to the steel construction community; (3) proper credit to others working in the same area; (4) prior publication of the material; and (5) justification of the conclusion based on the report.

All papers within the scope outlined above will be reviewed by engineers selected from among AISC, industry, design firms, and universities. The standard review process includes outside review by an average of three reviewers, who are experts in their respective technical area, and volunteers in the program. Papers not accepted will not be returned to the author. Published papers become the property of the American Institute of Steel Construction and are protected by appropriate copyrights. No proofs will be sent to authors.

Manuscripts

Manuscripts must be provided in Microsoft Word format. Include a PDF with your submittal so we may verify fonts, equations and figures. View our complete author guidelines at **aisc.org/ej**.

Smarter. Stronger. Steel.

American Institute of Steel Construction
130 E Randolph St, Ste 2000, Chicago, IL 60601
312.670.2400 | aisc.org/ej